3-14-2014

Chromium Evaporation of Metallic Component Materials in Solid Oxide Fuel Cell (SOFC)

Le Ge
University of Connecticut - Storrs, gavin.gele@gmail.com

Chromium Evaporation of Metallic Component Materials in Solid Oxide Fuel Cell (SOFC)

Le Ge, Ph.D.

University of Connecticut, 2014

Recent developments of planar intermediate temperature solid oxide fuel cells (IT-SOFCs) make metallic alloys attractive candidates as interconnects as well as balance of plant (BoP) materials at operating temperatures below 900 ^{o}C. The resistance of alloys against oxidation and corrosion is one of the critical criteria for selecting candidate alloys for SOFC applications. The oxidation and corrosion resistance of the alloys service at high temperature depends on the formation of a protective oxide scale (chromia. silica, alumina). Among these, chromia forming alloys are often used in SOFCs. At higher temperature, the evaporation of chromium containing species from chromia in humid air limits the applications of chromia forming alloys. SOFCs are susceptible to chromium evaporation (known as chromium poisoning) as it can lead to severe degradation of SOFC performance.

In this study, the transpiration method was used to measure the chromium evaporation rates from chromium evaporation of chromia and alumina forming nickel and iron base alloys. The effects of the temperature and water vapor content on the chromium evaporation rates were also investigated. The measured chromium evaporation rates were used to predict the degradation rates of the SOFCs under those conditions.

The oxidation behavior of candidate alloys in air with different water vapor contents was studied. The effects of the temperature and water vapor content on physicochemical characteristics of the oxide scales formed on the surface of metallic components were also examined.

To reduce the chromium evaporation rates and to mitigate the chromium poisoning, two coating systems were investigated. The electrical conducting cobalt manganese oxide coatings were applied on ferritic substrate (AISI 441) used as inteconnect, while electrical non-conducting aluminized coatings were applied on austenitic substrate used as BoP components. The evolution of cobalt manganese oxide coating system during heat treatment and reactions with underlying substrate were also studied in detail by electron microscopy. Both coating systems showed significant reduction in chromium evaporation rates when compared with uncoated alloys.

Chromium Evaporation of Metallic Component Materials in Solid Oxide Fuel Cell (SOFC)

Le Ge

B.E., City University of Hong Kong, Hong Kong, 2006

A Dissertation

Submitted in Partial Fulfillment of the

Requirements for the Degree of Doctor of Philosophy

at the

University of Connecticut

2014

APPROVAL PAGE

Doctor of Philosophy Dissertation

Chromium Evaporation of Metallic Component Materials in Solid Oxide Fuel Cell (SOFC)

Presented by

Le Ge, B.E.

Major Advisor _____

Prabhakar Singh

Associate Advisor _____

Frederick S. Pettit

Associate Advisor _____

Harris L. Marcus

University of Connecticut

2014

Dedicated to my parents

ACKNOWLEDGEMENTS

Thanks to my family for all of your love and support. Thanks to Prof. Singh and Prof. Pettit for all that you've taught me. Thanks to Dr. Verma, Peter, David, Mark and my lab mates at C2E2 for all your help. Thanks to my friends and gracias to Yashan and April.

TABLE OF CONTENS

LIST OF FIGURES

CHAPTER 2

CHAPTER 3

CHAPTER 4

LIST OF TABLES

CHAPTER 2

CHAPTER 1

INTRODUCTION

Fuel cell (SOFC) has been dubbed as a clean technology for future sustainable energy systems, which directly coverts chemical energy into electrical energy efficiently by electrochemical reaction of hydrogen and oxygen. The high operating temperature not only accelerates the electrochemical reaction but also offers more fuel flexibility –from internal reforming of hydrocarbon fuel to more tolerance of fuel impurities. However, the high temperature corrosion and oxidation of metallic components in the stack and balance of plant (BOP) component materials can lead to severe degradation of SOFC performance [1-6]. Chromium vapor species form at the exposed oxide surfaces of the metallic interconnects, stack manifold, air delivery tubes and high temperature heat exchangers, and enter the stack with the incoming air, and subsequently react with the bulk air electrode material either to form a stable compound or deposit as stable chromium oxide at the electrochemical triple phase boundary, which poisons and deactivates the air electrode. This has been studied and recognized as a major source of electrical performance degradation in cells [7-9]. Because of their critical role in long term stable performance of SOFC interconnects and BOP components, Cr evaporation and degradation characteristics of chromia and alumina forming alloys have been investigated reasonably extensively [10-26]. However, most of these studies have been directed towards the evaluation and minimization of the Cr evaporation problem of interconnects, by investigating suitable alloys [10-16, 19-27] or by application of coatings [16, 24, 28-37]. Limited studies have investigated chromia and alumina forming alloys for addressing the high temperature scaling and Cr evaporation in the SOFC-BOP [10, 13]. The study by Stanislowski et al. [10] serves as the primary source on alumina and chromia forming alloys and aluminized alloys for BOP application. The study suggests these alloys to be promising for BOP application with regard to Cr evaporation. However, this study was carried out at a single humidification level of 1.8%

(60% humidity at 25 ^{o}C (298 K)) and included limited microscopic examination of oxide scale and metal cross-sections for correlating the scale morphology with Cr evaporation kinetics. Gerdes and Johnson [13] have characterized the broad surface morphology and elemental composition of the oxide scales (by SEM/EDS) for calculation of the Cr evaporation after different durations of exposure in dry air only. It is necessary to study physico-chemical characteristics of the oxide scales and the role of water vapor.

This thesis presents an investigation of the influence of surface oxide on chromium evaporation of chromia and alumina forming nickel and iron base alloys. Evaluations of different coatings in terms of coating qualities, interdiffusion and chromium evaporation were conducted.

CHAPTER 2

LITERATURE REVIEW

2.1. *Solid Oxide Fuel Cells (SOFCs)*

In comparison with the conventional combustion based technologies for electrical power generation, solid oxide fuel cell (SOFC) power systems offer well documented advantages in terms of improved power plant efficiency (chemical to electrical), fuel flexibility (from coal to hydrocarbon to hydrogen), and reduction in the carbon foot print and emission of criteria pollutants (PM's, SOx, NOx and VOC) [1-3]. A basic SOFC system flow sheet is shown in Fig. 2.1. The core component of a SOFC system is the SOFC stack that was built up by connecting basic SOFC units-single cells.The basic SOFC unit is composed of four major components: electrolyte, cathode, anode, and interconnect. Fig. 2.2 gives a schematic of planar bipolar SOFC basic unit, including the various components.

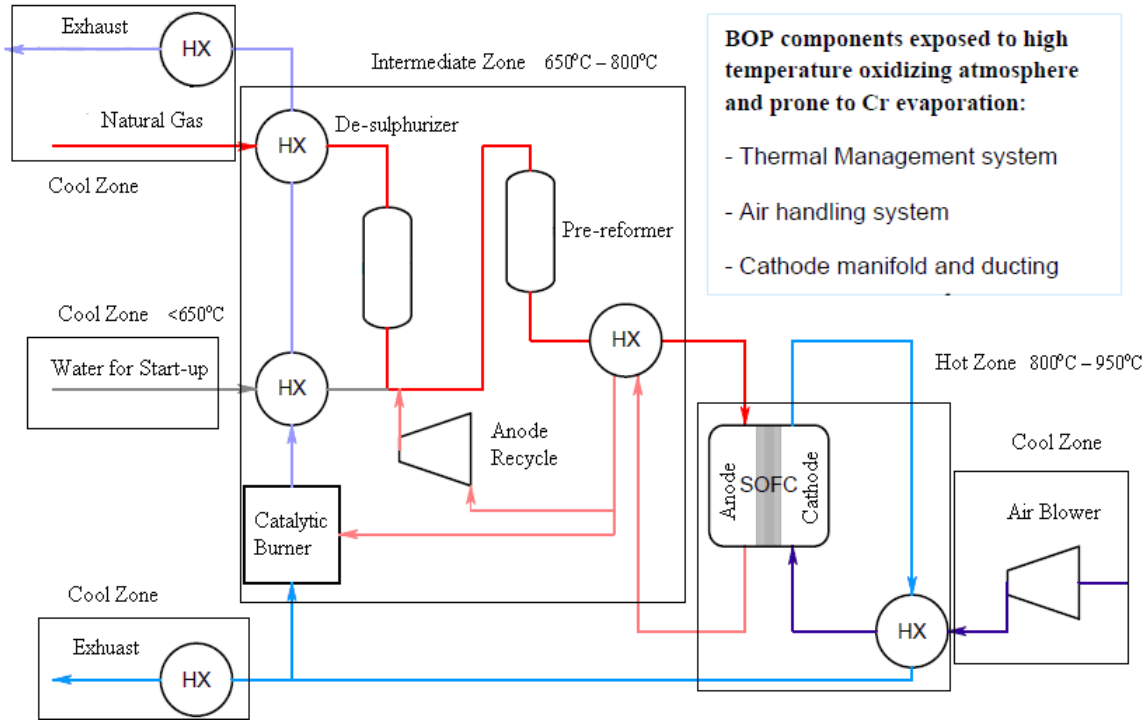

Fig. 2.1 Schematic of solid oxide fuel cell system

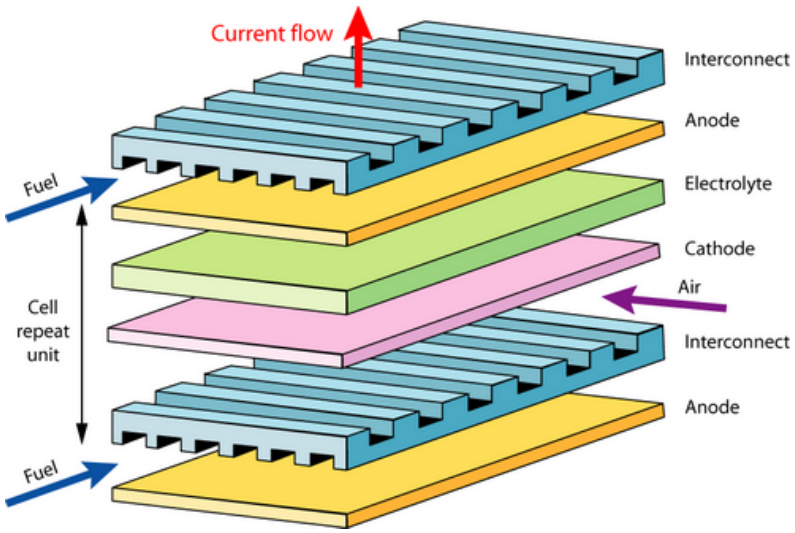

Fig. 2.2 Schematic of SOFC basic units [38]

2.1.1 Working Principle

Generally, SOFCs use a ceramic electrolyte which is capable of conducting negatively charged oxygen ions (O^{2-}) through neighboring oxygen vacancy sites ($V_O^{\cdot\cdot}$) without conducting electrons. The movement of oxygen ion is thermally activated hopping; it is therefore easy to understand the oxygen ionic conductivity of the electrolyte increases with the increase of the fuel cell operation temperature. Fig. 2.3 shows a schematic of the operation of a solid oxide fuel cell with an oxygen ion conducting electrolyte. The operation of the solid oxide fuel cell is straightforward: oxygen atoms are reduced on the porous cathode surface by electrons; then oxygen ions diffuse from cathode side to anode side of the SOFC via dense and thin electrolyte, at the anode side, oxygen ions react with hydrogen (fuel) and give off electrons to the external circuit and electrons travel back to the cathode completing the circuit. Since the movement of oxygen ion is thermally activated hopping, it is therefore easy to appreciate the oxygen ionic conductivity of the electrolyte increases with the increase of the fuel cell operation temperature.

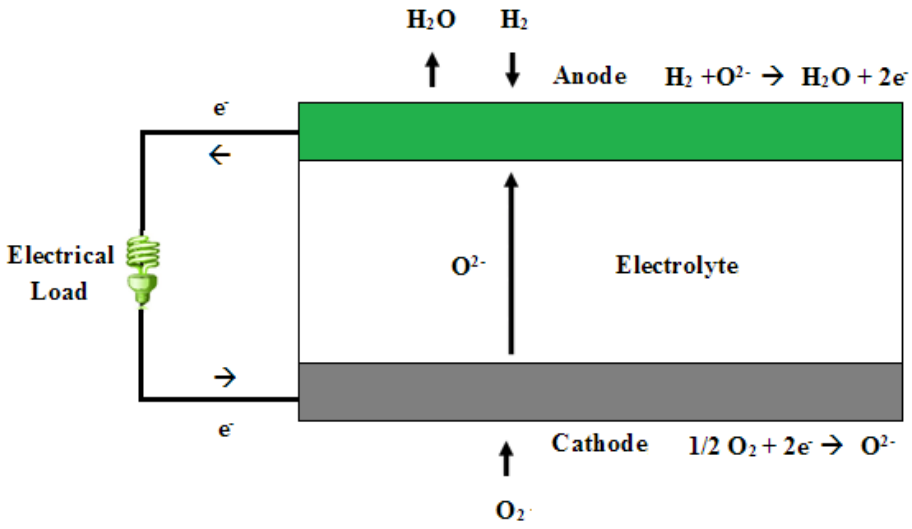

Fig. 2.3 Schematic showing the operation of a solid oxide fuel cell with an oxygen ion conducting electrolyte

The theoretical open circuit voltage (OCV) of the fuel cell is:

$$V_{voc} = \frac{-\nabla G}{zF} \qquad (2.1)$$

Where □G is the Gibbs free energy formation of reaction

$$H_2 + ½\ O_2 \rightarrow H_2O \qquad (2.2)$$

z is the number of electrons produced per mole of the hydrogen (fuel), F is Faraday constant. In practice, fuel cell operating voltage is always smaller than open circuit voltage (OCV) due to the factors: activation losses, Ohmic losses, and mass transport related losses [27]. At higher temperature, the voltage difference is often smaller, thus fuel cell performance often increases with increasing temperature; although theoretical open circuit voltage (OCV) often decreases with increasing the operating temperature.

2.1.2 Component Materials

The development of solid oxide fuel cells (SOFCs) is built on the new discoveries and improvements of component materials. Although higher operating temperature renders higher efficiency, the materials challenges (stability, performance, compatibility and cost) limit the application and commercialization of the SOFCs. Recently, there has been significant progress in reducing the operation temperature of SOFC from traditional 1000 °C to intermediate temperature range of 600 to 800 °C [39-50]. Lowering the operation temperature not only improves the long-term stability of the SOFC but also reduces the system cost by using less costly metal alloys as the interconnect [51] and BoP components. Further reduction in operation temperature (≤600 °C) would bring many benefits such as easier sealing, less insulation required, smaller thermal mismatch, and rapid startup with less energy consumption. However, such effort would dramatically increase the resistivity and polarization losses of the electrolyte and electrode. To compensate for the increase in ohmic losses at lower temperatures, electrolytes with higher ionic conductivity or thinner films are used [47, 52, 53]. This section gives a brief overview of the different components of SOFCs and the materials used.

Electrolyte

The electrolyte is an ionic membrane which is capable of conducting negatively charged oxygen ions (O^{2-}) through the oxygen lattice (oxygen vacancy) of the material. Apparently, fast ionic transport is one of the most important requirements of the electrolyte materials. The electrolyte, which separates the fuel and oxygen chambers, must also be dense to prevent gas diffusion. And it should be thermodynamic and mechanical stable over a wide range of temperatures and oxygen partial pressures. In addition, they must have compatible thermal expansion coefficients (CTE) with that of electrodes and have negligible interaction with electrode materials under operation and fabrication conditions. These requirements limit the choice of electrolyte materials. For low-temperature (400–600°C) SOFCs, ceria electrolyte is often

used, while for intermediate-temperature (600–800°C) SOFCs, zirconia, particularly yttria stabilized zirconia (YSZ), electrolyte is often chosen [54-56].

Cathode

The cathode is the electrode on the oxygen (air) side of the electrolyte, where oxygen is reduced via the following electrochemical reaction in Kroger-Vink notation [57]:

$$\frac{1}{2}O_2\ (gas) + 2e' + V_O'' \rightarrow\ O_O^X \qquad (2.3)$$

In SOFCs, oxygen is reduced by the addition of two electrons, and the resultant ion is incorporated into vacancies in the material. There are two classes of cathode materials with respect to the electronic and ionic conductivity. For cathode like Sr-doped $LaMnO_3$ (LSM, $La_{1-x}Sr_xMnO_{3-\delta}$), it is predominant electronic conductor with little ionic conductivity; the ionic diffusion in the cathode is limited, thus the reaction most likely take place in the vicinity of the triple phase boundary (TPB) between gas, cathode, and electrolyte. If the cathode has substantial ionic conductivity in addition to electronic conductivity, called mixed ionic electronic conductors (MIEC), however, the reaction can occur at other sites than the TPB, opening up more potential reaction sites. Example of such cathode is Sr-doped $LaCoO_3$ (LSC, $La_{1-x}Sr_xCoO_{3-\delta}$), where reaction can even happen at electrode surface. For thin film electrolyte SOFC, the overall losses of the cell are generally dominated by the polarization losses for the O_2 reduction on the cathode [58]. Due to the high-activation energy and slow-reaction kinetics for the O_2 reduction reactions (compared with the hydrogen oxidation reactions), cathodic polarization loss can be as high as 65% of the total voltage loss for intermediate-temperature SOFCs [25]. Thus, development of high performance and high stability cathodes becomes critical for intermediate-temperature SOFC technologies.

Anode

The anode is the electrode on the hydrogen (fuel) side of the electrolyte, where electrochemical oxidation of fuels happens. Another function of the SOFCs anode is the internal reforming or partial oxidation of the fuel when hydrocarbon fuel is used. The chemical and electrochemical processes often take place preferentially at certain surface and interfacial sites or triple-phase boundaries (TPBs). The anode polarization, the resistance to these electrode processes, is determined by intrinsic surface catalytic activities toward fuel oxidation and reforming, the microstructure, morphology, and transport properties of the electrode materials. Graphite, platinum, iron, cobalt and nickel has been used as anode materials at the early stage of SOFC development. Currently, the commonly used cathode material is nickel-yttria stabilized zirconia (Ni-YSZ), which is a porous cermet anode that possesses good electronic conductivity and catalytic activity (from Ni metal phase). The YSZ matrix prevents the Ni phase from coarsening, and offers a conduction path for oxide ions and thus may extend the active zones for anode reactions [59, 60].

Metallic Component Materials

The endeavors of reducing the operating temperature make it possible to replace ceramic interconnects with metallic materials in the planar SOFCs. The metallic materials, compared with ceramic counterpart, have better fabricability and lower cost. However, metallic interconnects as well as BoP components continue to be degraded despite the lowered temperature, and their corrosion products also contribute to the electrical degradation in the fuel cell [28, 61, 62]. Therefore, the identification and fabrication of suitable interconnect as well as BoP materials still remains as a major challenge in the development of SOFCs [17, 26]. The primary function of the metallic interconnect is to conduct electrical current; besides good electrical conductivity, the interconnect material must be chemically and mechanically stable for operation at high temperatures for long periods of time. Material requirements for the BoP remain

significantly different from that of the cell interconnects as the need to match the thermal expansion coefficients and to form electronically conducting oxides does not exist in the case of BoP. Material selection is primarily based on the requirements imposed by the high temperature strength, fabricability, long term creep, and corrosion resistance as well as cost effectiveness. The high temperature corrosion resistant alloys used in SOFCs, in terms of chemical composition, can be categorized as nickel and iron base austenitic and ferritic alloys. Conventionally, oxidation and corrosion resistance is achieved by forming external oxide scales of chromia (Cr_2O_3) or alumina (Al_2O_3). Chromia forming alloys are often chosen as interconnect materials because of electronically conducting oxides formed on the alloys surface. Chromium evaporation from the bulk interconnect materials, namely ferritic chromia forming alloys, as well as that from the electronically conducting interconnect coatings that consist of cobalt-manganese spinel have been extensively studied. Effectiveness of the interconnect alloy chemical composition and surface coatings, as a barrier against chromium evaporation to provide the desired life time of 40,000 h, has been studied under isothermal and thermal cyclic conditions [63, 64]. Unlike the cell interconnects; BoP components can be fabricated from a large number of nickel and iron base austenitic and ferritic alloys capable of forming protective chromia or alumina scale. Still, the selected materials must demonstrate adequate resistance to chromium evaporation since chromium vapor from BoP components can be transported to the cathode and contribute to the degradation of the cell. Surface coatings capable of forming alumina scale also offer the potential for such applications. Because of their critical role in long term stable performance of SOFC interconnects and BoP components, Cr evaporation and degradation characteristics of chromia and alumina forming alloys have been investigated reasonably extensively [10-15]. However, most of these studies have been directed towards the evaluation and minimization of the Cr evaporation problem of interconnects, by investigating suitable alloys [10-15] or by application of coatings [16]. Limited studies have investigated chromia and alumina forming alloys for addressing the high temperature scaling and Cr evaporation in the SOFC-BoP. The study by Stanislowski et al. [10] serves as the primary source on alumina and chromia forming alloys and aluminized alloys for BoP application. The study suggests these alloys to be promising for BoP application with regard to Cr

evaporation. However, this study was carried out at a single humidification level of 1.8% (60% humidity at 25 ^{o}C (298 K)) and included limited microscopic examination of oxide scales and metal cross-sections for correlating the scale morphology with Cr evaporation kinetics. Gerdes and Johnson [13] have characterized the broad surface morphology and elemental composition of the oxide scales (by SEM/EDS) for calculation of the Cr evaporation after different durations of exposure in dry air only. It is necessary to study the physicochemical characteristics of the oxide scales and the role of water vapor.

2.2 High Temperature Alloys

The definition of 'high temperature' is different in different context. In the context of high temperature oxidation and corrosion of metals, the 'high temperature' refers to 500 ^{o}C and above [65, 66]. The temperature under consideration would be high enough to vaporize the water and cause significant growth of the corrosion or oxidation product. High temperature alloys are often selected for their corrosion resistance, but they are at the same time constructional materials. Mechanical properties such as high-temperature strength, ductility and toughness, are thus also important.

2.2.1 Stainless Steel

Stainless steel is a term used to describe an extremely versatile family of engineering iron-base alloys, containing a minimum of 10.5% chromium [67]. They are often designed with oxidation, corrosion and heat resistant properties and with certain degree of machinability. In unpolluted atmospheres, chromium in stainless steels reacts with oxygen and moisture in the environment to form a protective, adherent and coherent, chromium rich oxide film which is generally very thin (several nanometers) and often referred

to as passive layer. The corrosion resistance of the stainless steels originates from such a passive layer which helps to inhibit further corrosion and oxidation of the steel.

The stainless steels can be divided into four categories based on their microscopic (crystal) structures: austenitic, ferritic, martensitic, and duplex steels (consisting of mixture of ferrite and austenite).

Austenitic stainless steels contain a maximum of 0.15% carbon, a minimum of 16% chromium and sufficient nickel and/or manganese to retain a face center cubic (FCC) structure at all temperatures from the cryogenic region to the melting point of the alloy. Corrosion performance of austenitic stainless steels may be tailored by careful alloy adjustment in order to survive a wide range of service conditions. In general, austenitic stainless steels exhibit superior corrosion resistance to both ferritic and martensitic. Austenitic stainless steels cannot be hardened by heat treatment; instead they are often strengthened by work-hardening. They offer excellent formability and their response to deformation can be controlled by chemical composition. They are not subject to an impact transition (ductile to brittle transition) at low temperatures and possess high toughness to cryogenic temperatures. They exhibit greater thermal expansion and heat capacity, with lower thermal conductivity than other stainless or conventional steels Austenitic stainless steels are commonly used for applications at elevated temperature because of their good creep and oxidation resistance. Austenitic stainless steels are often described as non-magnetic, but may become slightly magnetic when machined or worked.

Ferritic stainless steels consist of chromium and iron with very little or no nickel with a body center cubic (BCC) structure. They also contain very little carbon and are non-heat treatable; like austenitic stainless steels, ferritic stainless steels exhibit superior corrosion resistance to martensitic stainless steels and possess good resistance to oxidation. Unlike austenitic stainless steels, ferritic stainless steels are ferromagnetic and subject to an impact transition (toughness to brittle transition) at low temperatures, nevertheless, they possess adequate formability and toughness. Their thermal expansion and other thermal properties are similar to conventional steels. The toughness is limited for thicker dimensions, ferritic

stainless steels are readily welded in thin sections, and they suffer grain growth with consequential loss of properties when welded in thicker sections.

Martensitic stainless steels consist of carbon (0.2-1.0%), chromium (10.5-18%) and iron. Unlike austenitic and ferritic stainless steels, martensitic stainless steels may be hardened by heat treatment to provide a range of mechanical properties. Both their corrosion resistance and toughness are moderate, like ferritic stainless steels, martensitic stainless steels are ferromagnetic, subject to an impact transition at low temperatures but possess poor formability. Their thermal expansion and other thermal properties are similar to ferritic stainless steels.

Duplex stainless steels have a microstructure consisting of austenite and ferrite; they are characterized by high strength, good toughness, very good corrosion resistance in general. They are also ferromagnetic and subject to an impact transition at low temperatures. Their thermal expansion lies between that of austenitic and ferritic stainless steels, while other thermal properties are similar to plain carbon steels. Formability is reasonable, but higher forces than those used for austenitic stainless steels are required.

The effects of the alloying elements

Alloying elements are often added to modify the properties and performance of the steel. It is the combined effect of all the alloying elements and, to some extent, the impurities that determine the property profile of a certain steel grade. The effects of the some important alloying elements on the materials properties are discussed. Fig. 2.4 shows the composition and property linkages in the stainless steel family of alloys. It should also be noted that the effect of the alloying elements differs in some aspects between the hardenable and the non-hardenable stainless steels.

Chromium

Chromium is by far the most important alloying element in stainless steel. A minimum of 10.5% chromium is required for the formation of a protective layer of chromium oxide on the steel surface. The corrosion and oxidation resistance of the stainless steel increases with increasing chromium content. Chromium promotes a ferritic structure and therefore is described as a ferrite stabilizer.

Nickel

Nickel improves general corrosion resistance and promotes the austenitic structure (it is considered as an austenite stabilizer). Stainless steels with nickel (8-9%) have a fully austenitic structure, further increase in the nickel content improves both corrosion resistance (especially in acid environments) and also increases ductility and toughness (better workability). Nickel is also used to form the intermetallic compounds that are used to increase the strength in precipitation hardening steels.

Molybdenum (Tungsten)

Molybdenum substantially increases resistance to both local (pitting, crevice corrosion, etc) and general corrosion. Molybdenum and tungsten promote the ferrite structure, when used in austenitic alloys, must be balanced with austenite stabilizers in order to maintain the austenitic structure. In martensitic steels it will increase the hardness at higher tempering temperatures due to its effect on the carbide precipitation.

Nitrogen

Nitrogen is a very strong austenite former, it also substantially increases the mechanical strength and the resistance to localized corrosion. In ferritic stainless steels nitrogen will strongly reduce toughness and corrosion resistance. In the martensitic and martensitic-austenitic steels nitrogen increases both hardness and strength but reduces the toughness.

Carbon

Carbon is also a strong austenite former, it enhances strength (especially, in hardenable martensitic stainless steels), but may reduce the corrosion resistance by the formation of chromium carbides.

Titanium (Niobium & Zirconium)

Where it is not desirable or, indeed, not possible to control carbon at a low level, titanium or niobium may be used to stabilize stainless steel against intergranular corrosion. As titanium (niobium and zirconium) have greater affinity for carbon than chromium, titanium (niobium and zirconium) carbides are formed in preference to chromium carbide and thus localized depletion of chromium is prevented. These elements are ferrite stabilizers.

Sulfur

Sulfur is added to improve the machinability of stainless steels. As a consequence, sulfur will substantially reduce corrosion resistance, ductility and fabrication properties, such as weldability and formability

Cerium (Yttrium)

Cerium and similar rare earth metals are added in small amounts to stainless steels or high temperature alloys to improve the oxidation and corrosion resistance and adhesion of the oxide film at high temperatures.

Manganese

Manganese is generally considered as an austenite stabilizer and used in stainless steels in order to improve hot ductility. However, at high temperatures manganese will stabilize ferrite. Manganese increases the solubility of nitrogen and is used to obtain high nitrogen contents in austenitic steels.

Silicon

Silicon improves resistance to oxidation and is also used in special stainless steels exposed to highly concentrated sulfuric and nitric acids. Silicon is a ferrite stabilizer.

Aluminum

Aluminum improves oxidation resistance, if added in substantial amounts. It is used in certain heat resistant alloys for this purpose. In precipitation hardening steels aluminum is used to form the intermetallic compounds that increase the strength in the aged condition.

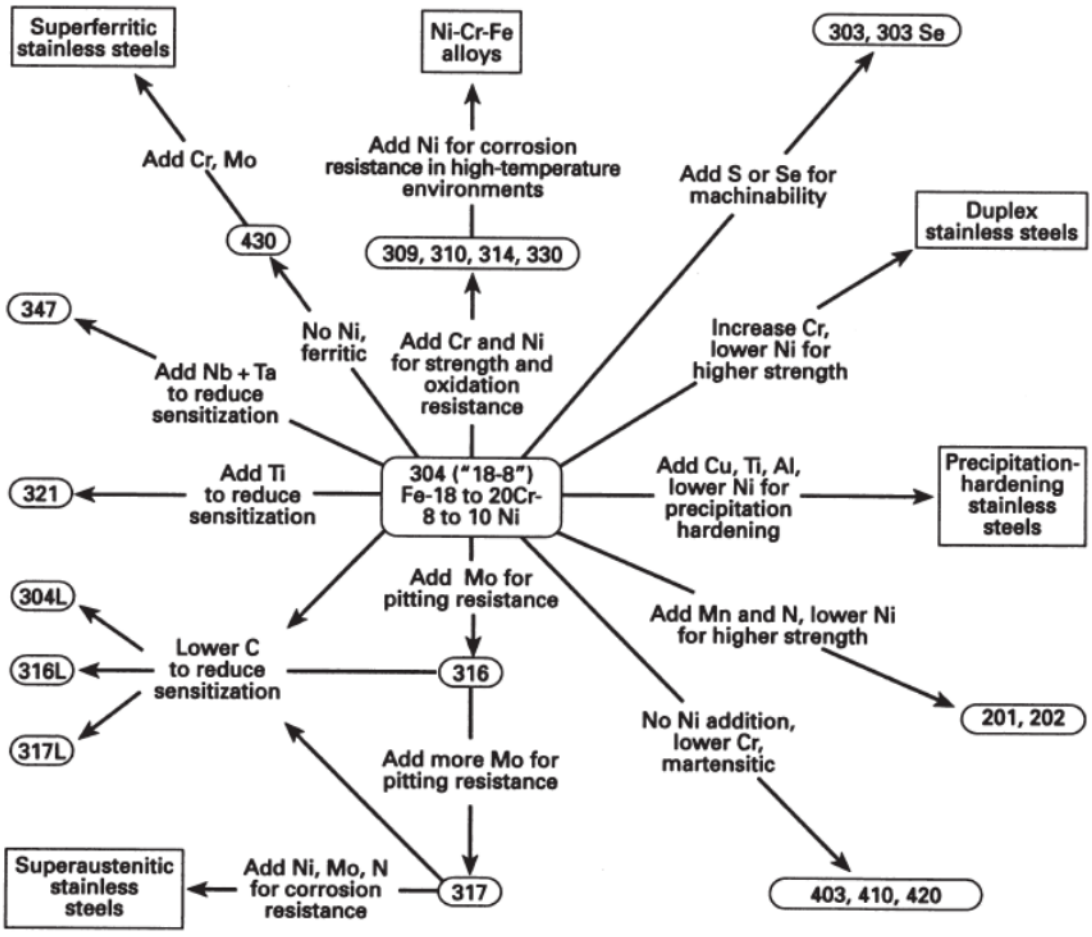

Fig. 2.4 Composition and property linkages in the stainless steel family of alloys [68]

2.2.2 Superalloy

Superalloys are metallic materials for elevated temperature service, usually based on group VIIA elements of the periodic table, which are proven to have great capabilities to maintain mechanical strength and creep resistance as well as structural and surface stability from room temperature to 0.8 Tm (melting point) of the alloy [69]. Superalloys are generally for most demanding high temperature applications such as steam power plants, petroleum refineries, gas turbines (land, marine and air), rocket engines and nuclear power plants, just to mention a few from the broad spectrum of high-temperature applications where the resistance to deformation and stability are prime requirements. Other high temperature properties include corrosion and oxidation resistance, high creep rupture strength, low thermal fatigue and low coefficient of thermal expansion are also required.

There are three main groups of superalloys: nickel base, cobalt base and iron base. Ni-base alloys are the most widely used for the hottest parts in high-temperature applications and they have the most complex, subtle and sophisticated metallurgy.

Ni base superalloys usually contain at least 12 to 13 basic alloying elements and 10 more tramp (trace) elements such as manganese, silicon, phosphorus, sulfur, oxygen and nitrogen which should be carefully controlled to minimize their deleterious effects.

The major phases present in the structure of a nickel base superalloy are:

Gamma matrix (γ - FCC austenite)

The continuous matrix of Ni base Superalloy is an FCC Ni-base austenitic phase, usually alloyed with a high percentage of solid-solution elements such as Co, Mo, Cr, Ta, W, Ti, and Al for solid solution strengthening.

Gamma prime (γ')

γ' is the major precipitate phase, coherent with the austenite matrix. The chemical additions of aluminum and titanium promote the creation of the γ' phase; γ' is typically in the form of Ni_3 (Al, Ti) with nickel and aluminum dominating. Unlike the strengthening that is developed by high hardness carbides, the inherent ductility of γ', which acts as a barrier to dislocation motion for strengthening, helps prevent cracking. Interestingly, strength of γ' increases with increase of the temperature, which makes Ni base superalloy a most appealing material for high temperature industrial applications.

Carbides

Carbon presence in superalloys often reacts with refractory elements to form primary stable carbides, which preferentially form at grain boundary to limit grain boundary sliding for increased grain boundary strength (creep resistance) at high temperatures. However, previous studies showed detrimental effects on ductility from grain boundary carbide.

Borides

Additions of boron are also used to increase the cohesive bonding to limit the grain boundary tearing under creep rupture failure.

Topologically close packed (TCP) phases

The TCP phases, σ, μ and Laves, commonly formed in Ni-base alloys, are undesirably hard phases having a detrimental effect on the properties of the alloy. Their plate-like morphology is a source for crack initiation and crack propagation leading to brittle failure at relatively low temperatures. Also, they contain a high refractory metal concentration taken from the γ matrix, thus weakening the superalloy.

The developments of alloy processing techniques has led to the development of directional solidification and the production of single crystal superalloys for better performance for gas turbine applications at high temperatures. Through the engineering of optimum mechanical properties, environmental stability has become the limiting factor of the components service life. Generally, the oxidation and corrosion resistance of high temperature superalloys can be achieved by growing a protective external oxide (Al_2O_3 or Cr_2O_3 layers) with small additions of Al and Cr. These scales formed on the alloy surface separate the alloy from the corrosive environment thereby preventing the formation of rapidly growing oxides (e.g. nickel, cobalt or iron) and consequently the corrosive degradation of the metallic component. α-Al_2O_3 is most desirable protective scale type, it is slow growing, dense, relatively inert and has low volatility compared to Cr_2O_3 for applications at temperature higher than ~ 950 °C; while at lower temperatures, Cr_2O_3 scale is often formed. In addition, the scale also must be adherent in order to achieve extended oxidation resistance lifetimes. Usually, for good scale adhesion, a reactive element (Zr, Y or Hf) is added to the alloy.

2.3 High Temperature Oxidation of Alloys

The characteristic of the oxidation reaction is that the reaction is heterogeneous and does not proceed exclusively in the interior of one phase. Heterogeneous reactions occur between two immiscible phases and usually result in the formation of a new phase. Such reaction can occur between the oxidants in the gas phase (or liquid phase) and a solid phase (metal or alloys) with formation of normally oxide phase. At low temperatures, the process of oxide phase formation is slow but at high temperatures such oxidation reaction is accelerated. The oxidation process is generally governed by solid-state diffusional transport of atoms or ions and electrons through the oxide phase (scale), when a continuous oxide scale is assumed. High temperature oxidation resistance is often required for alloys service at high temperatures. The

knowledge of oxidation theory is a must when designing or/and selecting alloys for high temperature applications

2.3.1 Oxidation Mechanism and Kinetics

The oxidation phenomenon is generally governed by both the principle of thermodynamics and solid state diffusion. For most metallic elements, a general reaction between the metal (M) and oxygen (O) in the gas phase can be written as

$$\frac{2a}{b}M + O_2 = \frac{2}{b}M_aO_b \qquad (2.4)$$

The Gibb's free energy ($\Delta G^{'}$) associated with such a reaction is generally negative for a corrosion or oxidation product to form. In practice, it is easier to compare the ΔG^o (standard Gibb's free energy of formation) of different oxides using a Richardson/Ellingham diagram as shown in Fig. 2.5. The values of ΔG^o are expressed as kJ mol^{-1} O_2 so the relative stabilities of various oxides may be compared directly at different temperatures. It is clear from this diagram that elements like aluminum, silicon and chromium that are near the bottom for unit activity of the metal, the oxides of these metals are more stable than the oxides of the elements above. The large affinity for oxygen is one of the criteria of choosing desired alloying elements for oxide scale formation.

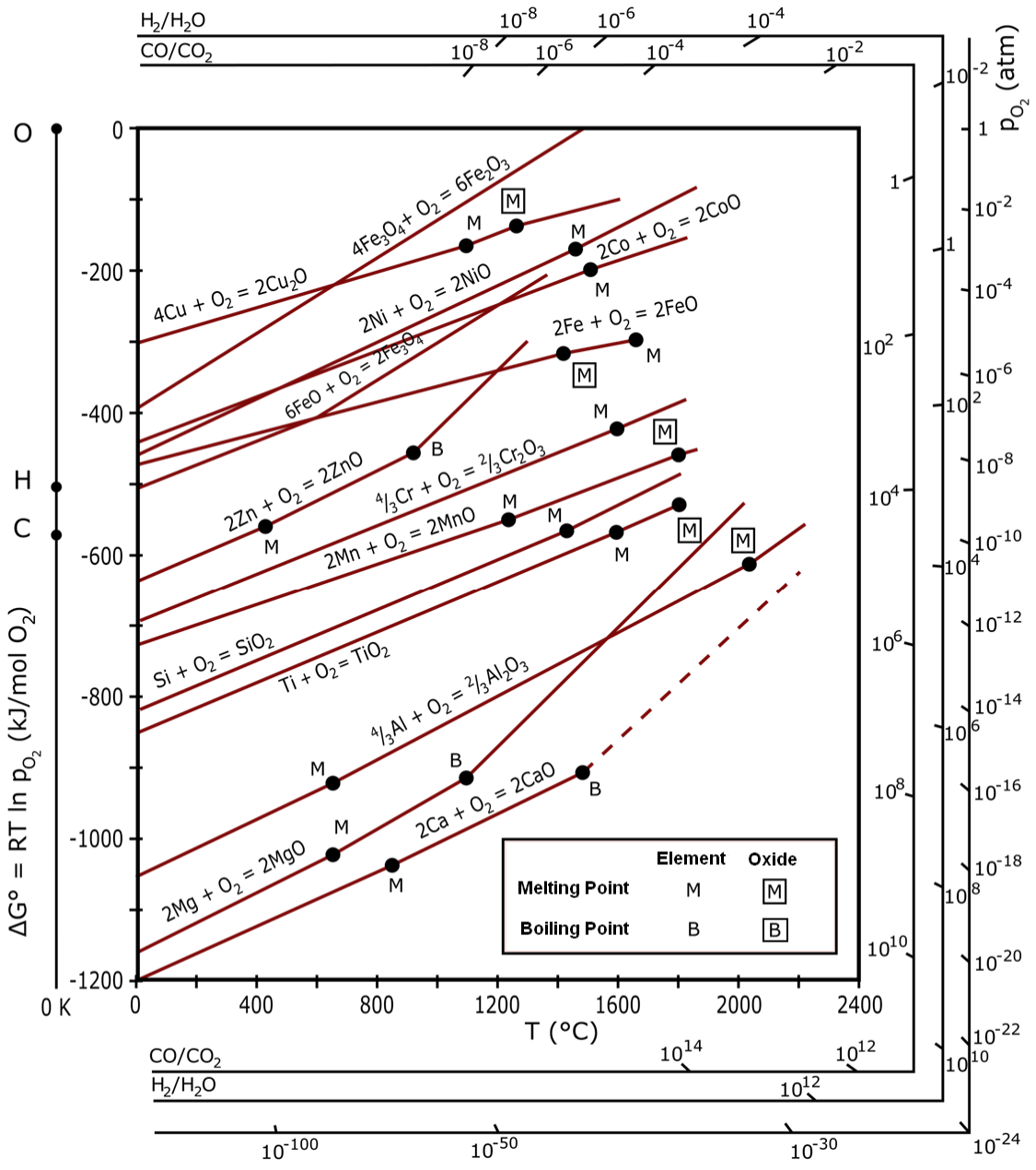

Fig. 2.5 Schematic showing the operation of a solid oxide fuel cell with an oxygen ion conducting electrolyte

Another criterion of choosing desired alloying element is the kinetics of the oxide scale formation need to be relatively slow. After an initial oxide layer is formed, further oxidation of the metal is achieved by solid-state diffusional transport of ions and electrons through the oxide. The driving force for metal cation and/or oxygen anion diffusion through the oxide (scale) is the activity gradient (or chemical potential) created across the scale as demonstrated in Figure 2.6 if several assumptions are made as Wagner did in the calculation [70].

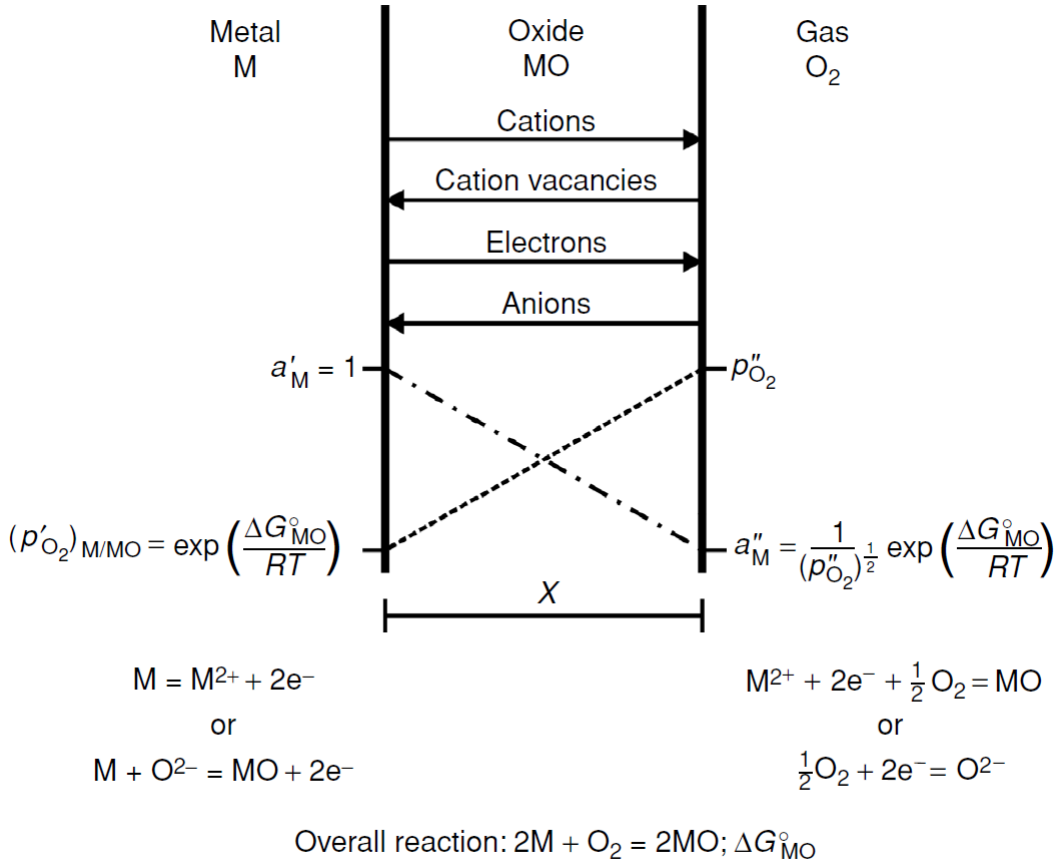

Fig. 2.6 Schematic diagram of species transport and equilibrium reactions

Assuming thermodynamic equilibrium is established at each interface: at the metal-oxide interface, the activity of the metal at the metal-oxide interface is equal to that in the alloy, and the apparent oxygen

partial pressure will be the dissociation pressure for that oxide; similarly at the gas-oxide interface, activity of the metal can be calculated where the oxygen partial pressure is that in the atmosphere.

In theory, two types of ionic transport can co-exist: inward diffusion of the oxygen ions and the other is the outward transport by the cation of the metal species. However in practice, it is possible to ignore the migration of the slower-moving ionic species as the mobilities of the cation and anion species usually differ by several orders of magnitude.

Wagner quantified growth rate as a function of scale thickness and time. As the scale thickens, the diffusion distance increases and ultimately reduces the reactant flux establishing an ever decreasing scale growth rate.

$$x^2 = 2k't \qquad (2.5)$$

Where x is scale thickness, the square of which is proportional to time t, and the proportionality constant is k', which is termed as the parabolic rate constant. Experimentally a similar equation was adopted as continuously monitor oxidation by mass change is easier to achieve.

$$\left(\frac{m}{A}\right)^2 = k''t \qquad (2.6)$$

Where A is the area over which reaction occurs; k'' is also referred to as the practical tarnishing constant or 'scaling constant' and has units of $g^2\ cm^{-4}\ s^{-1}$.

A comparison of parabolic rate constants for selected oxide scales as a function of reciprocal temperature is presented in Fig. 2.7.

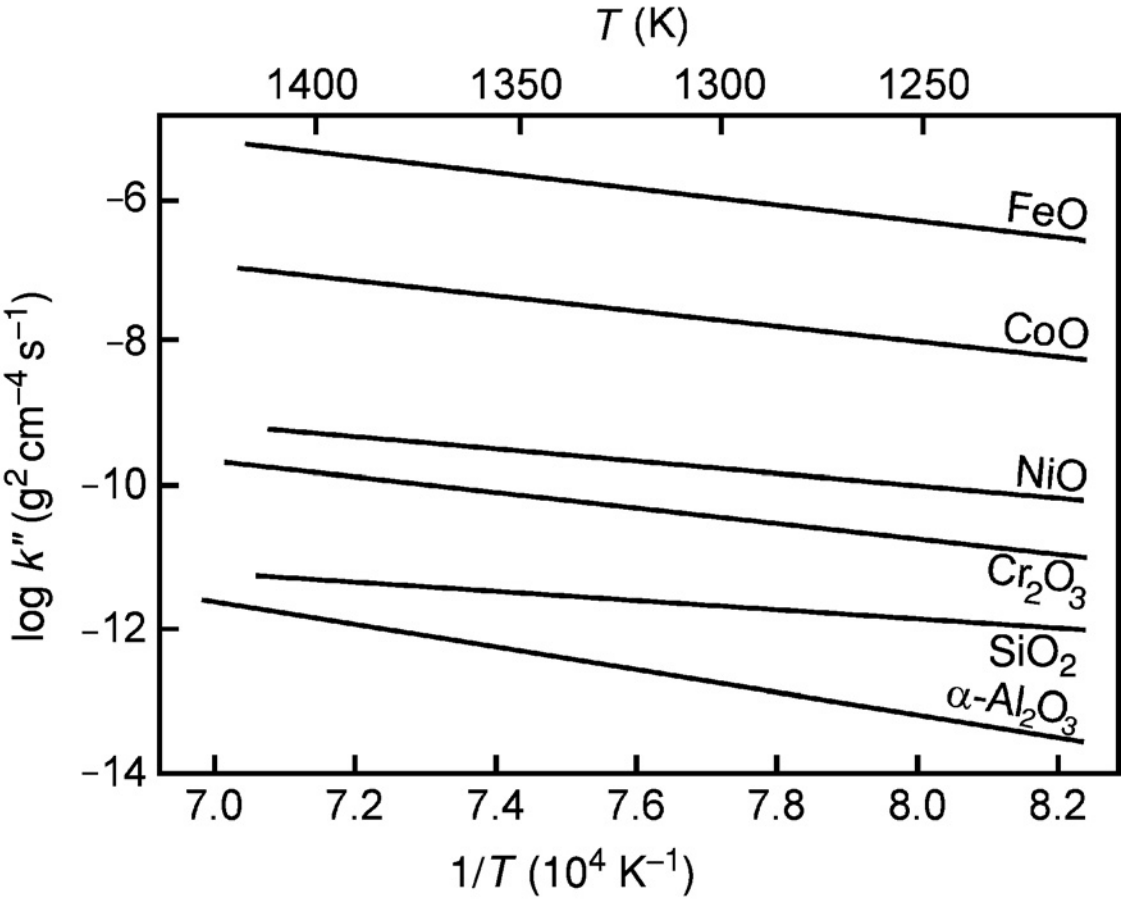

Fig. 2.7 Comparisons of parabolic rate constants for selected oxide scales [65]

2.3.2 Selective Oxidation

The process in which a solute oxidizes preferentially to the parent element and forms a continuous layer on the surface is referred to as selective oxidation. As discussed above, the ability for an alloy to form a protective oxide is both a thermodynamic and a kinetic issue. From thermodynamic point of view, the desired oxide scales need to have large oxygen affinity compared with other elements in the alloy; from kinetic point of view, the desired oxide should also have fairly slow growth rate. In practice, in Ni, Fe, or Co base alloy systems, the desired Cr_2O_3 or Al_2O_3 scale has much lower growth rate compared with the parent metal oxide. During the initial stage of oxidation, all of the elements in the alloy will oxidize and the initial oxide layer formed on the surface will be composed of elements in proportions as they are present in the alloy.

Once this transient oxide forms a continuous layer on the alloy, a drop in oxygen activity at the oxide metal interface will only allow the thermodynamically more stable oxide to continue to form. The capability of the alloy to maintain this oxide depends on the amount of this element in reserve and its ability to diffuse to the scale for further reaction. The concentration in the alloy to achieve this can be represented by

$$N_B^{Critical} = \frac{V_m}{32v} \left(\frac{\pi k_p}{D_B}\right)^{1/2} \qquad (2.7)$$

Where $N_B^{Critical}$ is the concentration of the oxide forming element in the alloy, D_B is diffusivity of element *B* in the alloy, k_p is the parabolic rate constant, V_m is the is the specific volume of the metal and v is the ratio of oxygen to *B* in the oxide. The selective oxidation of elements which form a slowly growing, protective layer is the basis for the oxidation protection of all alloys and coatings used at high temperature. These contain a sufficiently high concentration of a solute (e.g., Cr, Al, or Si) to produce an external layer of a stable oxide scale.

2.3.3 Effects of Water Vapor

Water vapor is present in many gases of industrial importance. It is well known that most technical steels oxidize faster in water vapor or in air or combustion gases containing water vapor than in dry oxygen [71]. Water vapor can interact with metals or alloys in many ways. It can participate in surface reactions, thereby modifying the scale–gas interface; it can also change the microstructure, morphology, properties and growth rate of the scale formed. In reality, the surface reactions induced by water vapor are often overwhelmed by changes in the scale microstructure, morphology, and diffusion or transport properties. In principle, there are mainly three ways water vapor can incorporate in the mass transfer processes within the scale: (1) gas transport, which is within cracks, voids or cavities in the scale; (2) molecular transport, which is long grain boundaries that are affected by water vapor; (3) ionic transport, which is possible achieved by dissolving hydrogen into oxide and affecting defects concentrations.

Importantly enough, water vapor can directly react with oxide scale and form volatile metal hydroxide species [72].

$$MO_x + nH_2O = MO_{x+n}H_{2n} \quad (2.8)$$

In addition, simultaneous oxidation and hydration sometimes occurs

$$MO_x + \ nH_2O\ (g) + \ mO_2\ (g) = \ MO_{x+n+2m}H_{2n} \quad (2.9)$$

2.4 Chromium Evaporation and Transport

2.4.1 Basis of Chromium evaporation

The corrosion of chromium-containing materials in oxidizing environments via the formation of volatile species (mainly in Cr^{6+} form) has both broad technological and environmental implications. The hexavalent chromium, namely chromium VI, refers to chemical compounds that contain the element chromium in the +6 valance state; they are considered to be genotoxic carcinogens which need special attention when handled [73]. In addition, chromium vapor species form, in the presence of air and water vapor , at the exposed oxide surfaces of the metallic interconnects, stack manifold, air delivery tubes and high temperature heat exchangers, and enter the stack with the incoming air, and subsequently react with the bulk air electrode material either to form a stable compound or deposit as stable chromium oxide at the electrochemical triple phase boundary, which poisons and deactivates of the air electrode (cathode), hence degrade the performance of the fuel cell. It remains as a major technical challenge in the development of SOFCs. In addition, the effects of Cr-related degradation have also been reported for the contact layer of Solid Oxide Electrolysis Cells (SOEC) cathodes. A recent study shows the concentration profile of Cr in SOEC which is quite different from the concentration of Cr seen in the SOFC device [74]. In the SOEC, because oxygen flows away from Oxygen-electrode-electrolyte interface, chromium uniformly diffuses into the cell. In SOFC, the direction of oxygen flow is reversed and chromium diffuses discretely in various regions of the cell. In the case of SOEC, the formation of a less conducting oxide layer forming between the contact layer and interconnect was suggested to be responsible for the degradation of the cells due to loss in the electronic path from interconnect to the cathode. Also, the Cr loss and depletion in Cr containing alloys due to evaporation in oxidizing environments at high temperature, especially in the presence of water vapor, can lead to accelerated corrosion, metal loss, and degradation of mechanical strength [75, 76]. Furthermore, the deposition of chromium oxide can degrade the performance of the catalysts used in steam methane reformers [77]. Finally, volatile chromium species

formed in atmospheric pressure chemical vapor deposition reactors used in the semiconductor industry can contaminate processed wafers, causing increased defects rates [78]. CrO_3, $CrO_2(OH)$, $CrO_2(OH)_2$, have all been experimental identified as the major volatile chromium species in terms of chromium evaporation. Several studies have also showed $CrO_2(OH)_2(g)$ is the dominant vapor species above chromium-containing materials exposed to oxygen and water vapor across a wide range of temperatures [79-83].

Vaporization of chromium oxide and condensation of chromium species are shown below in equations:

Vaporization reactions: $\frac{1}{2}\ Cr_2O_3(s) + H_2O\ (g) + \frac{3}{4}\ O_2\ (g) = CrO_2(OH)_2\ (g)$ (2.10)

$\frac{1}{2}\ Cr_2O_3(s) + \frac{1}{2}\ H_2O(g) + \frac{1}{2}\ O_2(g) = CrO_2(OH)\ (g)$ (2.11)

$\frac{1}{2}\ Cr_2O_3(s) + \frac{3}{4}\ O_2(g) = CrO_3(g)$ (2.12)

Condensation reactions: $CrO_2(OH)_2\ (g) = CrO_2(OH)_2(s)$ (2.13)

$CrO_2(OH)_2(g) = \frac{1}{2}\ Cr_2O_3(s) + H_2O(g) + \frac{3}{4}\ O_2(g)$ (2.14)

The equilibrium vapor pressure of volatile chromium species can be determined if the equilibrium constants of the above reactions are known. Vapor pressure of three major chromium containing species formed under different humidity levels and temperature can be calculated based on reactions 2.14-2.16. Assuming thermal equilibrium between the solid phase and the gas phase, and also assuming the activity of Cr_2O_3 to be 1 for pure chromium oxide; the activity of chromium containing oxide will be ≤ 1.

$$P_{CrO_2(OH)_2} = {a_{Cr_2O_3}}^{1/2}.P_{H_2O}.P_{O_2}^{3/4}.K_1 \qquad (2.15)$$

$$P_{CrO_2(OH)} = {a_{Cr_2O_3}}^{1/2}.P_{H_2O}^{1/2}.P_{O_2}^{3/4}.K_2 \qquad (2.16)$$

$$P_{CrO_3} = {a_{Cr_2O_3}}^{1/2}.P_{O_2}^{3/4}.K_3 \qquad (2.17)$$

The total vapor pressure of the chromium-containing volatile species is the sum of all the species above ($P_{CrO3} + P_{CrO2(OH)} + P_{CrO2(OH)2}$).

2.4.2 Kinetics of Evaporation

The various techniques for determining vapor pressures can be classified as "static" or "dynamic" methods [84]. The static methods measure directly the pressure exerted by the vapor in equilibrium with its liquid or solid phase while the dynamic methods determine the vapor pressure from the mass loss of the sample. Direct static method measurement of vapor pressure can be used over a wide range of pressure down to 1 Pa [85, 86]. Since the chromium vapor pressure would be far less than 1 Pa, the direct static method seems to be inappropriate. The main experimental techniques in determining vapor pressure data in the low pressure regime are gas saturation or transpiration method using a carrier gas and the molecular effusion method using a Knudsen cell or torsion effusion method. Gas saturation and effusion are generally considered the most accurate experimental method for vapor pressure lower than ~1 Pa. However, the molecular effusion method is often considered as a high vacuum process (water vapor partial pressure $<10^{-5}$ bar), which does not represent the SOFC conditions. Thus, transpiration method becomes most suitable for the chromium vapor measurement. This method is based on the principle that

the vapor species produced over the samples oxidizing at high temperatures, are carried away by a flowing carrier gas and subsequently condensed and collected. If the flowing gas is totally saturated by the evaporating substance, by applying Dalton's law for the carrier gas and knowing the flow rate of the inert gas, the vapor pressure of the substance can be calculated with the formula below [84].

$$\frac{\quad}{\quad}$$

where is the mass loss rate of the transported compound, T is the temperature at which the mass flow rate is measured, is the volumetric flow rate of the inert gas, M is the molecular mass of the substance and R is the gas constant. Fig 2.8 shows the variation of the mass loss rate with volumetric flow rate.

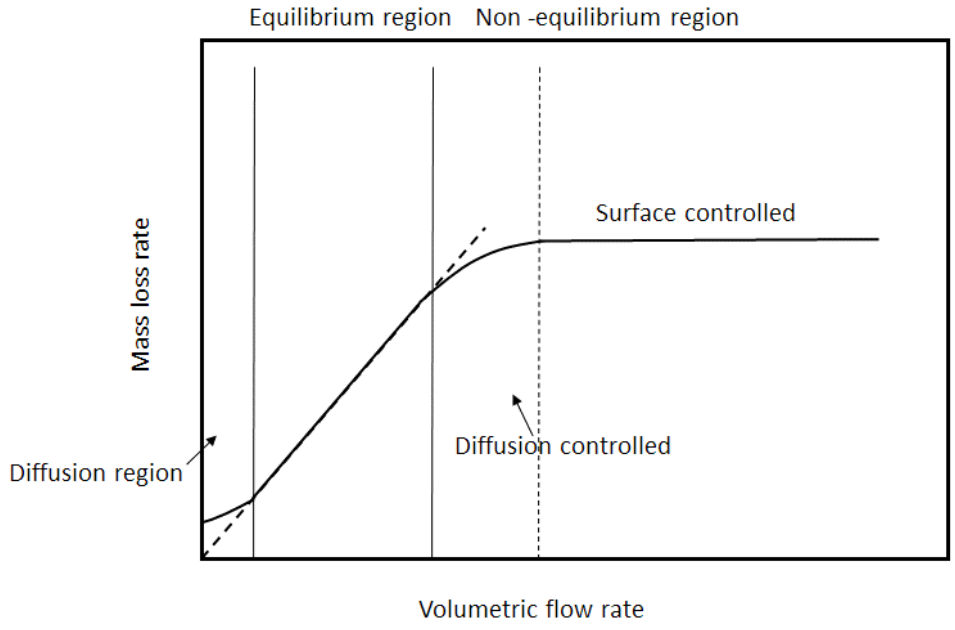

Fig. 2.8 Variation of mass loss rate with volumetric flow rate

In the diffusion region vapor was oversaturated in the carrier gas because of the low flow rate and mass transport. The plateau region where is varied linearly with , which indicates that the carrier gas was saturated with the vapor. An appropriate flow rate will be determined experimentally where the vapor is in thermal equilibrium with the carrier gas when equilibrium partial pressure of the interested volatile

species were to be measured. At higher flow rates, the rate of diffusion of the vaporized species is no longer sufficient in the carrier gas in order to achieve a complete saturation in the reaction chamber. Fig. 2.9 shows the schematic profile of the boundary layer over a disk-shaped sample with a laminar gas flow. A stationary boundary layer forms, which presents the concentration of the vaporized species over the sample surface. The thickness of the interface is dependent on the distance from the leading edge and the gas velocity at a plate-shaped sample.

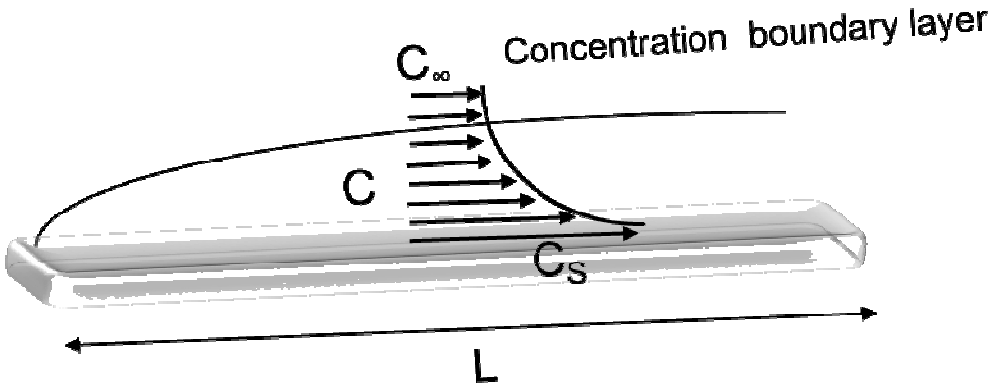

Fig. 2.9 Schematic representation of the concentration boundary layer of the gaseous hydroxide (M-O-H(g)). The volatilization rate is limited by M-O-H (g) transport outward through a laminar gas boundary layer

The mass flow (loss) rate can be calculated using the formula below:

$$J = 0.664 \text{ ——(—— (—)}^{1/2} \qquad (2.19)$$

J mass flow ρ boundary layer gas density
D interdiffusion coefficient volumetric flow rate
L characteristic length r_R tube radius
P_v partial vapor pressure of the evaporating species
M_v molecular mass η gas viscosity

For the chromium evaporation rate measurement, however, the flow rate in the region where surface reaction is rate control process is chosen, where the chromium evaporation rate is independent of the flow rate.

2.4.3 Mitigation

It is shown by many studies that the reduction in Cr vapor pressure and flux could be achieved via Cr-evaporation barrier coatings [34, 35, 87, 88]. It is also demonstrated that Cr evaporation can be mitigated by surface treatment or Cr trapping (gettering) during cell and stack operation [89, 90]. In general, such surface barrier coatings can be classified in terms of conductivity as conductive and non-conductive coatings. Because of the electrical conductivity requirement, conductive coatings are often chosen as Cr-evaporation barrier for interconnects. The appropriate coatings must have adequate conductivity, matching thermal expansion and chemical compatibility with adjacent components, and good stability in both reducing and oxidizing atmospheres. Numerous coating materials have been applied for interconnects, including conductive perovskites, which are also common cathode materials in SOFCs. The advantage of perovskite type coatings is their low thermal expansion coefficient mismatch with alloys and electrode materials; however, it is difficult to achieve fully dense perovskite coatings. Spinel type materials have been considered as coating materials for SOFC interconnects as well. The application of La-chromites, Mn-chromite, or non-Cr containing oxide coatings have been proposed as suitable surface layers on alloy interconnects to reduce Cr evaporation [58, 91]. Such layers could potentially be applied either in a separate fabrication step (e.g., thermal spray) or grown in-situ through suitable modification of the alloy bulk or surface. In general, it is easier to achieve fully dense spinel coatings and the effectiveness of preventing inward transport of oxygen and outward migration of Cr is better when compared with perovskite coatings [92]. One of the promising coating compositions which has been successfully employed in the SOFC technology is the mixed spinel of Mn and Co. It has been demonstrated that the application of $Mn_{1.5}Co_{1.5}O_4$ (MCO) spinel coating on the chromia forming ferritic alloys based ICs could suppress chromium poisoning related degradation of SOFC cathodes [88].

CHAPTER 3

EXPERIMENTAL

3.1. Test Material Preparation

Table 1 shows the chemical composition of all the alloys tested in this study.

Alloy (wt.%)	Nicrofer 6025HT	Aluchrom YHf	AISI 310S	AISI 441	AFA OC-4
Fe	8~11	Bal	Bal	Bal	Bal
Ni	Bal	0~0.3	19~22		25.03
Cr	24~26	19~21	24~26	17.5~18.5	13.96
Al	1.8~2.4	5.5~6	-		3.55
Si	0~0.05	0~0.5	1.5	1.0	0.14
Mn	0~0.1	0~0.5	2	1.0	1.97
Ti	0.1~0.2	-	-	0.1~0.6	0.05
Cu	0~0.1	-	-		0.51
W	-	-	-		0.95
V	-	-	-		0.04
Mo	-	-	-		1.98
Nb	-	-	-	0.3~1.0	2.53
Zr	0.01~0.1	0~0.07	-		-
Y	0.05~0.12	0~0.1	-		-
Hf	-	0~0.1	-		-
P	0.045	-	0.045	0.04	0.013
B	-	-	-		0.0008
N	-	0~0.01	-		0~0.001
S	0.03		0.03	0.15	0.0009
C	0.15~0.25	0~0.05	0.08	0.03	0.101

Table 1 Chemical composition (wt%) of the investigated alloys

Alloy test coupons (25x20x1mm) were ground with SiC paper up to 1200 grit and cleaned ultrasonically in deionized water followed by degreasing and washing with ethanol and acetone.

3.2. Chromium Evaporation Test

3.2.1 Transpiration Method

Chromium evaporation tests were conducted under the simulated oxidant environment of SOFC. The transpiration technique was used to measure the chromium evaporation rate. The method is based on the principle that the vapor species produced over the sample, oxidizing at high temperatures, are carried away by a flowing carrier gas and subsequently condensed and collected. Figure 3.1 shows a schematic of the transpiration apparatus. Before the chromium evaporation test, the constant temperature zone of the furnace was determined and calibrated using a K-type thermocouple. The sample was placed in the quartz tubular reactor assembly within the isothermal zone of the furnace. As indicated in the figure, the quartz reactor design consisted of a capillary opening to prevent the back diffusion of the vapor species. Dry air at a flow rate of 300 standard cubic cm min^{-1} (sccm) was used as a carrier gas during the entire test duration. Among several humidification techniques experimentally evaluated in our laboratory for obtaining a consistent and accurate level of humidification, we selected the room temperature bubbling technique for obtaining 3% H_2O. High accuracy Harvard '33' double syringe positive displacement pumps (Harvard Apparatus, Inc., Holliston, MA, USA) with a flow accuracy 0.1 nano-liter/h of liquid water, was used to deliver the deionized water at a preset rate. A flash evaporator, consisting of a quartz capillary tube, cartridge heater and metallic mesh was designed and fabricated for operation at 200 - 300 ^oC to ensure continuous and complete vaporization as

well as good mixing of the carrier gas with the water vapor. Water vapor present in the carrier gas was condensed and collected in the water collector during the course of the experiment.

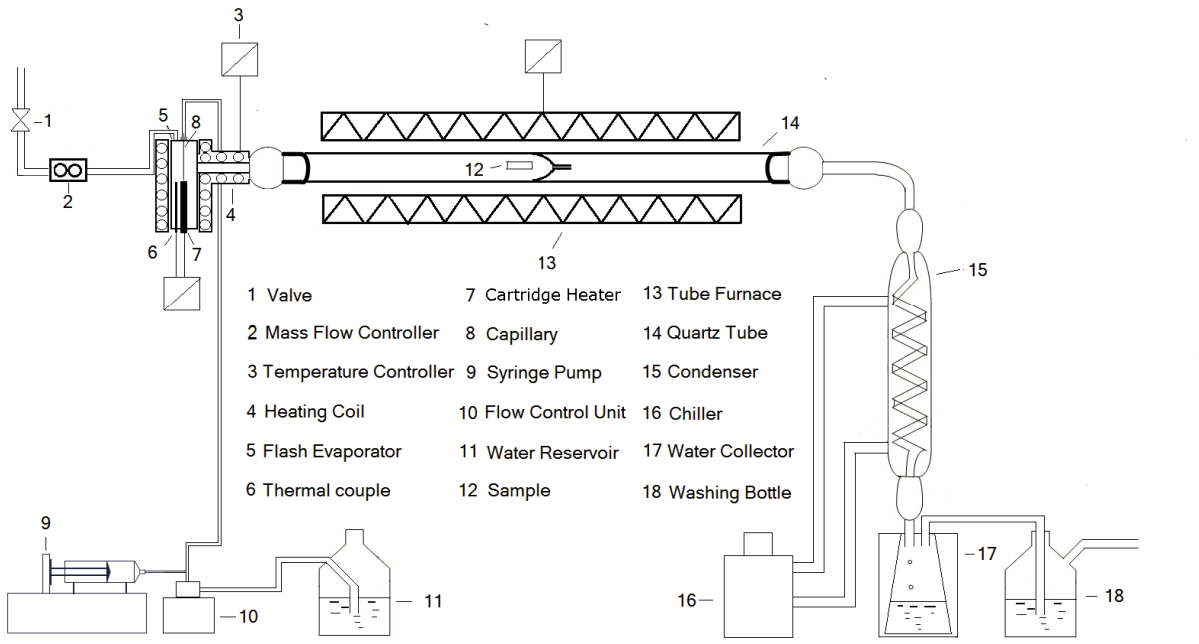

Fig. 3.1 Schematic of the experimental apparatus for the chromium evaporation estimation

3.2.2 Chromium collection and analysis

Our observations indicated that the chromium vapor condensed at lower temperature sections of the reactor wall, and the glass elbow joint as Cr_2O_3 (Cr^{3+}, green) and $CrO_2(OH)_2$ (Cr^{6+}, brown) and dissolved in the condensed water. After the completion of the evaporation experiment, deposited and dissolved chromium was collected for assay. This involved dissolution and collection of the condensed chromium species from the reactor wall as well as collection of the chromium containing water that condensed in the water collector. In terms of chromium extraction, it was observed that Cr^{6+} present as $CrO_2(OH)_2$ dissolved easily in water whereas

Cr^{3+} compound that condensed on the reactor wall dissolved in concentrated HNO_3. Efforts on mechanical removal and chemical dissolution of the Cr_2O_3 (Cr^{3+}) proved difficult and non-reproducible with large scatter in the Cr assay. A novel process to convert Cr^{3+} to Cr^{6+} was developed to facilitate the dissolution of all evaporated chromium. The condensed chromium was extracted using a two-step process: (a) dissolution in the concentrated nitric acid (upon heating to 80 ^{o}C), followed by (b) dissolution in an alkaline potassium permanganate (0.3% $KMnO_4$ in 1% NaOH medium, upon heating up to 80 ^{o}C). The second step converted the remaining Cr^{3+} species (which could not be dissolved earlier in the nitric acid solution) to Cr^{6+}. Inductively coupled plasma atomic emission spectroscopy, ICP-AES (Perkin Elmer Optima 7300, Norwalk, USA) was used to analyze the chromium concentration in the condensate. Standard quality assurance procedures were employed, including analysis of duplicate samples, method blanks, post digestion spiked samples, and laboratory control samples.

3.3 *Thermogravimetric analysis (TGA)*

TAG (Perkin Elmer Pyris 1, Norwalk, USA) tests were conducted under an oxidizing environment to study the oxidation behavior of the AFA alloy at 800-900 ^{o}C. Alloy test coupons (5x5x1mm) were ground with SiC paper up to 1200 grit and cleaned ultrasonically in deionized water followed by degreasing and washing with ethanol and acetone. Dry air at a flow rate of 50 standard cubic cm min^{-1} (sccm) was used during the entire test duration. The samples were heated up at a rate of 20 ^{o}C/min and maintained in the isothermal region for 20 h and cooled down at a rate of 20 ^{o}C/min.

3.4. Application of Manganese Cobalt Oxide Spinel Coating

Alloy test coupons (25x20x1mm) were ground with SiC and cleaned ultrasonically in deionized water followed by degreasing and washing with ethanol and acetone. A slurry containing the conductive manganese cobaltite ($Mn_{1.5}Co_{1.5}O_4$) spinel oxide, binder, dispersant and solvents were applied on the coupon surface as well as edges by aerosol spray deposition (ASD) and followed by forced air drying. Multiple deposition-dry cycles were applied to help to build up the required coating thickness. After coating, the part is subjected to two heat treatments to develop an adherent, dense coating. The first heat treatment consist of a controlled atmosphere, reduction firing which reduces the spinel to Co metal and MnO. During subsequent oxidation in air (or in-situ during stack start-up) the Co and MnO react with oxygen to reform the spinel with enhanced densification via reaction-sintering. Fig. 3.2 shows the key process operations in the coating process.

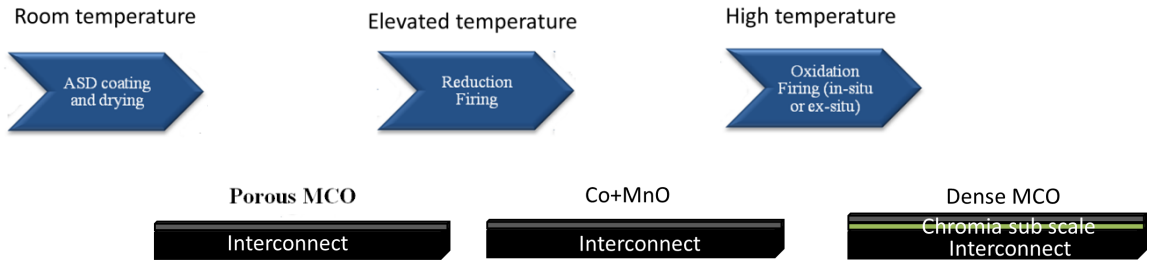

Fig. 3.2 Key Operations in the standard ASD based coating process flow

3.5. Sample Characterization

Surface morphology and scale composition were analysed using environmental scanning electron microscopy (ESEM, FEI Quanta FEG 250, USA) coupled with energy dispersive X-Ray spectroscopy (EDS, Genesis Apex 4, EDAX, USA). The oxide scales were also analyzed by X-Ray Diffraction (XRD, D8 Advance, Bruker AXS GmbH, Karlsruhe, Germany). Oxide scale microstructures were further examined by focused ion beam (FIB) technique (FEI strata 400S, USA; 30 keV Ga+ ions) with a dual-beam column and Transmission electron microscopy couple with Scanning Transmission electron microscopy (TEM/STEM, FEI Sprit Twin TEM). Thin oxide scales developed in the very early stages of oxidation were characterized by Auger electron spectroscopy (AES, PHI 595 Multiprobe System).

CHAPTER 4

RESULTS AND DISCUSSION

4.1. Equilibrium chromium vapor pressure

4.1.1 Equilibrium chromium vapor pressure calculation

Using a thermo-chemical data base (HSC Chemistry 6.12, Outotec Oyj, Finland), equilibrium vapor pressures of various chromium vapor species formed from pure chromium oxide under flowing humid air was calculated. Fig. 4.1 shows vapor pressure of the chromium-containing volatile species as a function of temperature and water vapor pressure. The Fig. 4.1 a shows that at 1% water vapor the overall chromium vapor pressure is dominated by the vapor pressure of $CrO_2(OH)_2(g)$ below 1000°C, above which vapor pressure of $CrO_3(g)$ and $CrO_2(OH)(g)$ becomes equally significant and starts to take over as the dominating species. This transition temperature will increase as the amount water vapor increases (Fig. 4.1 a-e).

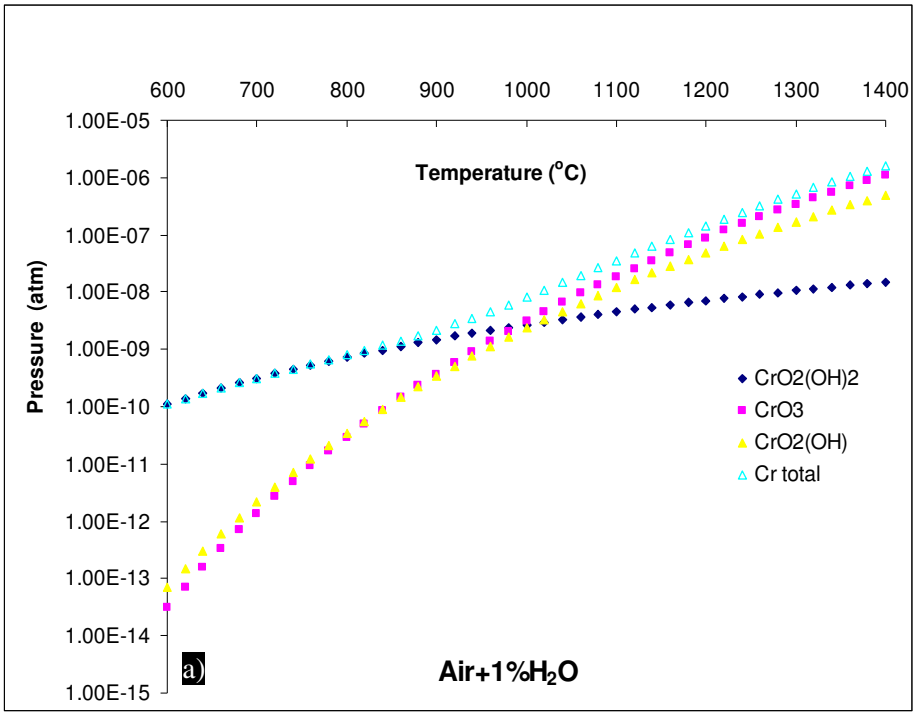

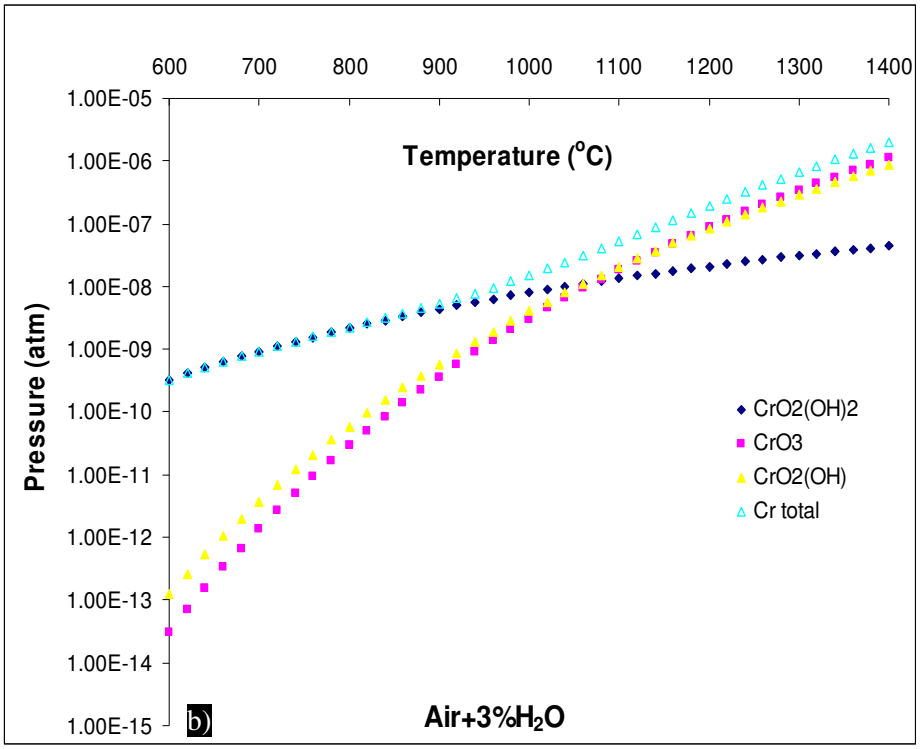
600
700
800
900
1000
1100
1200
1300
1400
1.00E-05
1.00E-06
1.00E-07
1.00E-08
1.00E-09
1.00E-10
1.00E-11
1.00E-12
1.00E-13
1.00E-14
1.00E-15
Temperature (°C)
Pressure (atm)
CrO2(OH)2
CrO3
CrO2(OH)
Cr total
b)
Air+3%H2O

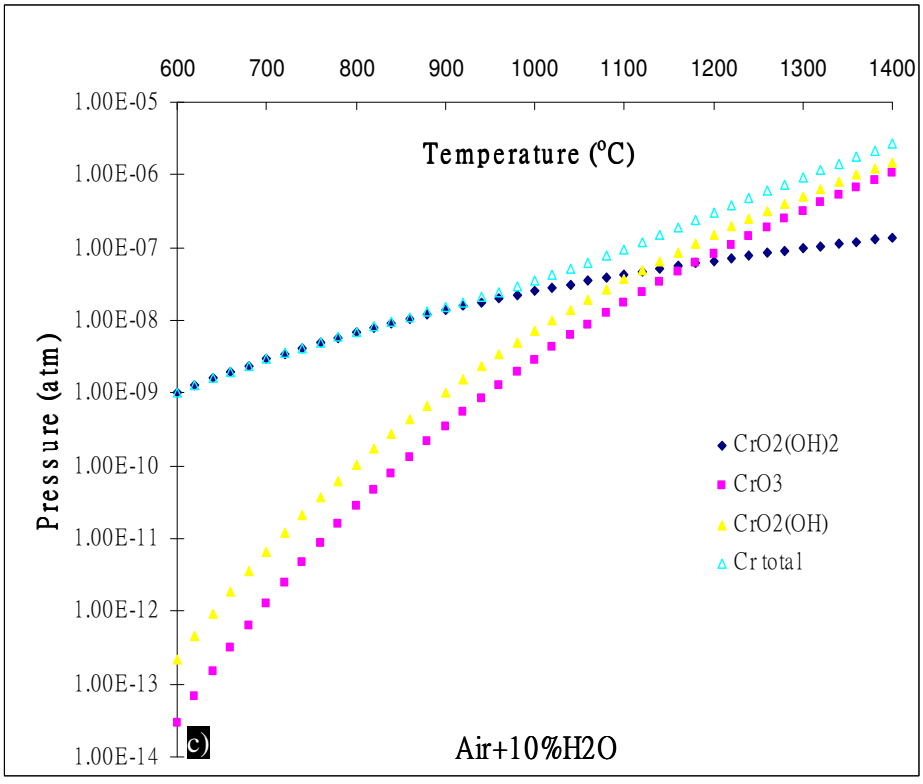
600
700
800
900
1000
1100
1200
1300
1400
1.00E-05
1.00E-06
1.00E-07
1.00E-08
1.00E-09
1.00E-10
1.00E-11
1.00E-12
1.00E-13
1.00E-14
Temperature (°C)
Pressure (atm)
CrO2(OH)2
CrO3
CrO2(OH)
Cr total
c)
Air+10%H2O

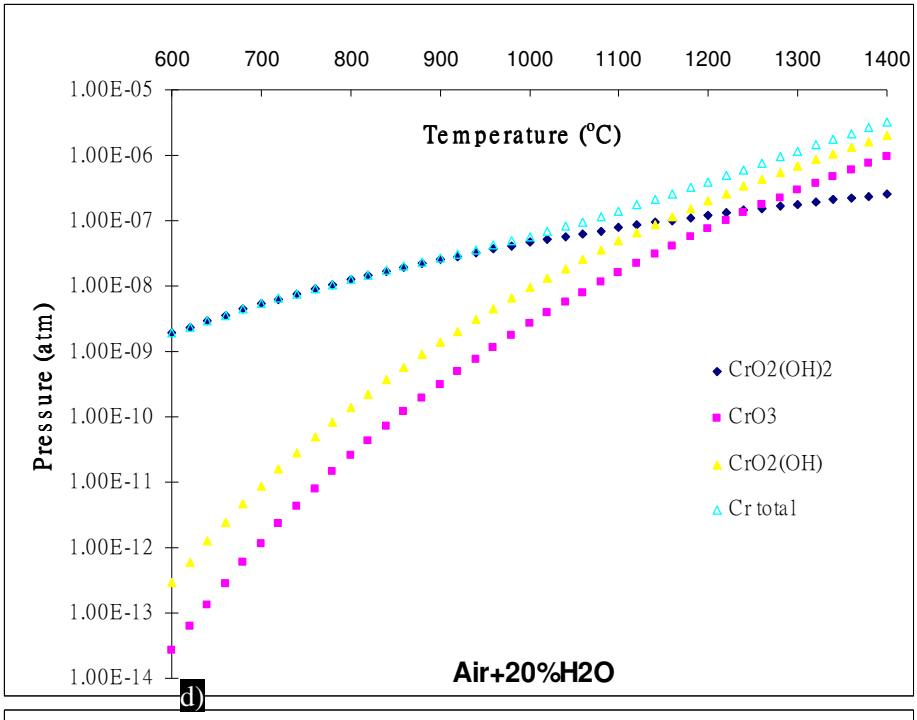
600
700
800
900
1000
1100
1200
1300
1400
1.00E-05
1.00E-06
1.00E-07
1.00E-08
1.00E-09
1.00E-10
1.00E-11
1.00E-12
1.00E-13
1.00E-14
Temperature (°C)
Pressure (atm)
CrO2(OH)2
CrO3
CrO2(OH)
Cr total
Air+20%H2O

d)

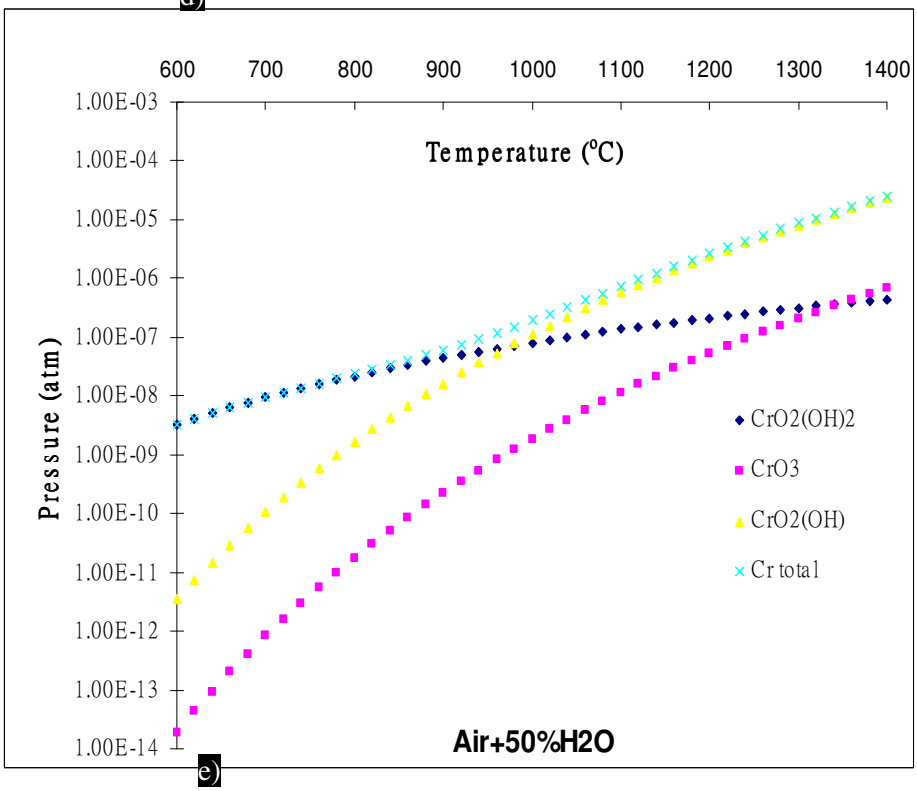
600
700
800
900
1000
1100
1200
1300
1400
1.00E-03
1.00E-04
1.00E-05
1.00E-06
1.00E-07
1.00E-08
1.00E-09
1.00E-10
1.00E-11
1.00E-12
1.00E-13
1.00E-14
Temperature (°C)
Pressure (atm)
CrO2(OH)2
CrO3
CrO2(OH)
Cr total
Air+50%H2O

e)

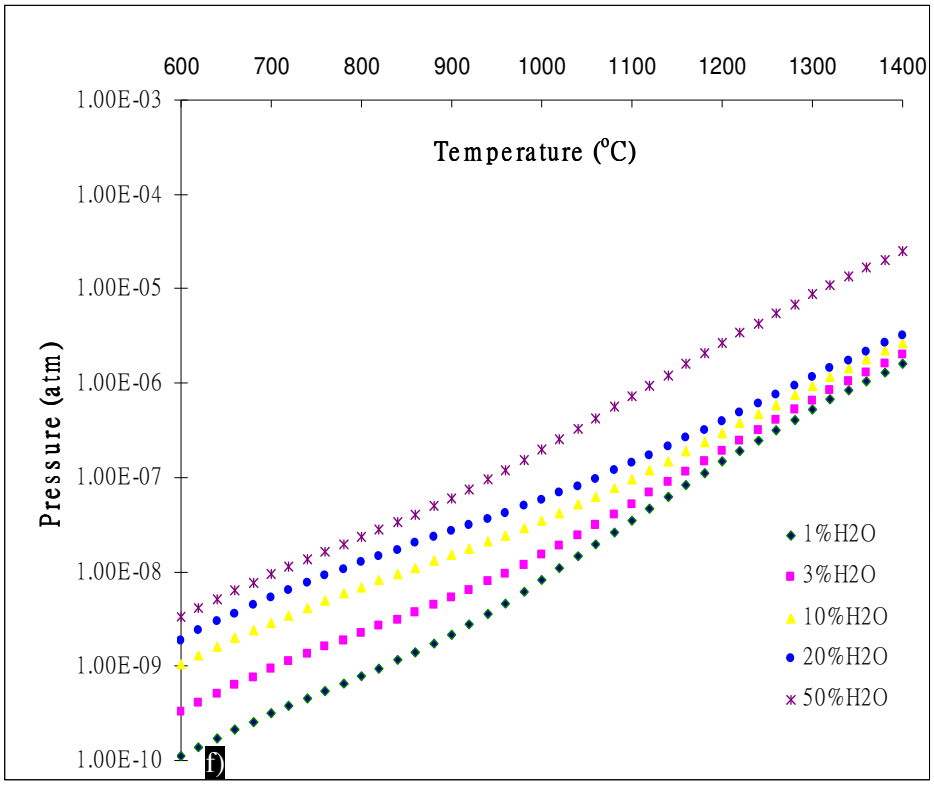

Fig. 4.1 Calculated chromium-vapor species pressure in (a) 1%H_2O+Air (b) 3%H_2O+Air (c) 10%H_2O+Air (d) 20%H_2O+Air (e) 50%H_2O+Air (f) Total vapor pressure of volatile chromium vapor species ($PCrO_2(OH)_2$ (g) + $PCrO_2(OH)$ (g) + $PCrO_3$(g)) as function of temperature for different water vapor contents

The partial pressure of $CrO_2(OH)$(g), $CrO_2(OH)_2$(g), will increase with humidity level (Fig. 4.1 a-e), as a result, as it was shown in Fig. 4.1 f, the total pressure of chromium-containing volatile species increases with humidity level. In addition, other thermal databases have been searched, and the equilibrium pressures of CrO_3(g) $CrO_2(OH)$(g) and $CrO_2(OH)_2$(g) have been calculated using various thermal databases and values obtained by experiments and first principle calculations. Figure 3.2 shows a comparison of CrO_3(g), $CrO_2(OH)_2$(g) and $CrO_2(OH)$(g) vapor pressure at 3% humidity level (most common water vapor content representing the SOFC working condition) [79-83]. There are limited number of experimental values of CrO_3(g) vapor pressure available in the literature. Kim did most of the measurement of CrO_3(g) using transpiration method above 1400 °C, while Opila did only one

measurement at 900 °C. Nevertheless, Opila's measurement agreed with the exploration of Kim's data [79]. The CrO_3 vapor pressure (Fig. 4.2 a) calculated using HSC database is very close to the that using JANAF database, however they are both about one order of magnitude lower than the value calculated using Kim's experimental results. Results obtained from Ebbinghaus's calculation and IVANTATHERMO database are in good agreement with Kim's experimental results. JANAF data and HSC data are primarily based on mass spectrometric study (vapor effusing from an alumina Knudsen cell which contained Cr_2O_3 under oxidizing environments) of Grimley et al [93]. Kim ascribed the possible reason to the uncertainties in their estimated relative ionization cross-section of the vaporized species. Therefore, IVANTATHERMO database and Ebbinghaus's calculation are more recommended for CrO_3 (g) vapor pressure calculations.

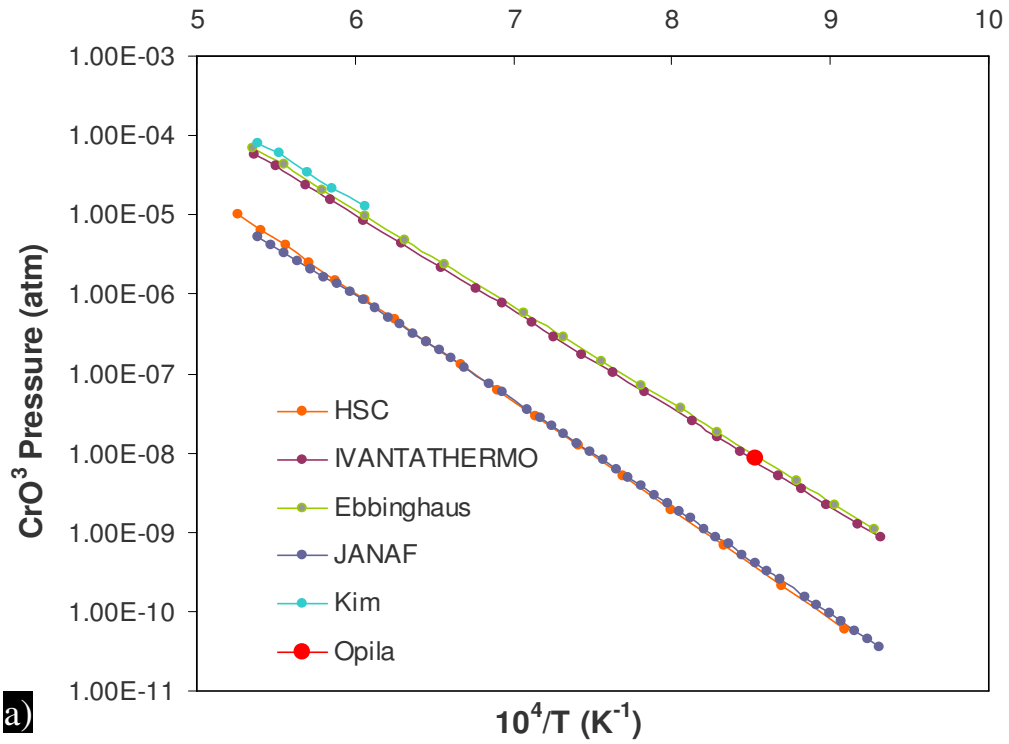

a)

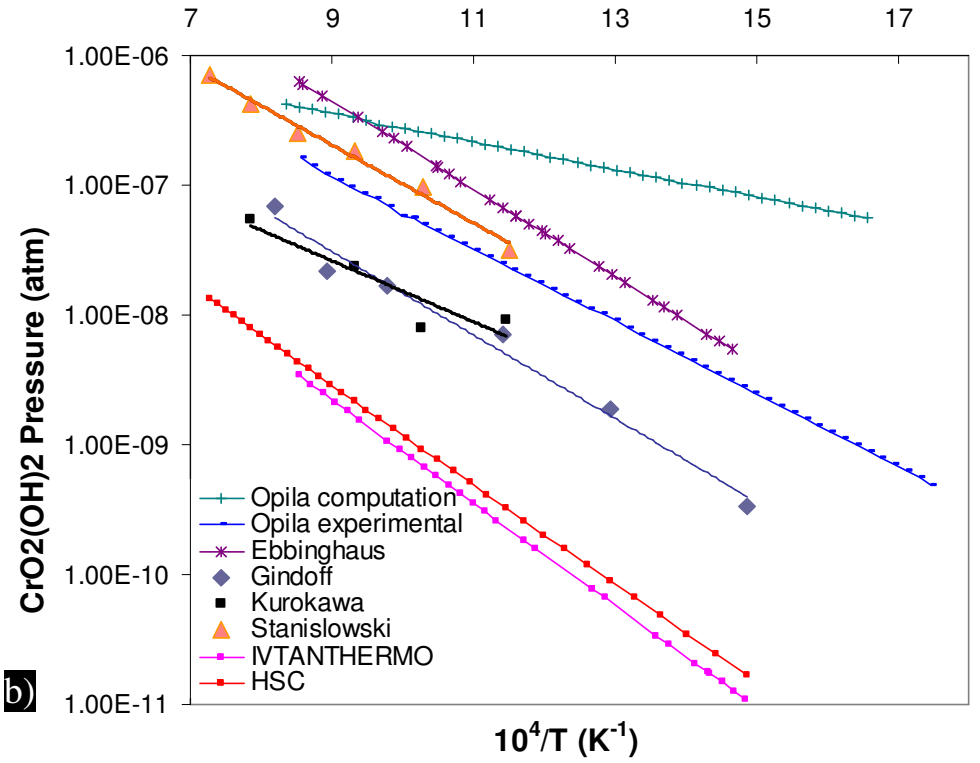

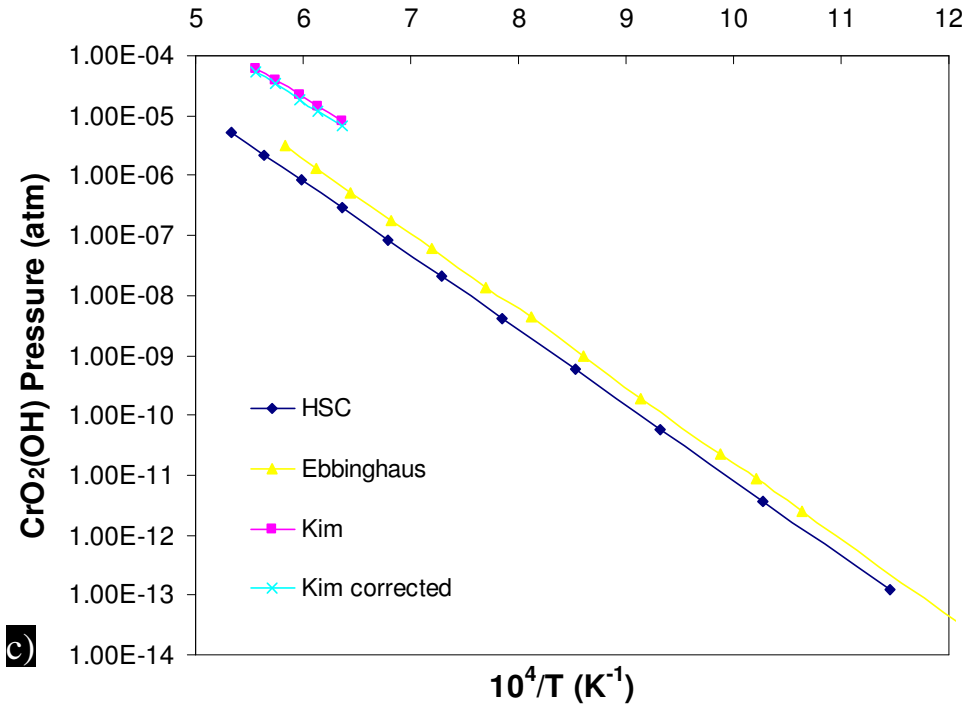

Fig. 4.2 Calculated Cr-O-H species pressure in 3%H_2O+Air from different literature data and thermodynamic database (a) CrO_3 (b) $CrO_2(OH)_2$ (c) $CrO_2(OH)$

The $CrO_2(OH)_2$ (Fig. 4.2 b) vapor pressures calculated using HSC database and IVANTATHERMO database are about one or two orders of magnitude lower than most of the experimental data. Therefore, they are not recommended for $CrO_2(OH)_2$ (g) vapor pressure calculations. The $CrO_2(OH)_2$ (Fig. 4.2 b) vapor pressures calculated using Oplia's computational results and Ebbinghaus's calculation are much higher than most of the experimental data, it is postulated by Opila that the higher computation value may be due to the fact that the harmonic approximation is likely to break down for low frequency modes. Nevertheless, there is still large discrepancy between the experimental values although similar transpiration methods were employed. The possible reason of the discrepancy may come from the chromium collection methods, as some of the Cr^{6+} species will be reduced to Cr^{3+} which is insoluble in acid solution, further conversion of Cr^{3+} to Cr^{6+} is needed. Therefore, Opila and Stanislowski's data are recommended.

Figure 4.2 c shows a comparison of and $CrO_2(OH)$(g) vapor pressure at 3% humidity level. It is shown that the $CrO_2(OH)$ vapor pressures calculated using HSC database and Ebbinghaus's calculation are about one order of magnitude lower than most of Kim's experimental results and that corrected using Opila's $CrO_2(OH)_2$(g) data. Since higher $CrO_2(OH)_2$(g) values are adopted in Ebbinghaus's calculation, therefore, Ebbinghaus's calculation for $CrO_2(OH)$ should be lower than its real value. Hence, Kim's data are preferred over the estimates of Ebbinghaus's calculation. From the analysis of all the existing data in literature, Fig. 4.3 is constructed, where CrO_3 vapor pressure calculated by Ebbinghaus and $CrO_2(OH)$ vapor pressure determined by Kim is chosen as the most reliable reference; and $CrO_2(OH)_2$ vapor pressure determined by Opila and other groups are also chosen. It should be noted that some experimental data are extrapolated in order to fit the wide range of temperature scale.

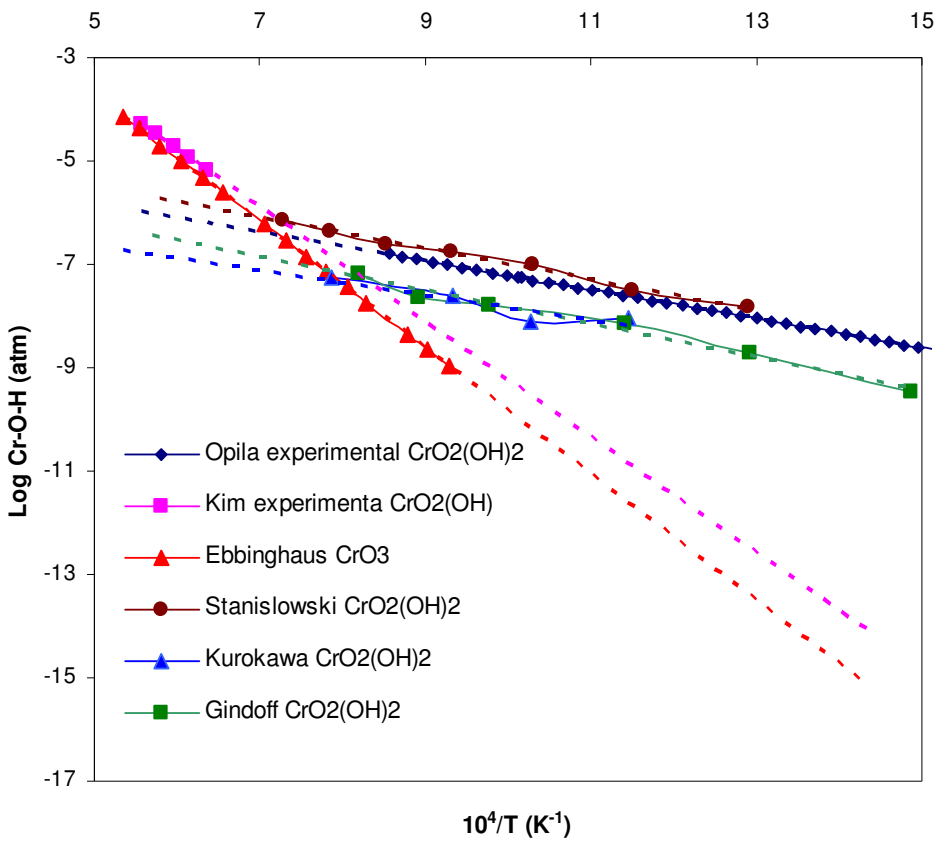

Fig. 4.3 Calculated Cr-O-H species pressure in 3%H_2O+Air from different literature data and thermodynamic database

4.1.2 Chromium vapor measurement via transpiration method

The standard calibration of test set-up was done by measuring the chromium loss rate (500 h) of pure chromium oxide (99.99% pure, Sigma Aldrich). The chromium loss rate versus volumetric flow rate is plotted in Fig. 4.4. The equilibrium (vapor pressure saturated) and non-equilibrium (vapor pressure unsaturated) region were determined experimentally by varying the flow rate of the carrier gas (Fig. 4.4). A flow rate of 100sccm was chosen to measure the equilibrium chromium vapor pressure. The chromium vapor pressure measured at 850 ^{o}C & 950 ^{o}C were compared with the most reliable literature data (Fig. 4.5). The total equilibrium chromium vapor pressure falls in between the Opila and Gindoff's data after

corrected (the IVANTATHERMO database is used to calculate CrO_3 (g) vapor pressure and Kim's extrapolated data is used to calculate $CrO_2(OH)$ (g) vapor pressure)

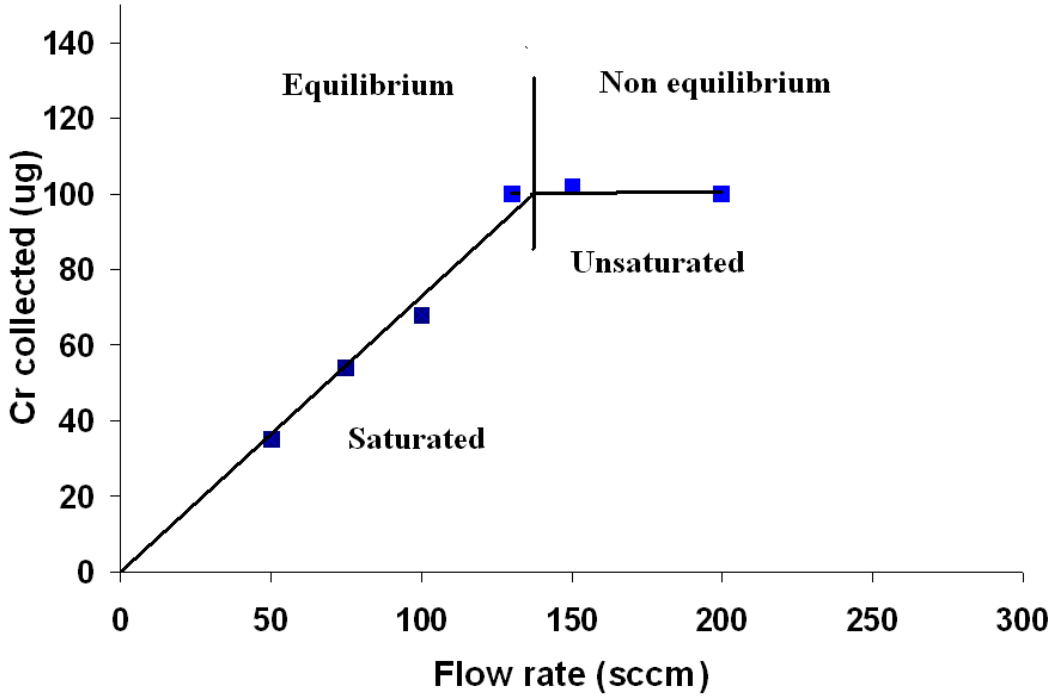

Fig. 4.4 Gas flow-rate dependence of chromium transport rate at 850 ^{o}C in 3% humid air

Although, the purpose of this work is not to study the chromium equilibrium vapor pressure from pure Cr_2O_3, nevertheless, this gave us the confidence of our own measurement technique. It is important to note the effect of the temperature on chromium vapor pressure is significant as reported repeatedly before. However, for Cr evaporation rate measurements of different bare alloys as well as coatings, a higher flow rate (300sccm) is chosen to ensure the chromium loss rate is independent of the volumetric flow rate (as shown in Fig. 3.4). In this flow rate region, the evaporation rate is independent of the flow rate of the carrier gas; hence maximum chromium evaporation rate is achieved.

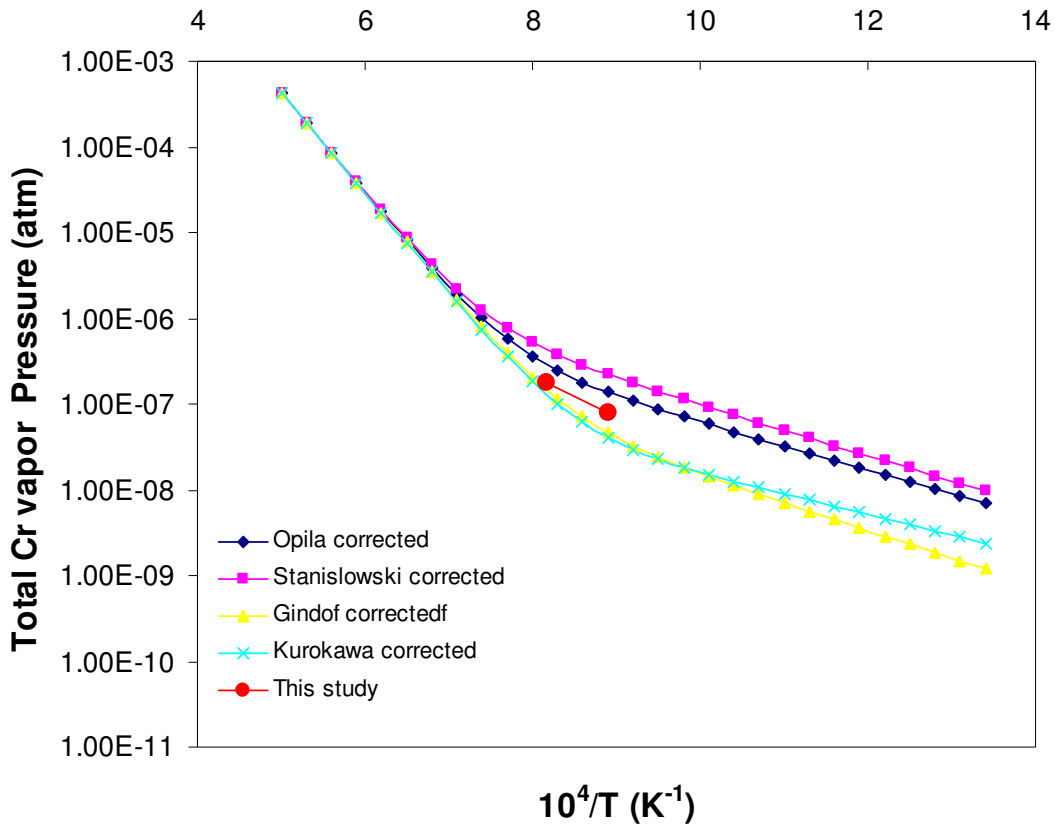

Fig. 4.5 Measured Cr-O-H species pressure in 3%H_2O+Air in comparison with different literature data and thermodynamic database

The chromium evaporation rates of different bare alloys measured (500 h) from 850 to 950 ^{o}C in 3% or 12% humid air were shown in Fig. 4.6. The evaporation rate decreased in the order: austenitic & ferritic chromia former> nickel base chromia and alumina mixed former> austenitic alumina former > ferritic alumina former.The increase of the temperature and water vapor content affects the chromium evaporation rates as predicted by the calculation.

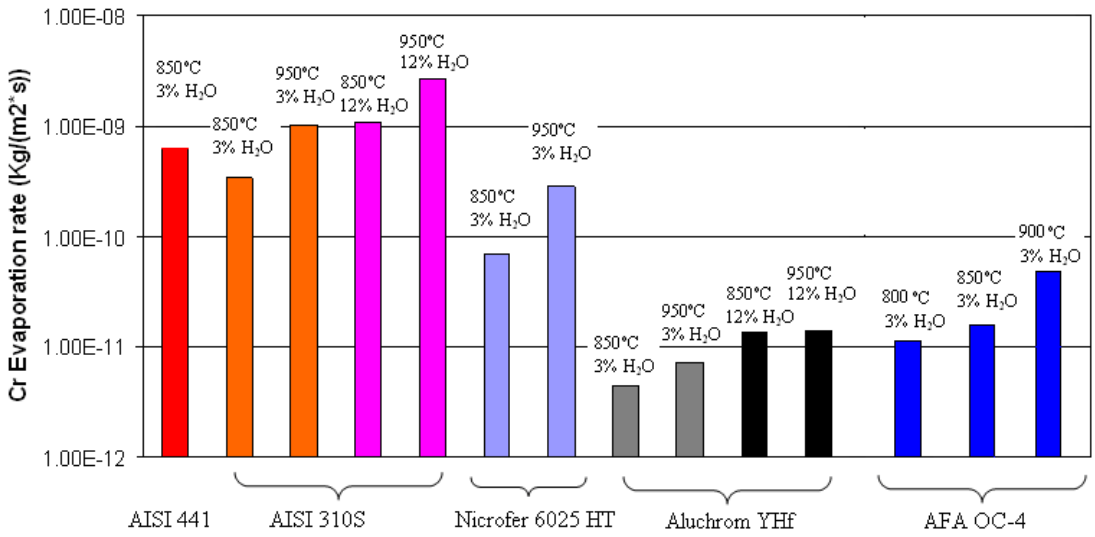

Fig. 4.6 Measured Cr evaporation rates of different bare alloys

4.2 Ni and Fe Based Alloys Chromia forming Alloys

4.2.1 Oxide scale formation and characterization of AISI-310S

Oxide scale after 500 h exposure at 850 ^{o}C and 3% humidity appeared non-uniform in morphology, i.e., generally dark scale with bright patches (Fig. 4.7 a). At higher magnifications, the areas with distinctly different morphologies were observed (Fig. 4.7 b), each having a considerably different elemental composition (as described in EDS profiles in Fig. 4.7 e&f). The areas with faceted fine grains (Fig. 4.7 d) were characterized to be the oxide of chromium and manganese. Within such areas, there were localized patches of overgrown faceted crystals (Figure 4.7 c), but these patches showed little compositional variation to the surrounding fine grain area. The areas with no faceted grains (as a result of spallation, as apparent in Fig. 4.7 b) was detected to be predominantly chromia (refer EDXS profile Fig. 4.7 f). Both morphology and composition of the oxide scales developed at 950 ^{o}C in 3% humidity air (Figure 4.8) were largely similar to those developed at 850 ^{o}C in 3% humidity air. The significant differences were the presence of coarser oxide grains (Figures 4.8 c and 4.8 d), and a larger areas with features of spallation (Fig. 4.8 b) at 950 ^{o}C. With the exposed chromia sub-layer and bare metal, together with the temperature effect, higher chromium evaporation rate is expected and observed (Fig. 4.6). Morphological variations of the scale formed at 850 ^{o}C in 12% water vapor pressure were also similar to those in Fig. 4.7 and 4.8. The major fraction of the surface was covered with the faceted fine grains (Fig. 4.9 c&d). However, there were a few variations which may be quite relevant for the chromium evaporation behavior of the alloy: (i) the much greater fraction of the surface had the features of spallation (Fig. 4.9 a&b), and (ii) cracks were observed in the areas with the faceted fine grains of chromium-manganese oxide (Fig. 4.9 d),

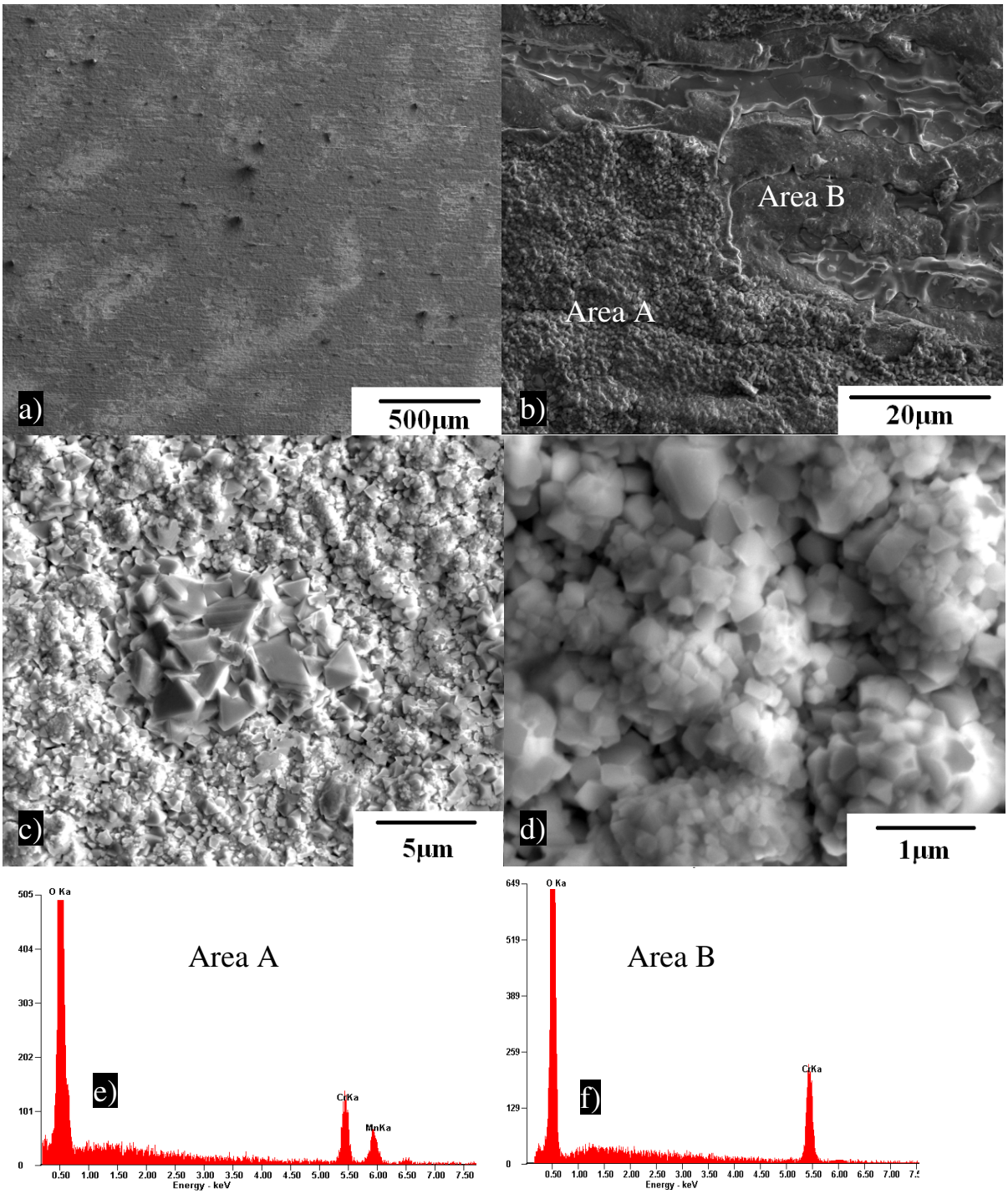

Fig. 4.7 Different oxide scale morphologies of AISI 310S exposed to 3% humid air for 500 h at 850°C (a), (b), (c), (d), and (e) area A, (f) area B is EDS elemental profile of the selected area of interests

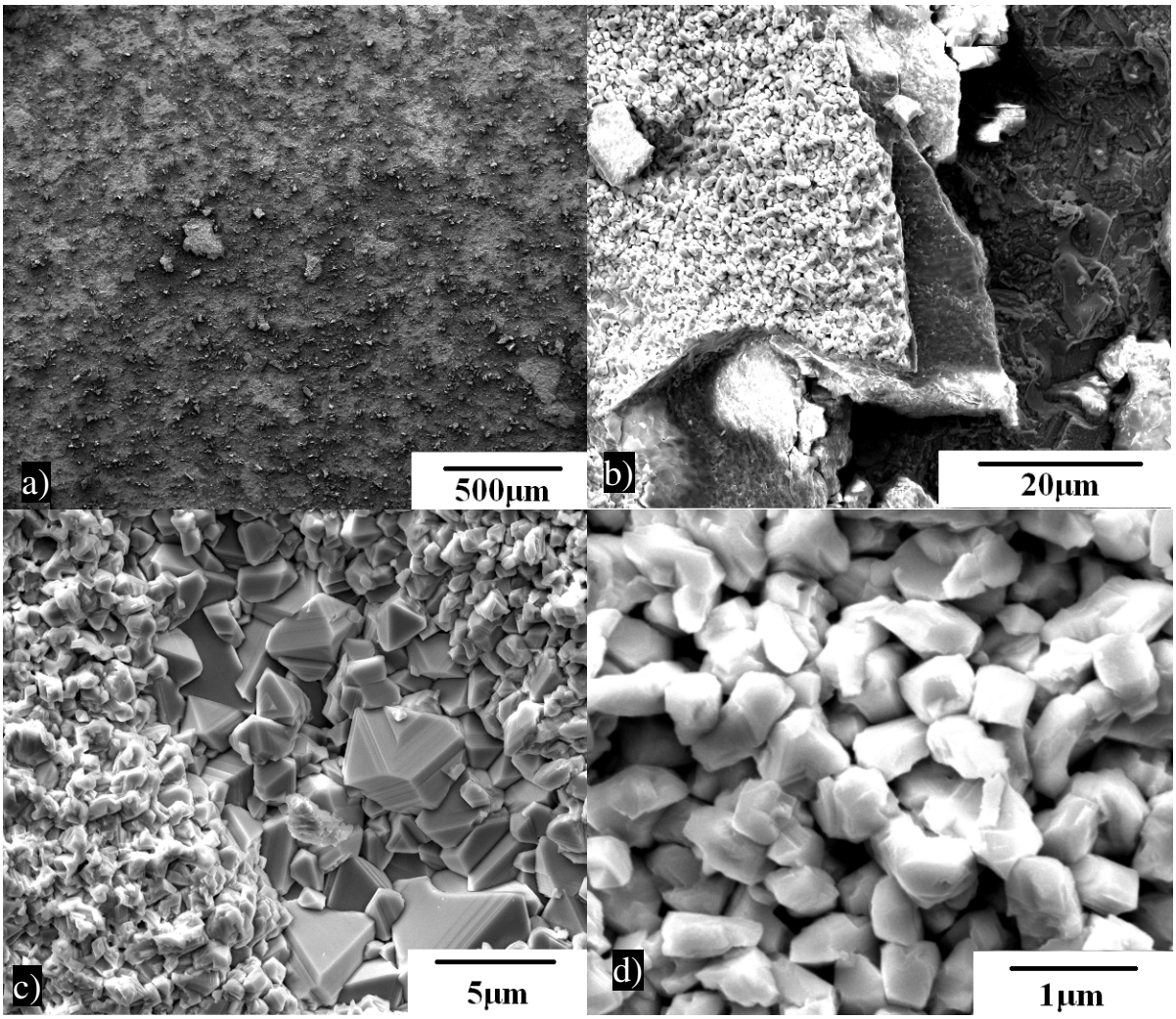

Fig. 4.8 Different oxide scale morphologies of AISI 310S exposed to 3% humid air for 500 h at 950°C (a), (b), (c), (d)

which led to the spallation of the outer scale, exposing the underneath chromia layer (seen in Fig. 4.9 a&b). To confirm the physical and chemical characteristics across the depth of the oxide scales, cross-section of an AISI 310S alloy sample exposed to a 3% humidity air for 500 h at 850 °C was examined by FIB/SEM/EDS.

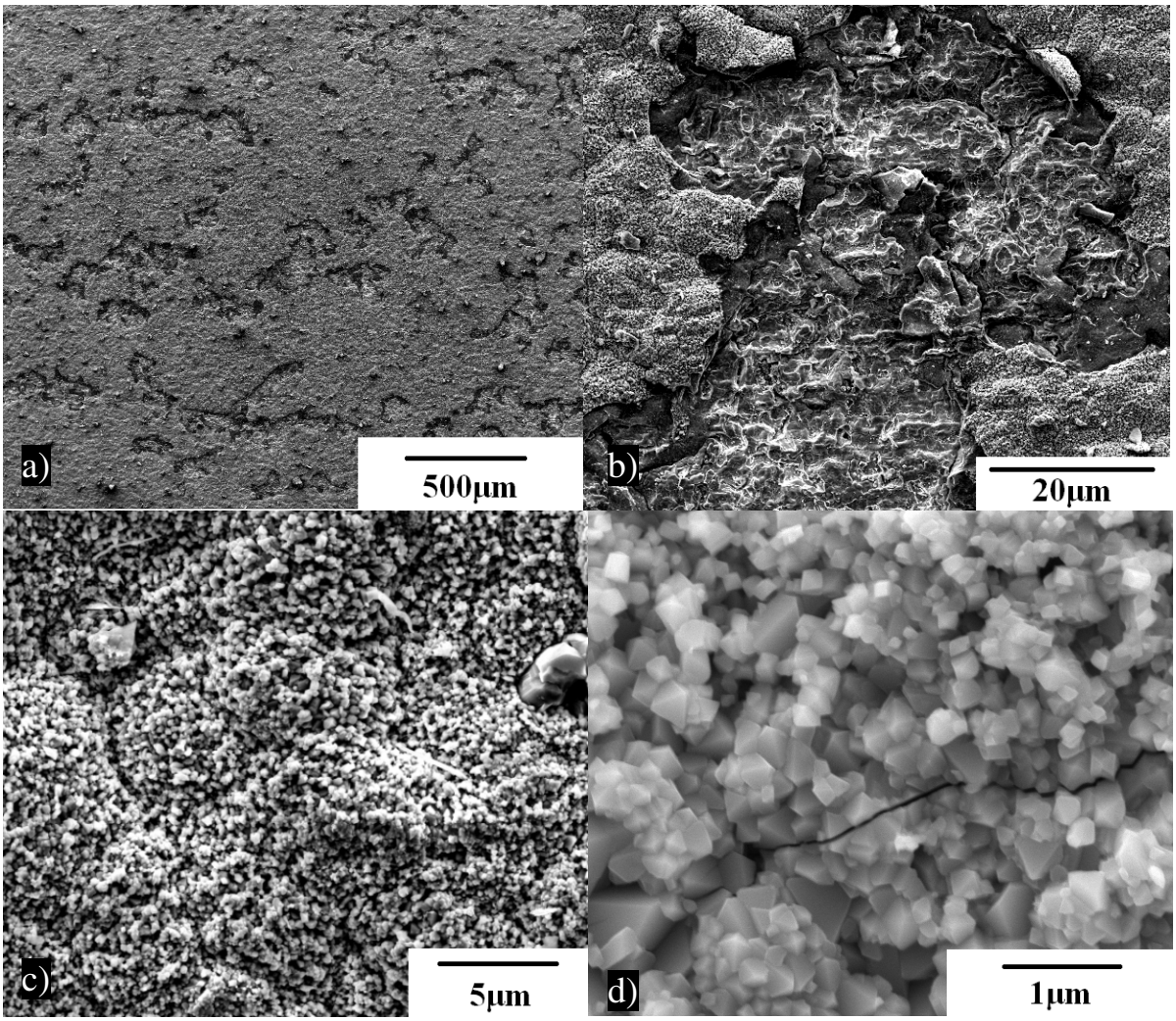

Fig. 4.9 Different oxide scale morphologies of AISI 310S exposed to 12% humid air for 500 h at 850°C (a), (b), (c), (d)

Fig. 4.10 establishes: (i) the outer layer of overgrown oxide (~ 2 µm thick), and (b) the inner layer of chromium oxide (Cr_2O_3) underneath the external layer of chromium-manganese mixed oxide ($(Cr,Mn)_3O_4$),which is consistent with the EDS results described in Fig. 4.7. The highest chromium evaporation rate of AISI 310S among the three test alloys is attributed to the formation of a chromium-rich scale, scale cracking and spallation. The presence of the 2% manganese in AISI 310S accounts for the formation of the outer layer of $(Cr,Mn)_3O_4$ spinel, whereas the inner scale remains composed primarily of chromia (Cr_2O_3). The presence of the protective $(Cr,Mn)_3O_4$ spinel can lower the chromium

evaporation by an order of magnitude when compared to pure chromia [12, 94]. However, in the case of the AISI 310S the $(Cr,Mn)_3O_4$ spinel either did not cover the total surface area or it suffered spallation (Fig. 4.7-4.9), exposing the underlying layer of pure chromia to humid air. This explains the higher chromium evaporation rate observed for AISI 310S.

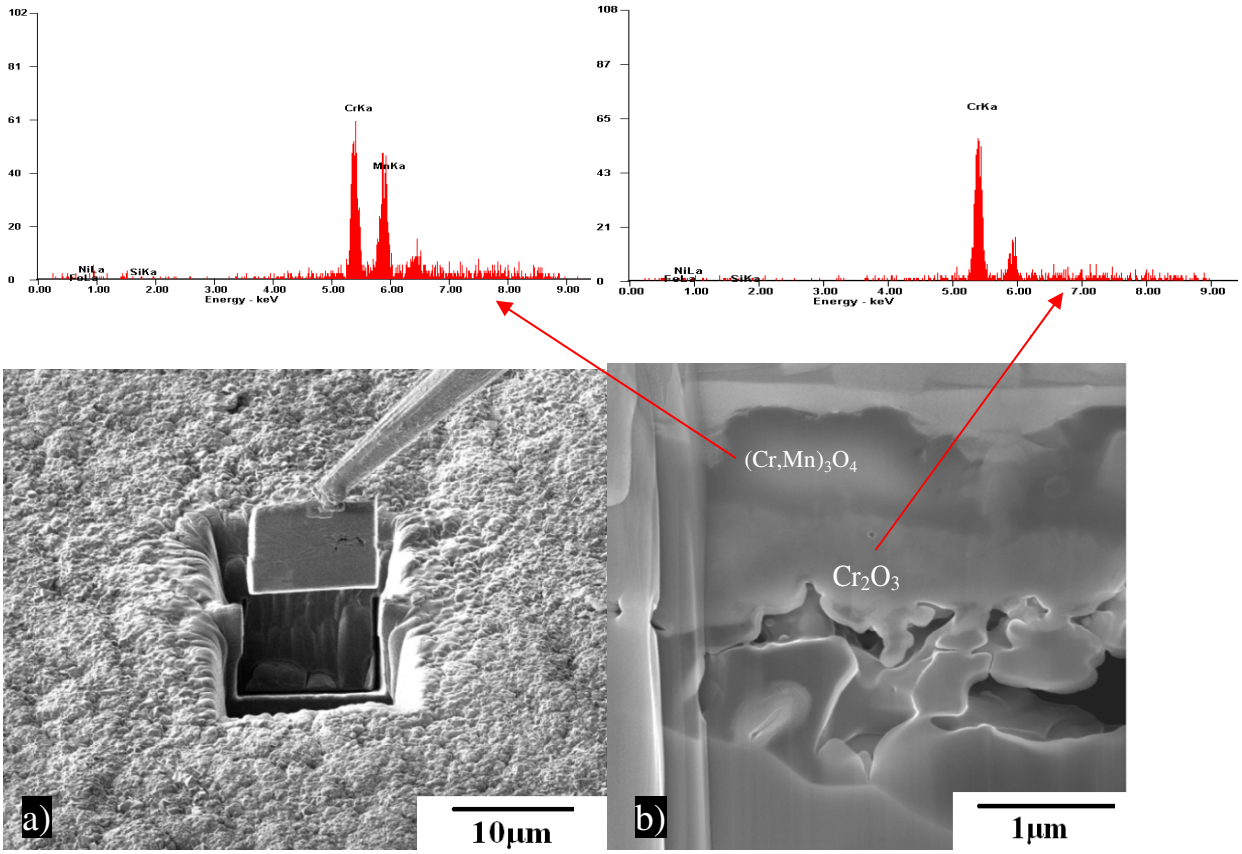

Fig. 4.10 FIB sectioning and SEM images of cross-section of AISI 310S exposed to 3% humid air for 500 h at 850°C, and EDS analysis of the different oxide scale layers

4.2.2 Oxide scale formation and characterization of Nicrofer6025 HT

The surface oxide that developed on Nicrofer6025 HT in 500 h oxidation at 850 and 950°C in 3% humidity air has regions of localized overgrowth (Fig. 4.11), which is more prominent at 950 °C (Fig.

4.11 d&e). The EDS results suggest the overgrowth region is a mix of oxides of chromium, nickel, silicon and iron, whereas the rest of the exposed area is predominantly aluminum oxide.

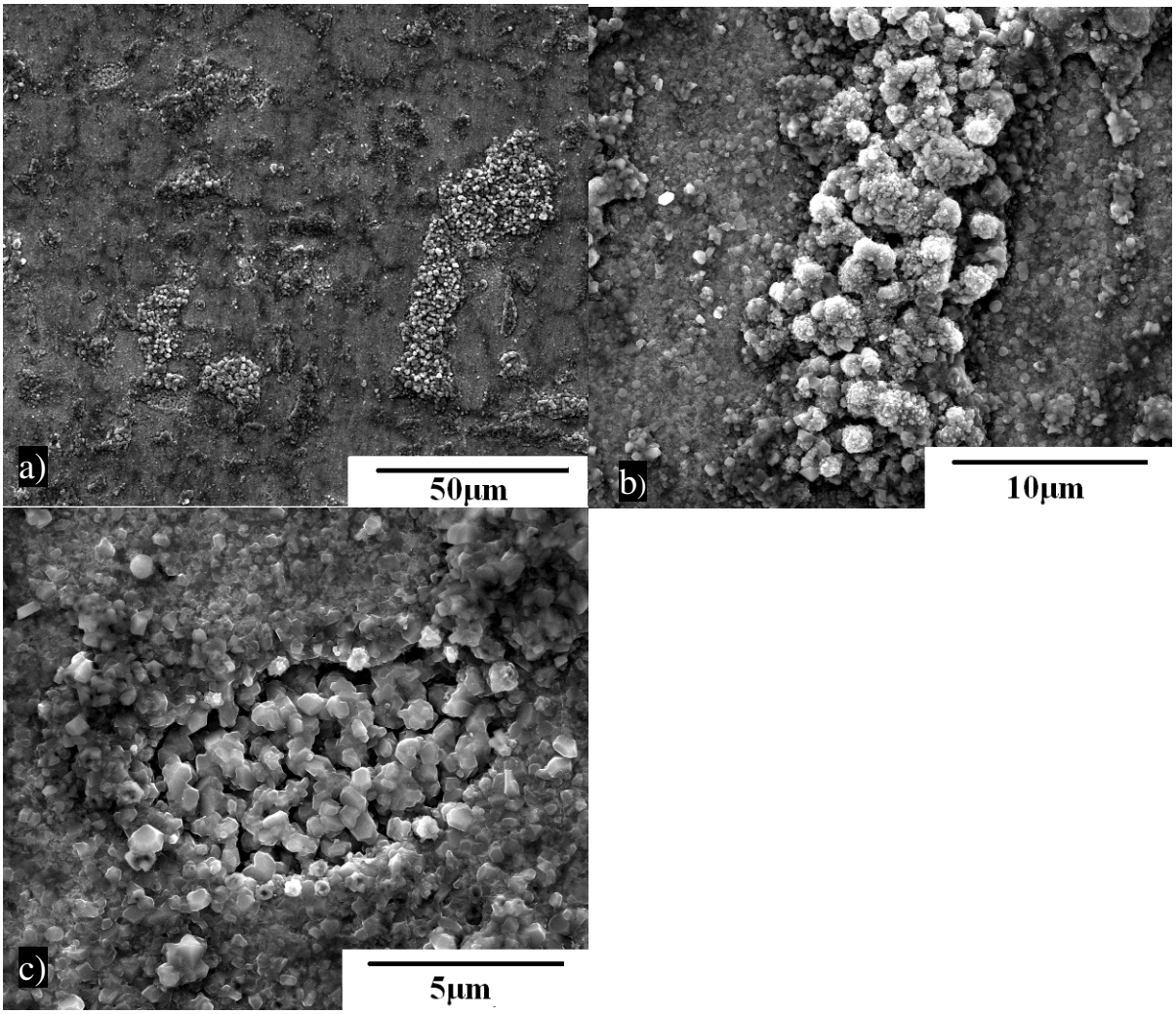

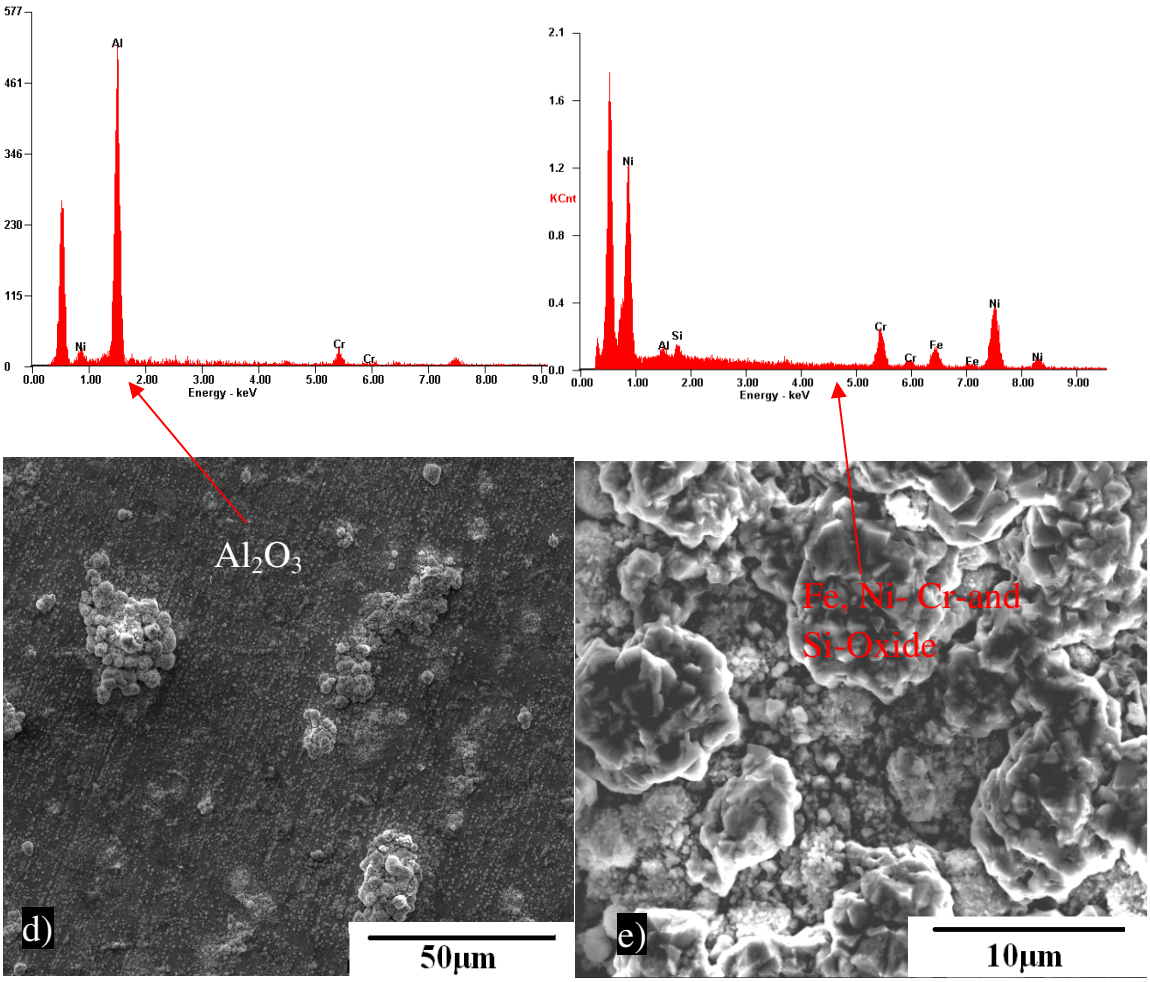

Fig. 4.11 Different oxide scale morphologies of Nicrofer 6025HT exposed to 3% humid air for 500 h: (a-c) at 850 °C, and (d-e) at 950 °C and EDS spectra suggesting formation of different oxides

The FIB cross sectional images and the EDS analysis of the overgrown scale are shown in Fig. 4.12 a and b. The oxide thickness in the overgrowth region is ~ 10 µm, (Fig. 4.12 a), whereas the thickness of the thinner region is only ~ 500 nm (Fig. 4.12 c). The inner layer of reasonably uniform thickness was identified to be essentially an aluminum oxide (Fig. 4.12 c). As the image contrast and EDS analysis would suggest the overgrowth region consisted of irregularly intermixed areas of a chromium oxide and mixed oxides of chromium, nickel, silicon and iron (Fig. 4.12 b). The layers of aluminum-rich and chromium-rich oxides (Fig. 4.12 c&b) are respectively Al_2O_3 and Cr_2O_3 (which was confirmed by XRD),

and which also is consistent with the reported nature of the oxide scales developed on a similar steel in steam [10, 11]. The reported literature also suggests that the steam environment can cause breakdown of the alumina scale [95], which explains the development of the overgrowth region. The frequent presence of the overgrown areas of chromium rich oxide (Fig. 4.11 & 4.12) accounts for the considerable chromium evaporation of Nicrofer6025 HT alloy (Fig. 4.6). The chromium evaporation rate of Nicrofer6025 HT is considerably lower than AISI 310S steel, which is attributed to the layer of the protective of alumina on Nicrofer6025 HT (Fig. 4.11 & 4.12).

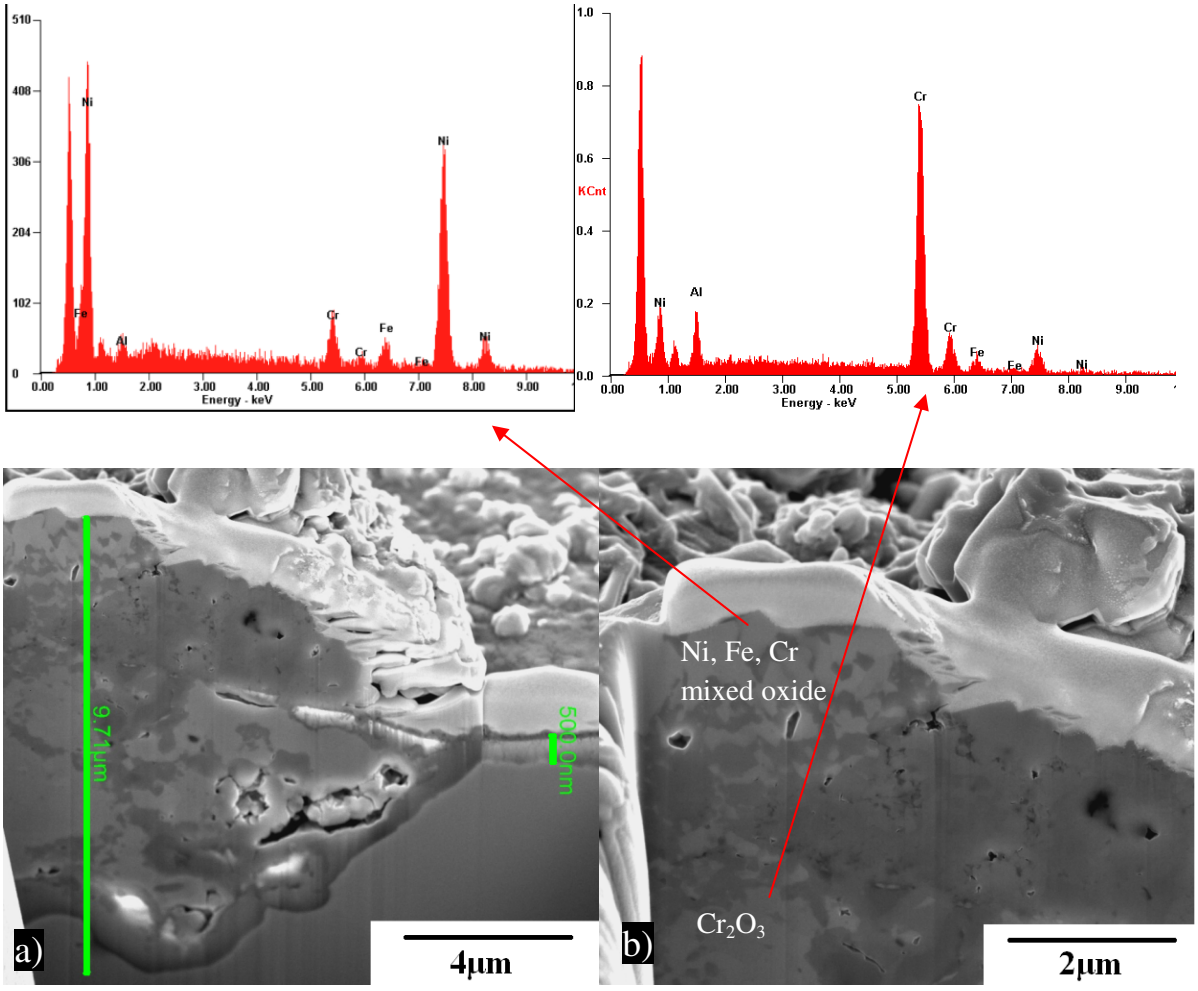

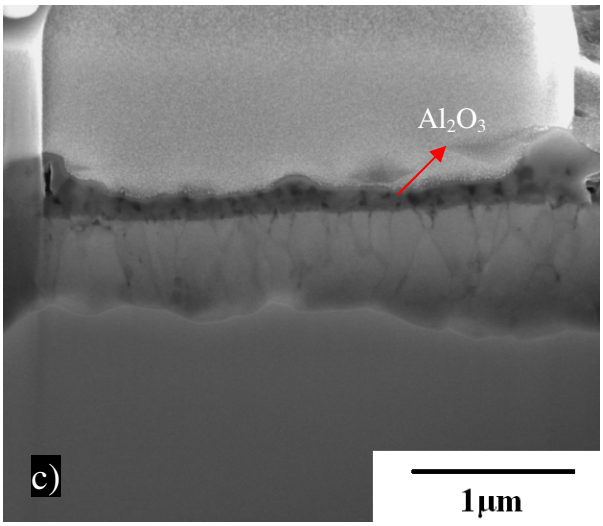

Fig. 4.12 FIB sectioning and SEM images of cross-section of Nicrofer 6025HT exposed to 3% humid air for 500 h at 950°C, and EDS analysis of the different oxide scale layers

4.2.3 Oxide scale formation and characterization of Aluchrom YHf

The oxide scales developed upon 500 h exposure of Aluchrom YHf in 3% humidity air at 850 °C was dense and uniform (Fig. 4.13 a&b).

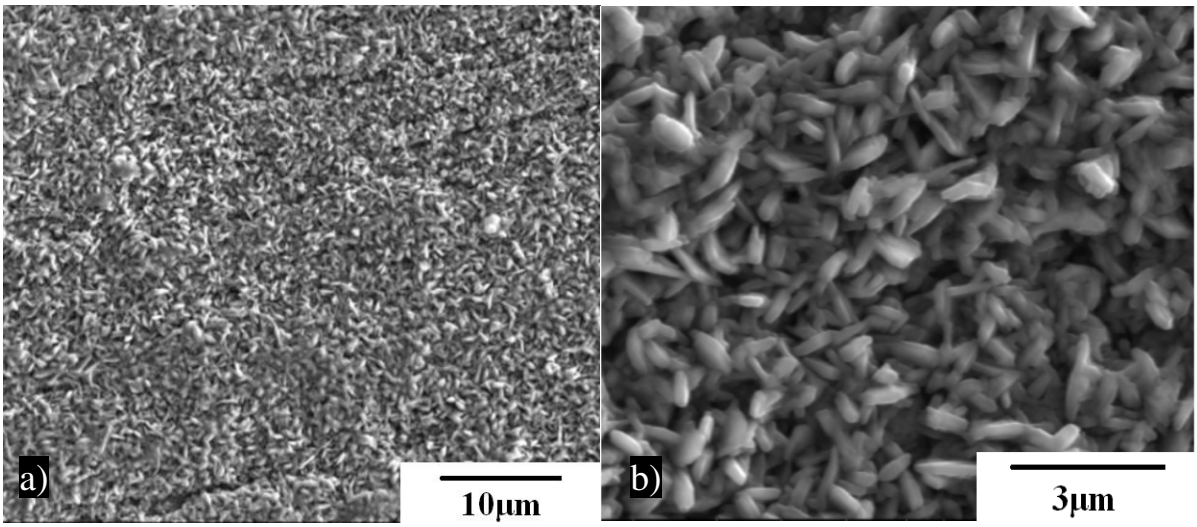

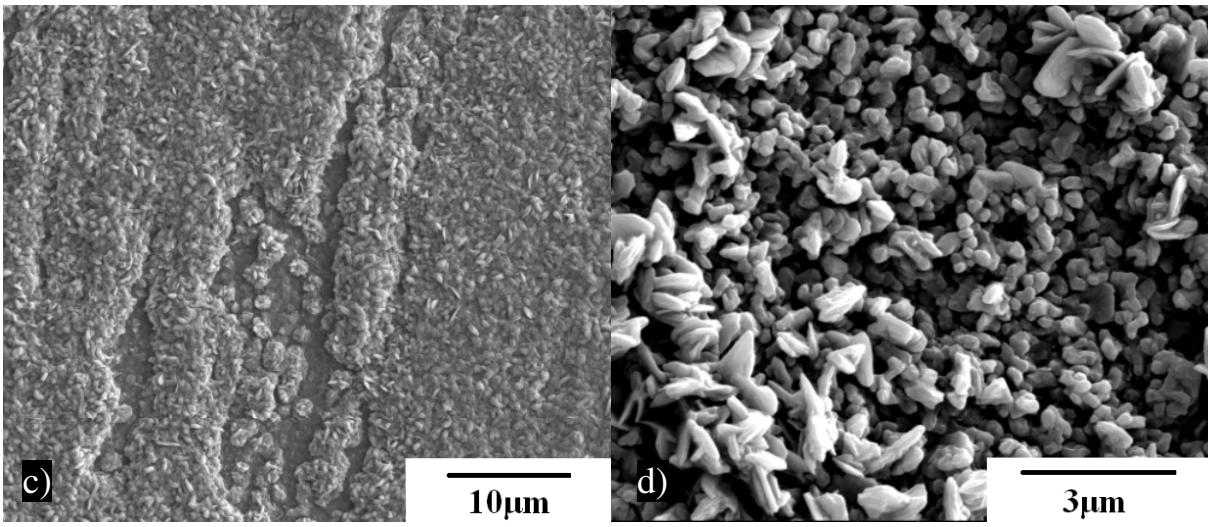

Fig. 4.13 Oxide scale morphologies developed on Aluchrom exposed to 3% humid air for 500 h: (a&b) at 850 ^{o}C, and (c&d) at 950 ^{o}C

The oxides present in the scale were identified to be α, γ and θ forms of Al_2O_3, by XRD (Fig. 4.14). An increase in humidity to 12% and/or temperature to 950 ^{o}C resulted in distinct development of platelets of oxide (Fig. 4.13 c&d, and 4.15 a-d), in addition to the kind of scale that was observed in 3% humidity air at 850 ^{o}C. XRD analysis of the scales suggested disappearance of peaks of γ and θ forms of aluminum oxide in the case of the scales developed at 950 ^{o}C (Fig. 4.14). It is noted that γ and θ forms of Al_2O_3 that are inherently metastable tend to be unstable at higher temperatures [96, 97], which explains the exclusive peaks for α Al_2O_3 in the scan for sample exposed for 500 h at 950 ^{o}C in Fig. 4.14. Therefore, it is inferred that the transformation to α Al_2O_3 took place at the expense of the metastable γ and θ Al_2O_3 that had formed during heating through lower temperatures.

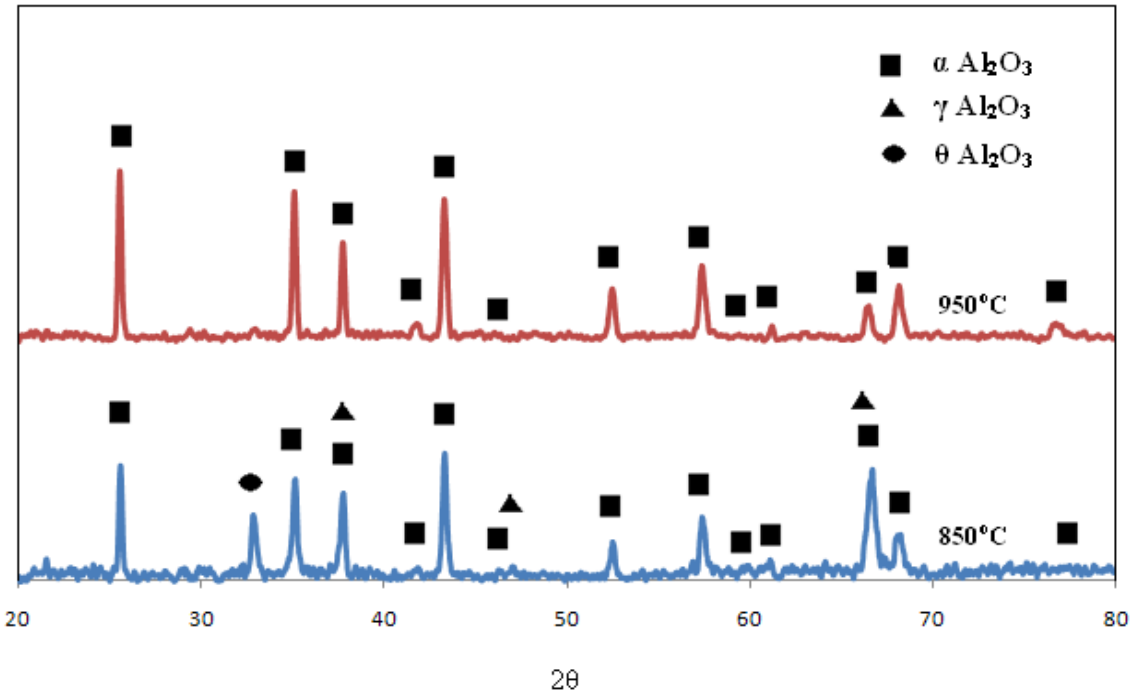

Fig. 4.14 XRD patterns of the oxide scales developed on Aluchrom upon chromium evaporation tests for 500 h at 850 and 950°C with 3 % water

Also, the scales on the samples tested at the higher humidity (12 %) had developed greater areas of localized overgrowth (Fig. 4.15).

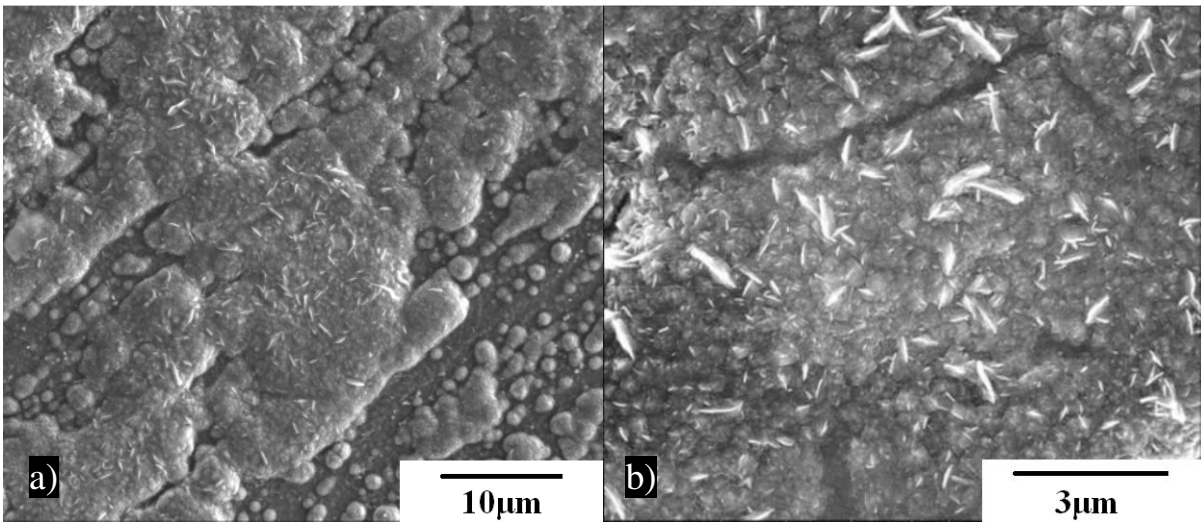

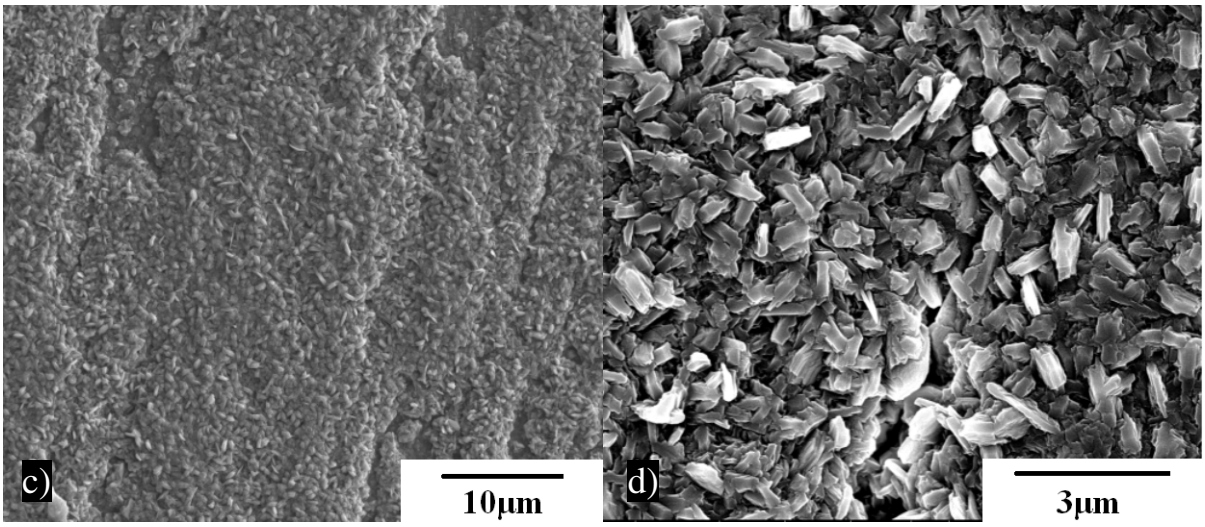

Fig. 4.15 Oxide scale morphologies developed on Aluchrom exposed to 12% humid air for 500 h: (a&b) at 850°C and (c&d) at 950°C

SEM images of FIB cross sections in Figure 4.16 show morphology of oxide scales developed on Aluchrom in 500 h at 850 and 950 °C and in 3 and 12% humidity air. The alumina scale developed at 850 and 950 °C in 3% humidity air remained compact and uniform in thickness (Fig. 4.16 a&b) which is consistent with the low evaporation rates in 3% humidity air. However, these scales were found to be columnar at a higher magnification, with some degree of porosity, which may still facilitate chromia transport through these scales, thus, accounting for the significant chromia evaporation under the given experimental condition (Fig. 4.6), in spite of the formation of a reasonably compact alumina layer. Furthermore, it is suggested that the initial development of chromium rich oxides at the gas-metal interface contributed to chromium evaporation before the eventual establishment of the contiguous alumina layer seen in Fig. 4.16a&b. As the data in Fig. 4.6 clearly show, the increase in humidity from 3 to 12% had more predominant influence in chromium evaporation rate than the increase of temperature from 850 °C to 950 °C. The scales developed at the higher humidity (12 %) were considerably non-uniform in thickness. The areas of greater thickness (that showed up as overgrowth in Fig. 4.15 a) and possessed defects such as porosities (Fig. 4.16c&d) that could allow chromia diffusion, thus accounting for considerably greater evaporation rate in air with 12% humidity (Fig. 4.6).

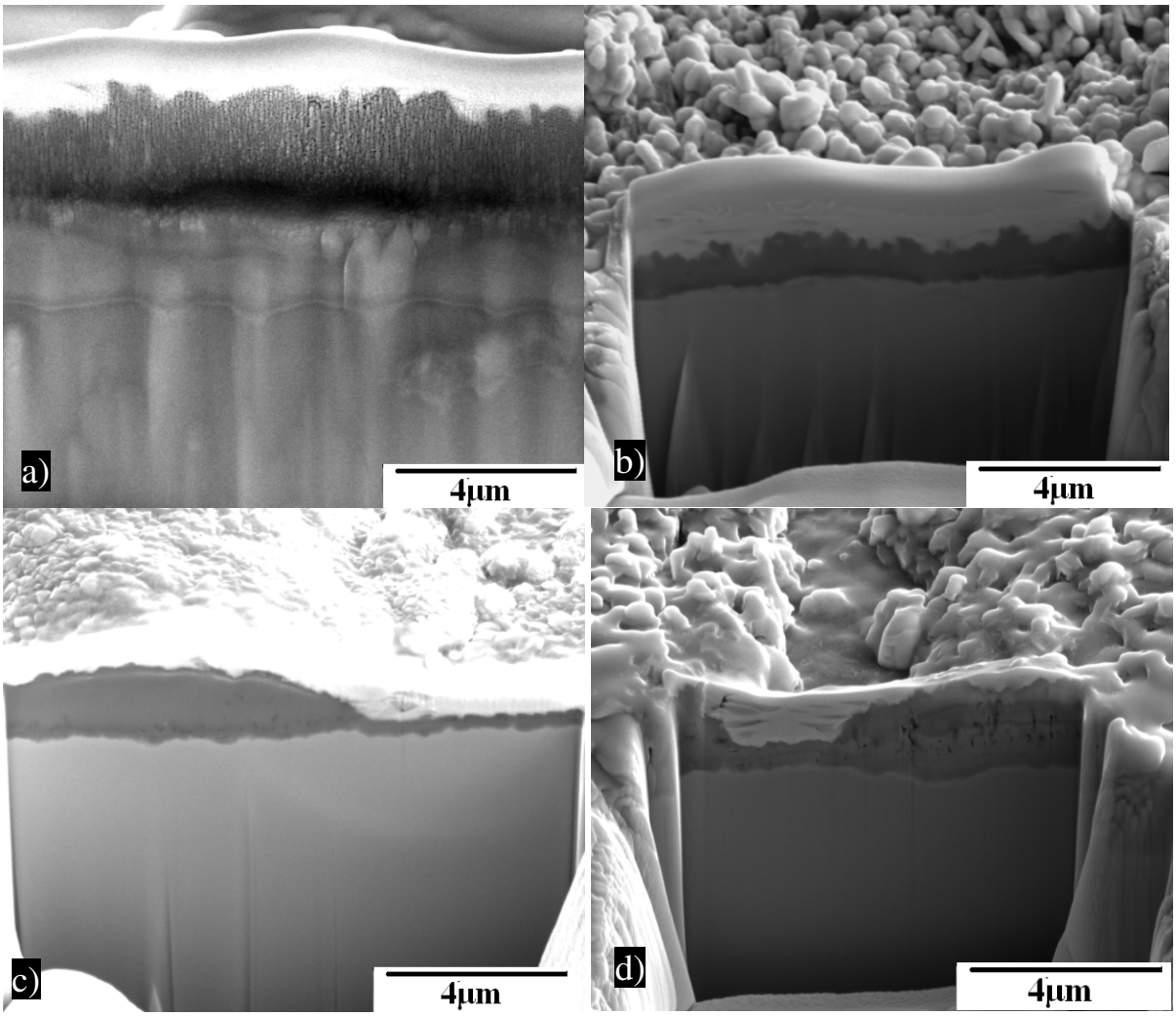

Fig. 4.16 SEM images of FIB cross sections showing morphology of oxide scales developed on Aluchrom in 500 h at 850 and 950 °C) and in 3 and 12% humidity air: (a) 850 °C and 3% humidity, (b) 950 °C and 3% humidity, (c) 850 °C and 12% humidity, and (d) 950°C and 12% humidity

4.2.4 Oxide scale formation and characterization of Alumina forming austenitic (AFA)

Alumina forming austenitic (AFA) stainless steel, AFA OC-4 developed a scale with considerably non-uniform topographic features (Fig. 4.17a) during 500 h exposure in 3% humidity air at 850 °C. Similar features were observed for samples tested for 500 h at 800 and 900 °C in 3% humid air. As became

evident at a higher magnification, the non-uniform topography of the scale was the result of the regular formation of overgrown oxide (Fig. 4.17b).

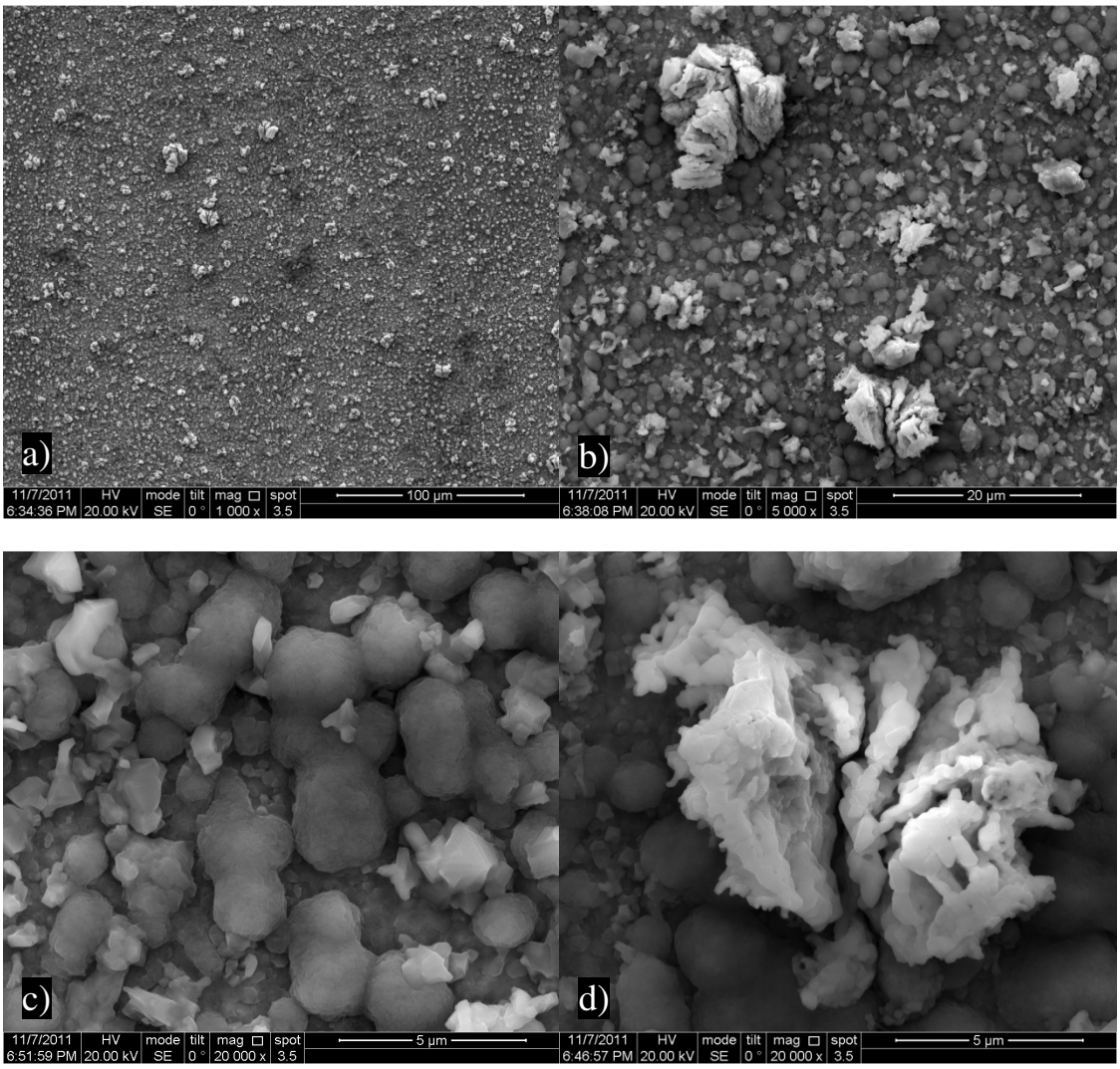

Fig. 4.17 Oxide scale morphology developed on AFA-OC4 for 500 h at 850°C in 3% water environment a), b),c),d

The primary scale of nodular oxides (Fig. 4.17c) was analyzed using EDS, and determined to be predominantly Al rich oxide, whereas, the overgrown oxide (Fig. 4.17d) was primarily Nb rich oxide. Fig. 4.18 shows the cross-sections of the AFA OC-4 alloy after oxidation for 500 h in 3% humid air at 800, 850 and 900 °C. The scales developed at different temperatures were similar, i.e., the aluminum-rich

oxide covering the surface with Nb-rich oxide overgrowth at some locations. It appears that the B2-NiAl phase in the alloy (which acts as aluminum reservoir) dissolved to facilitate alumina scale formation, resulting in development of a well-defined precipitation-denuded zone.

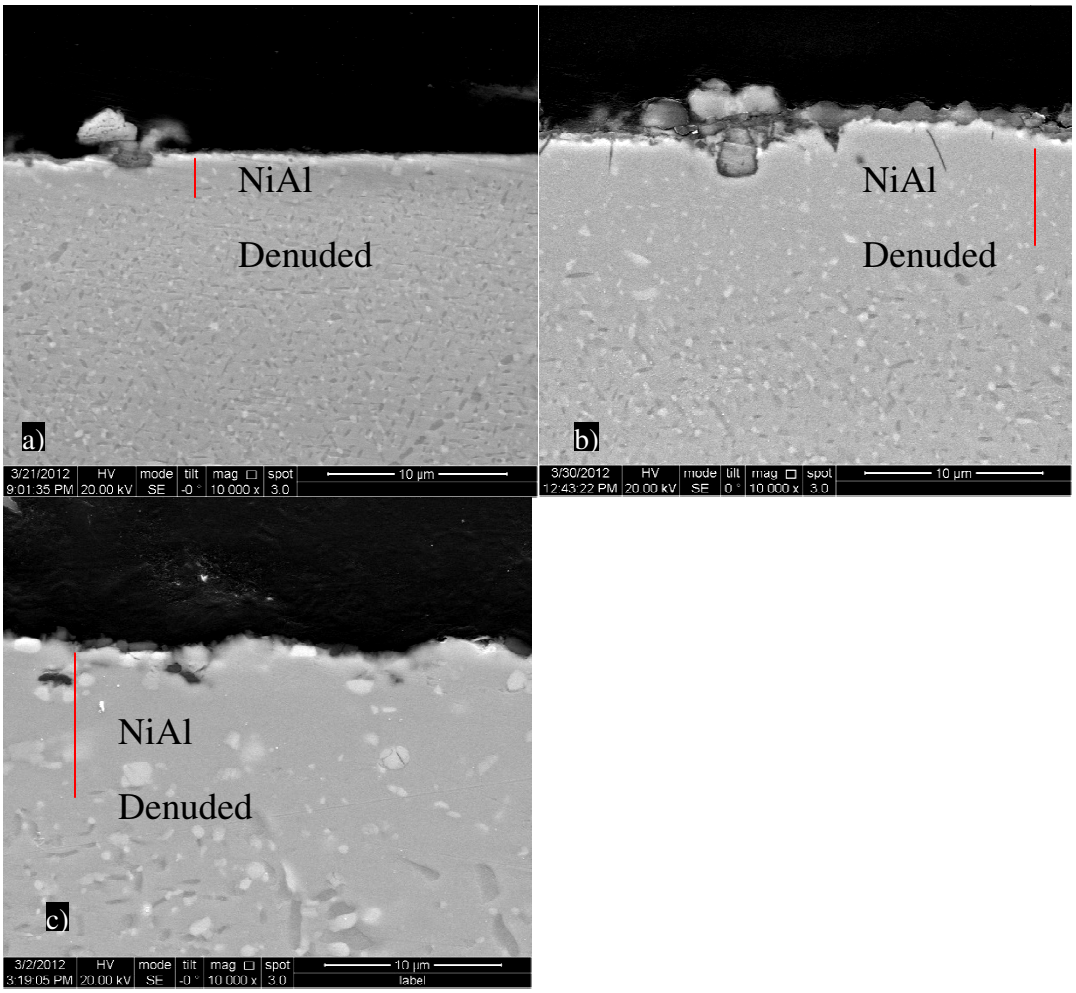

Fig. 4.18 SEM images of cross-section of AFA-OC4 after 500 h test in 3% water environment at a) 800°C, b) 850°C, c) 900°C

Though the width of the precipitate-free zone was the least in the case of the specimen oxidized at 800 °C (Fig. 4.18), indicating the least degree of NiAl precipitate dissolution, even this sample had developed a full-fledged alumina layer (as seen in Fig. 4.19). As an interesting observation, EDS has suggested Al level in the denuded zone to remain at 2-2.5 wt. % (which is similar to the solubility limit of aluminum in

austenite), indicating that even though aluminum was extensively used up for development of a full-fledged alumina layer (Fig. 4.19), aluminum thus used up was adequately replenished due to the dissolution of the NiAl precipitates.

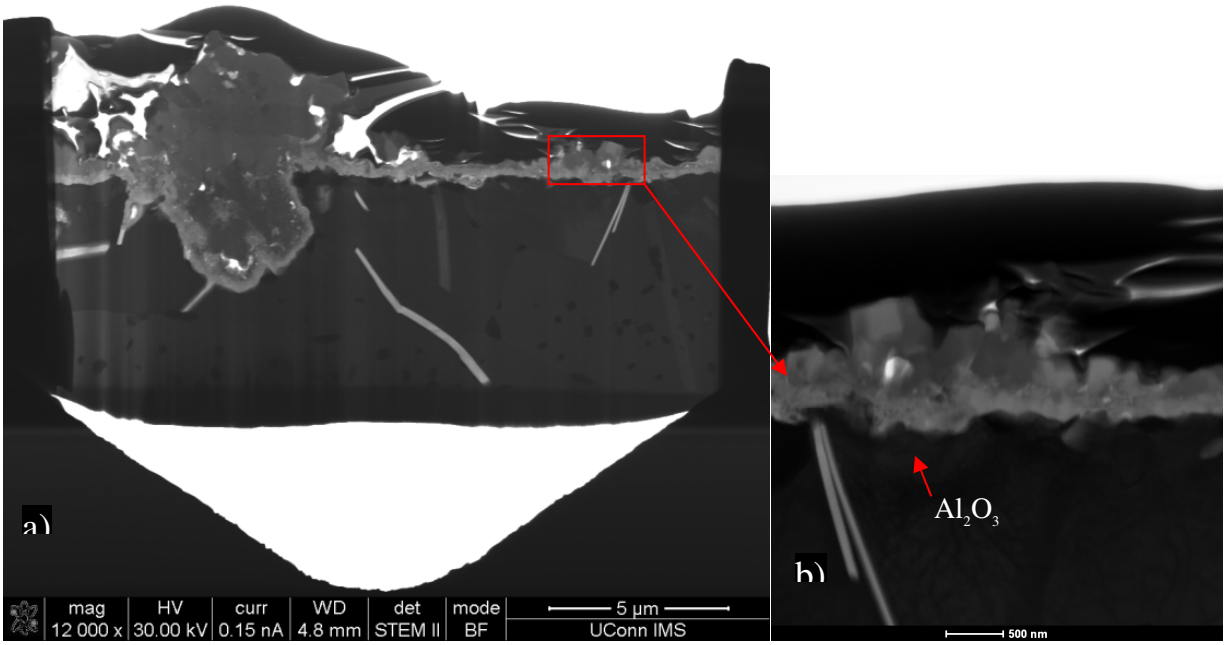

Fig. 4.19 STEM images of FIB cross-section of AFA-OC4 after 500 h test in 3% water environment at 850^{o}C a) b)

An adequate availability of aluminum ensured the alumina rich scale to be continuous (i.e., without any disruption). A closer look of alumina rich oxide scale suggests a two-layer scale (Fig. 4.19), i.e., an outer layer of mixed oxide and a continuous aluminum oxide layer underneath. The top mixed oxide layer that contains Al, Cr, Fe, Ni, Nb and Mn. An XRD scan of the scale (Fig.4.20) suggests a predominant formation of aluminum rich oxide, with some chromium, niobium and iron contents.

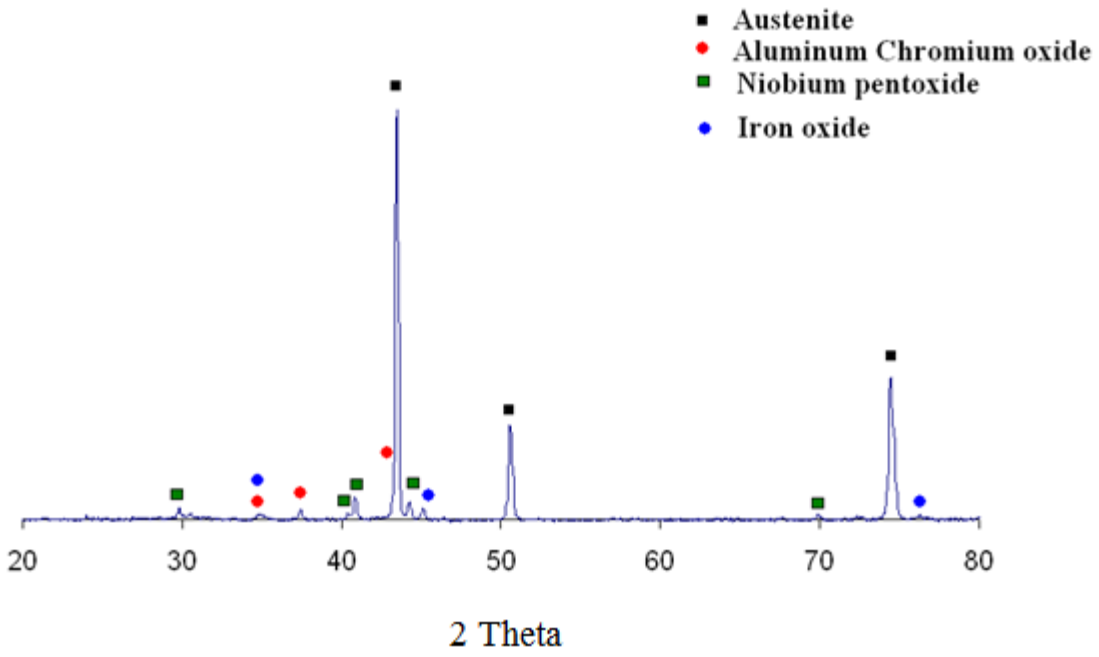

Fig. 4.20 XRD patterns of the oxide scales developed on AFA-OC4 upon chromium evaporation tests for 500 h at 850°C in 3% water environment

The high intensity peaks of the austenite substrate indicate that oxide scale is rather thin, which might have facilitated Cr evaporation rate of the AFA OC-4 alloy (as compared to another alumina former Aluchrom, on which formation of a single layer alumina scale has been reported . Morphology of the oxide scale developed upon exposure for 500 h in 3% humidity air at 850 °C (Fig. 4.17 & Fig. 4.18 b) provides an evidence of overgrowth of Nb-rich oxide, 'bursting' out of metal surface. It is well established that this alloy would develop an alumina scale under the given experimental condition [98-106]. It is important to understand whether the formation of the overgrown areas of Nb oxide might have caused any disruption in the alumina scale, thereby contributing to the evaporation of chromia. However, observation of the cross-section of the scale developed (Fig. 4.21) suggests that the overgrowing Nb-rich oxide was undercut by the continuous alumina layer. It may be possible to understand this behavior in the light of the alloy microstructure and the properties of Nb oxide. As briefly described before, one of the purposes of adding Nb to the AFA OC-4 alloy is to develop nano size Nb-based carbide for precipitation strengthening to increase the creep resistance at high temperatures.

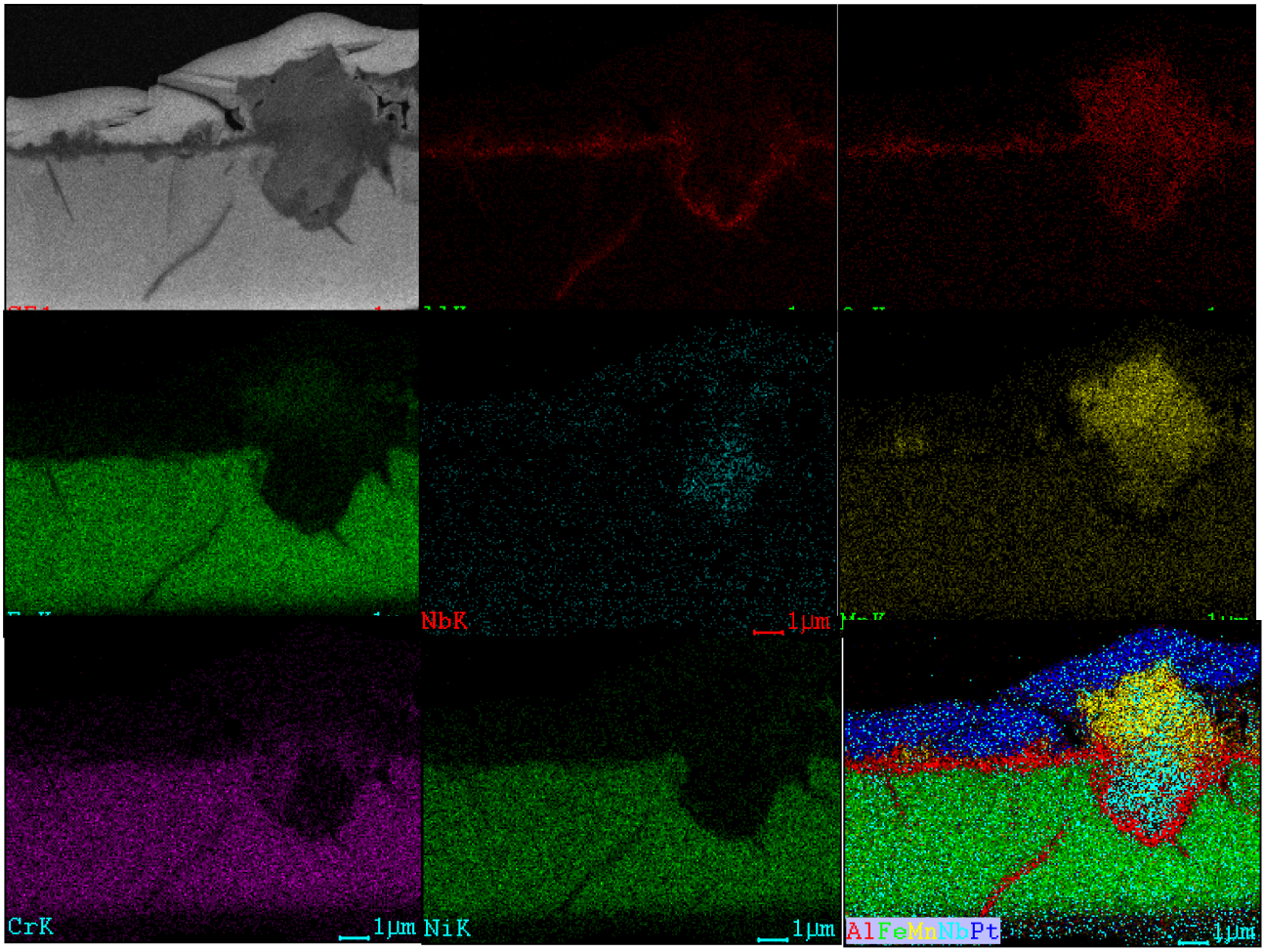

Fig. 4.21 EDS elemental mapping of FIB cross-section of AFA-OC4 after 500h test in 3% water environment at 850^{o}C

However, our observation shows the micro-size NbC precipitates on the polished surface (Fig. 4.22 a & b) and in the sub-surface of the polished cross-section (Fig. 4.22 c). These Nb carbide precipitates seem to have a profound influence also on the mechanical stability of the oxide scale, seen as 'bursting' of Nb-rich oxide.

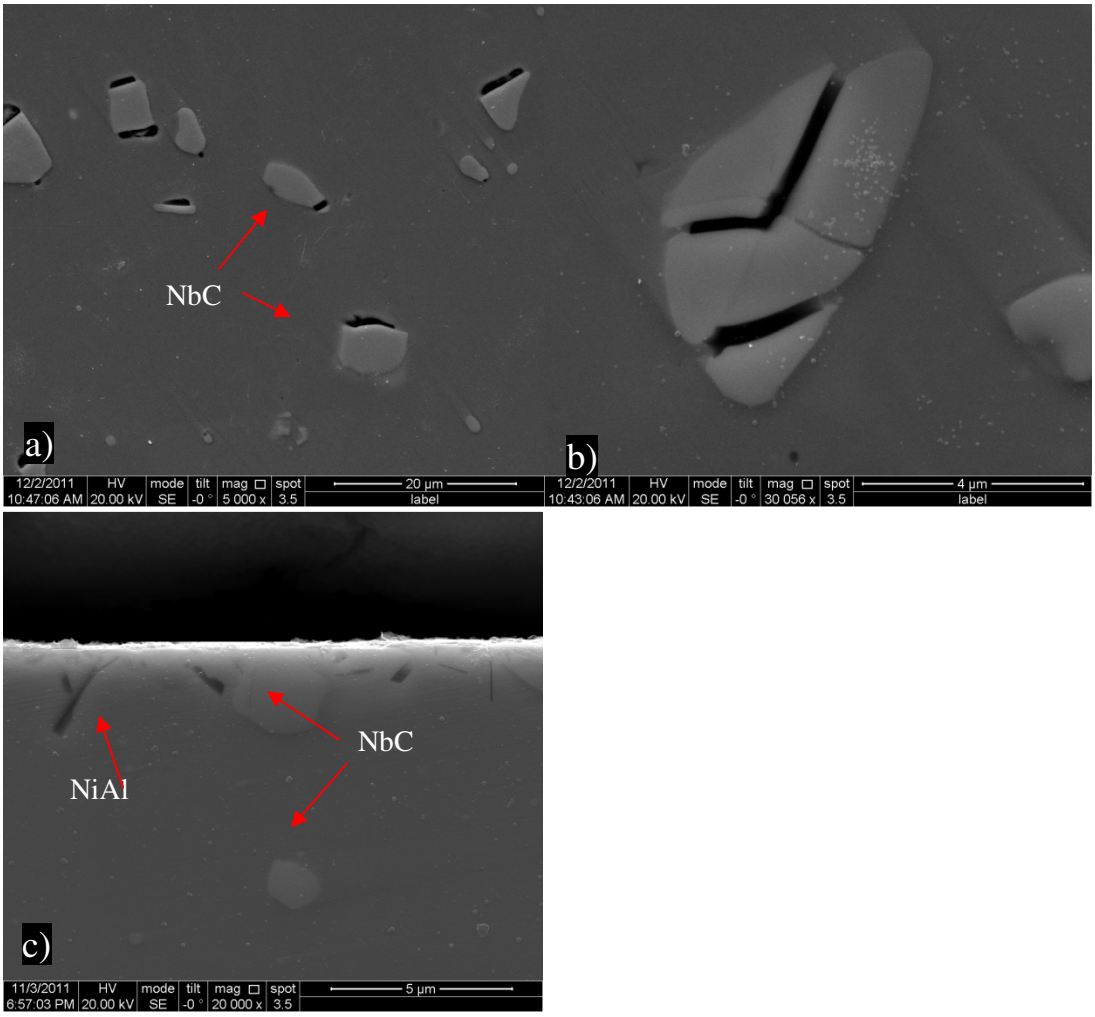

Fig. 4.22 SEM images of: a), b) as polished surface, and c) cross-section of AFA-OC4

An alumina scale will develop over rest of the sample surface, whereas, at the locations of NbC precipitates, an initial thin layer of Nb-oxide (Nb_2O_5) will form. Subsequent growth of oxide at the locations of NbC precipitates will progress by inward diffusion of oxygen through the initial Nb-oxide layer [65]. Further oxidation of NbC will generate considerable stress at the alloy-scale interface (because of the considerable increase in volume when NbC oxidized to Nb_2O_5). Such stress can cause cracking in the Nb_2O_5 formed [107], and pathways (cracks). Cracking of the scale will allow diffusion of molecular oxygen to the alloy/scale interface and further oxidation at the interface to form alumina layer. In fact, it

is suggested that the cracking in the scale was further accentuated since one of the reaction products of oxidation of NbC is CO

$$2NbC + 7/2\ O_2 \rightarrow Nb_2O_5 + 2CO\ (g) \qquad (4.1)$$

which possibly generated enough stress to cause 'bursting' of Nb-rich oxide shown in Fig. 4.17d. The short term oxidation experiments have shown the formation of Nb_2O_5 to be so rapid that even in 5 min exposure in 3% humidity air at 850°C, similar Nb-rich oxide was observed on metal surface. It is inferred, therefore, that in spite of the localized overgrowth of Nb-rich oxide, the protective alumina film rapidly establishes and acts as an effective barrier for any outward Cr transport from the alloy bulk. In order to understand the scale growing mechanism, it is important to understand how the scale is formed at the early stages of the oxidation. Fig. 4.23 shows the weight change of the AFA-OC4 upon exposure for 20 h in dry air at 750, 850 & 950 °C.

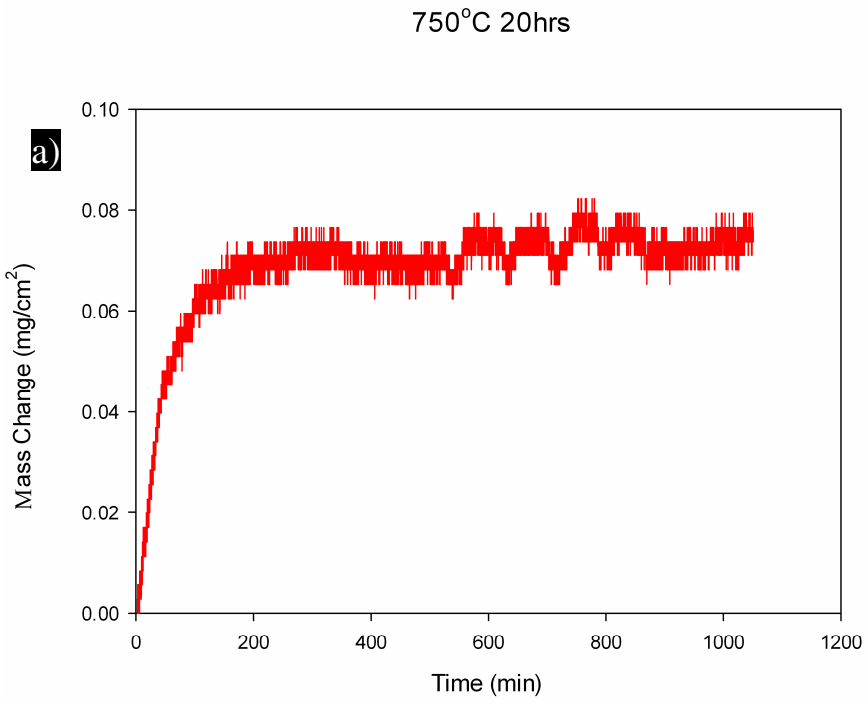

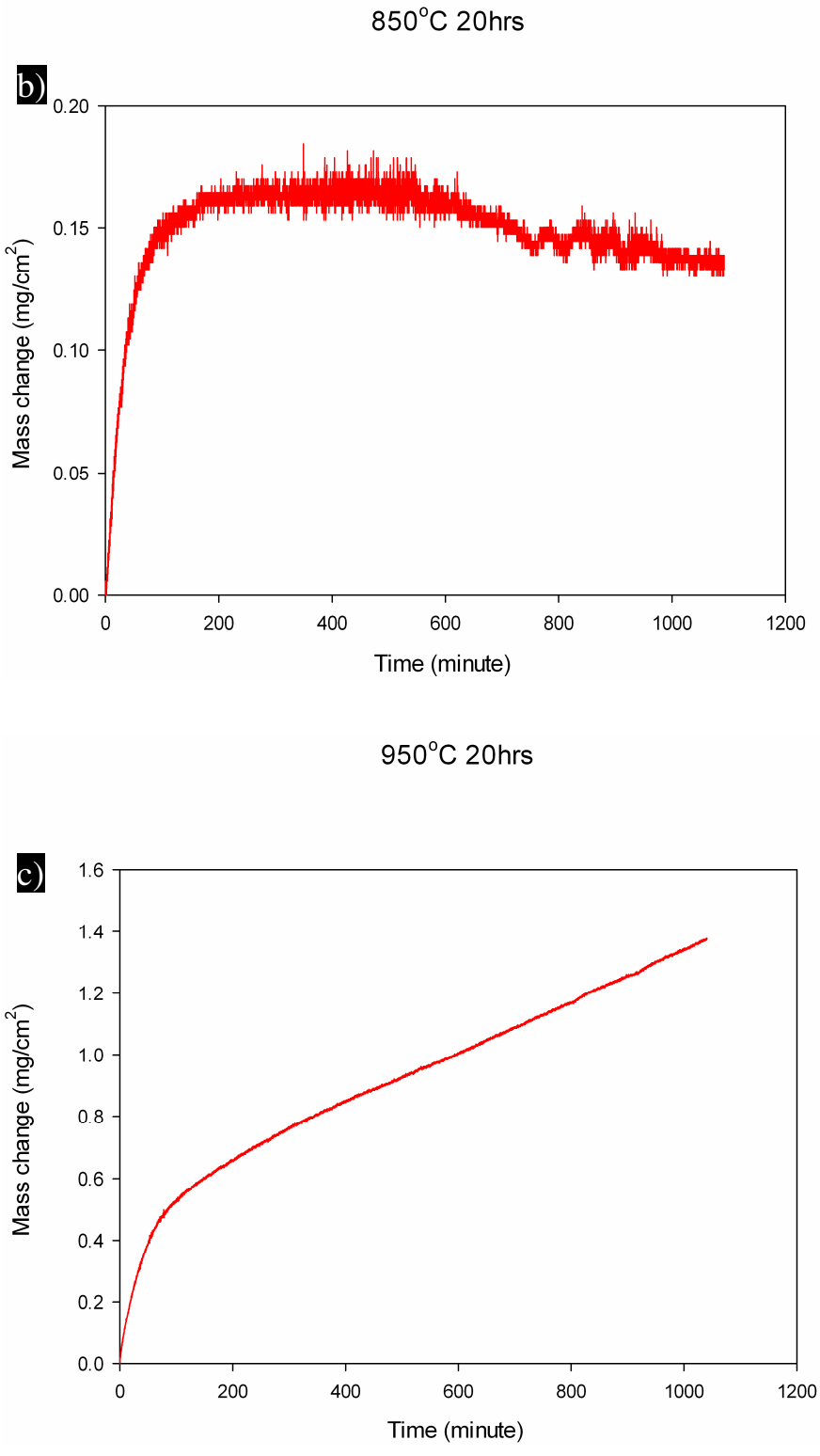

Fig. 4.23 Mass change in air for 20 h at a) 750°C, b) 850°C c) 950 °C

The calculated parabolic rate constant of initial oxidation indicates that the rate to be very close to the reported data for Cr_2O_3 formation [65]. The early stage of transient Cr_2O_3 formation could contribute to the Cr vapor species when measured in the Cr evaporation experiment. Also, although the undercutting alumina layer was formed, the Cr_2O_3 that remained in the mixed oxide layer of the scale would continually contribute to the Cr evaporation. AES profiles for Al, Cr and O (Fig. 12) in the thin oxide scales developed in the very early stages (1 and 5 min) of oxidation suggest a gradual enrichment of Al in the inner scale (indicating that it takes some time before the full-fledged alumina layer establishes), whereas the external layer of mixed oxides (including Cr oxide) would start to develop instantaneously.

(a)

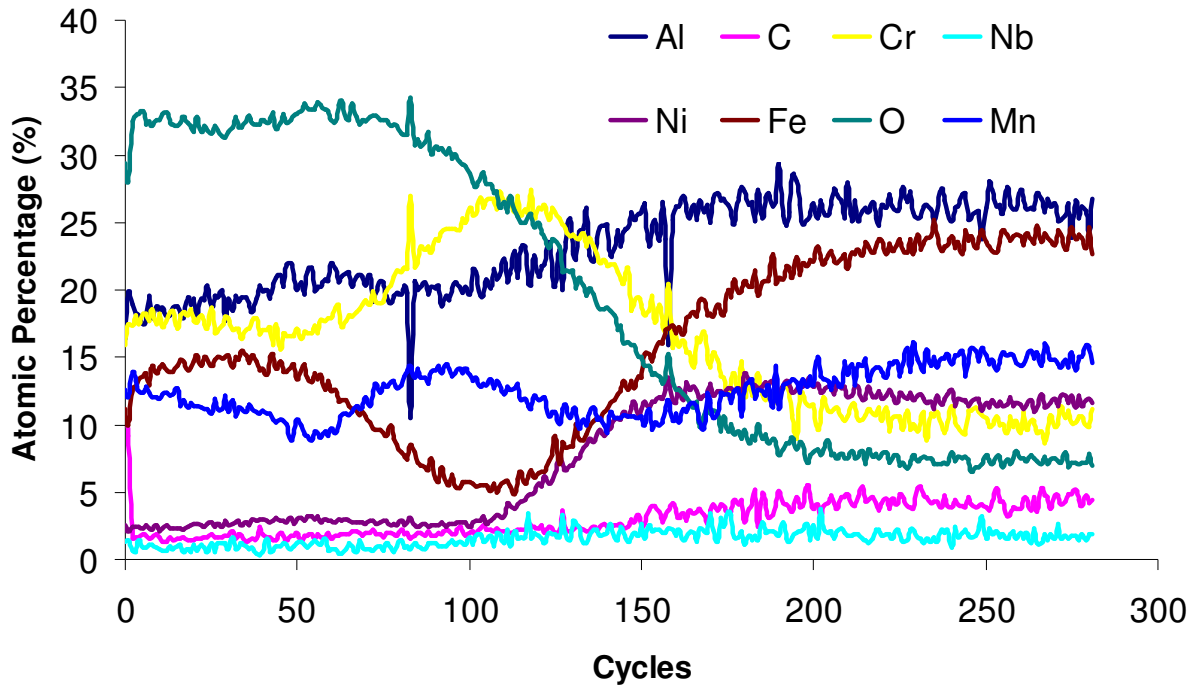

(b)

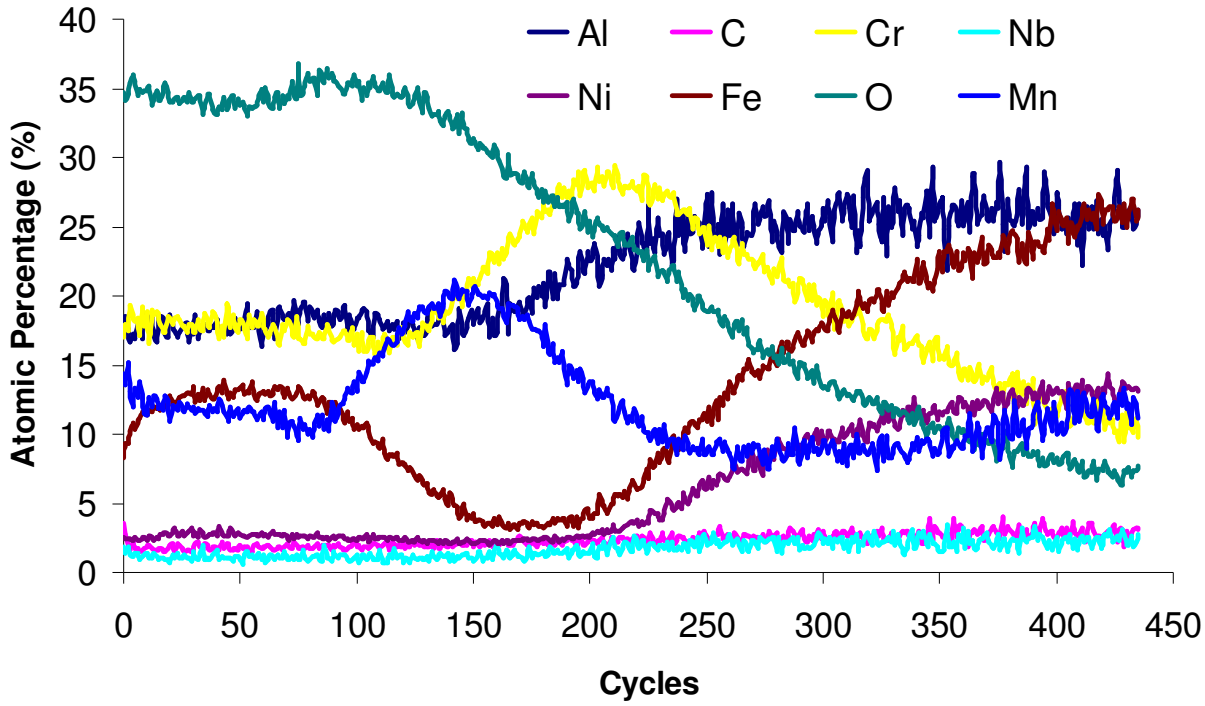

Fig. 4.24 AES profiles for different elements in the thin oxide scale of AFA stainless steel oxidized at 850 ^{o}C for: (a) 1 min and (b) 5 min

Until the full-fledged inner layer of alumina has established, outward diffusion of Al, Cr, Fe, Ni, Nb and Mn and formation of the mixed oxide will continue. Cr thus available at the outer surface will result in Cr evaporation. It is also possible that since the Nb-oxide bursts that start to form quite early (as seen in Fig. 4.25) could disrupt this initial scale and aid in Cr evaporation. Fig. 4.26 shows the schematic of rapid establishment of the full-fledged inner layer of alumina after initial oxidation of AFA, which retards the outward diffusion of Cr. Therefore, Cr evaporation will be limited by Cr available in the external scale of the mixed oxide.

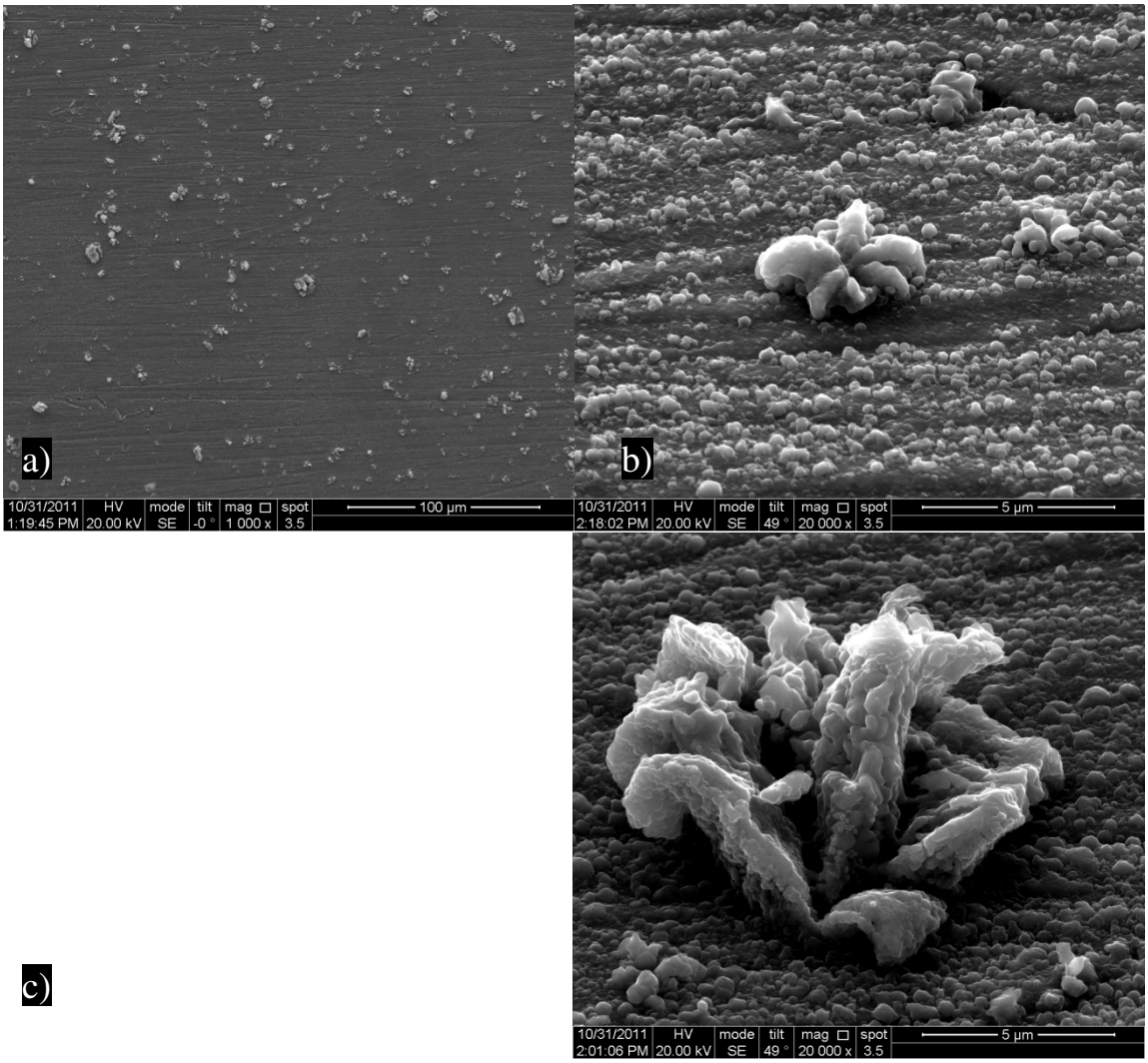

Fig. 4.25 Oxide scale morphologies developed on AFA OC-4 exposed to 3% humid air for 20 h at 850 ^{o}C

a) b) c)

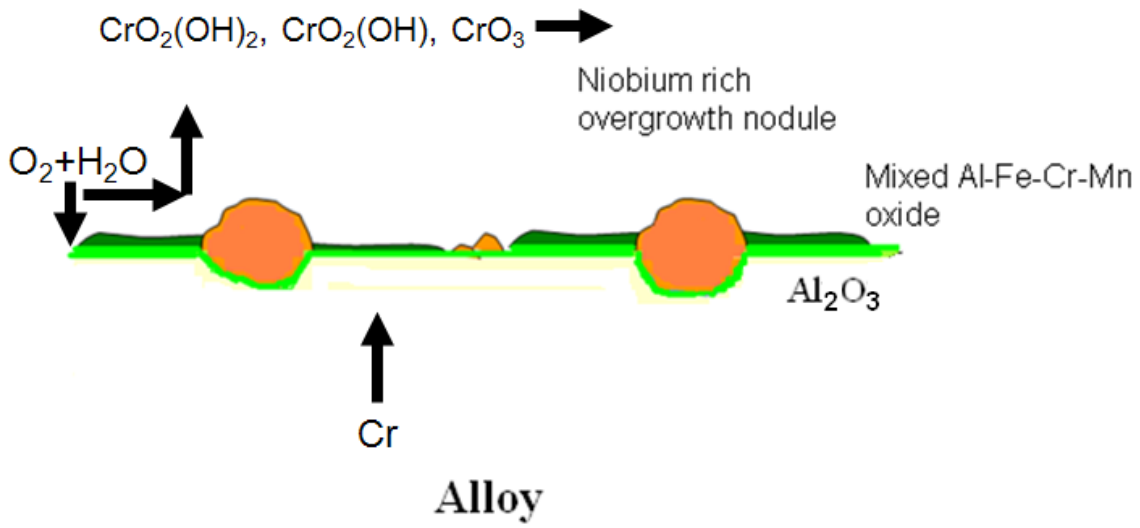

Fig. 4.26 Schematic of rapid establishment of alumina layer that retards Cr evaporation

4.2.5 Oxide scale formation and characterization of AISI 441

The uncoated AISI 441 alloys show a chromium evaporation rate comparable to other chromia forming alloys (AISI 310S). The oxide scale formed after 500 h exposure at 850°C and 3% humidity has regions of localized overgrowth (Fig. 4.27 a&b). At higher magnifications, the localized overgrowth areas were observed with coarse faceted crystals (Fig. 4.27 c); EDS results suggest the overgrowth region is primary chromium-manganese mixed oxide (with ratios approximately as $Mn_{1.5}Cr_{1.5}O_4$) with ~5 wt. % Ti and ~2 wt. % Si. The non-overgrowth areas with faceted fine grains (Fig. 4.27 d) were characterized to be chromium-manganese mixed oxide (with ratios approximately as $MnCr_2O_4$) with less Si (~ 0.5 wt. %). The major fraction of the surface was covered with the faceted fine grains.

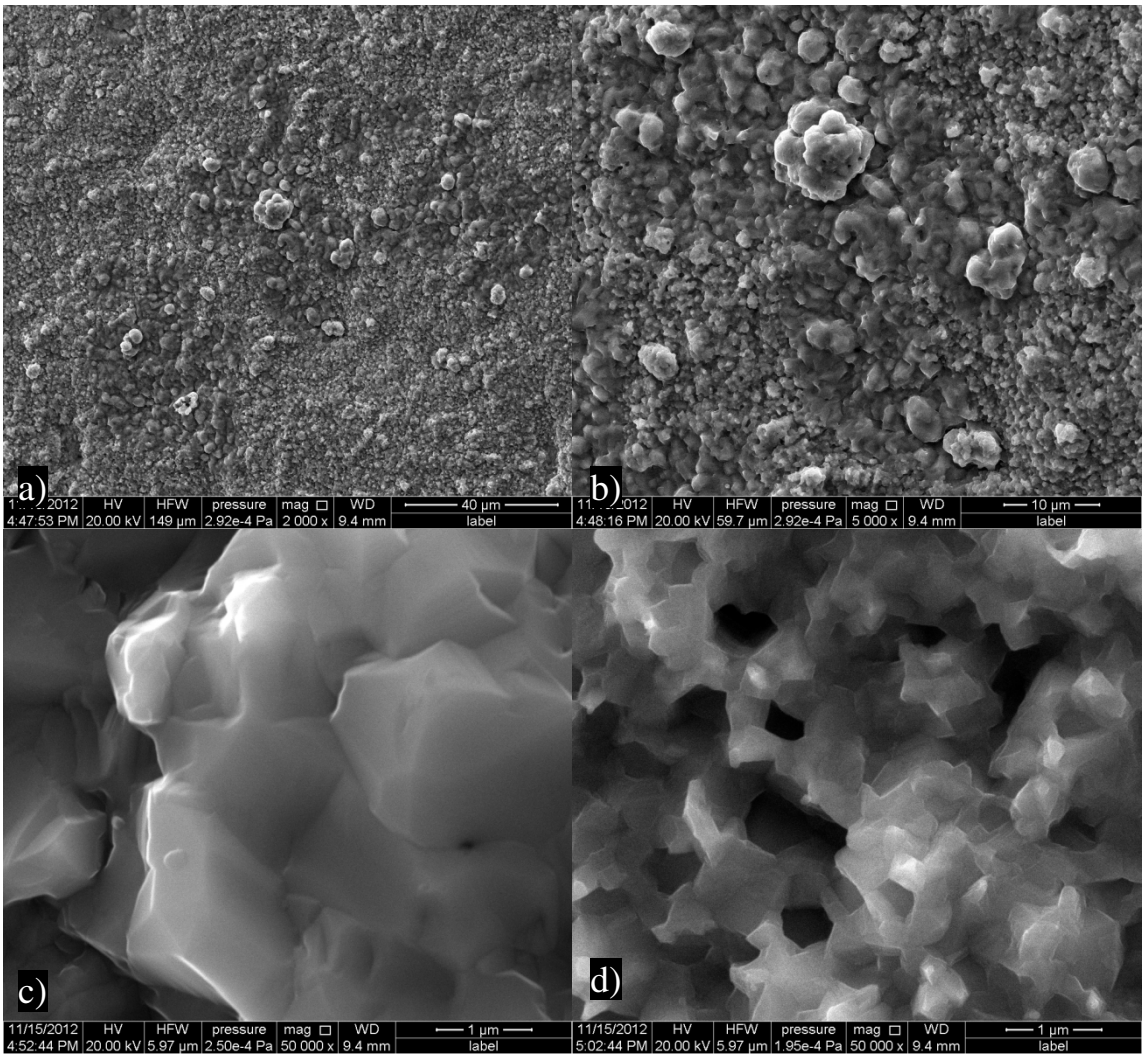

Fig. 4.27 Oxide scale morphologies of AISI 441 exposed to 3% humid air for 500 h at 850°C a) b) c) d)

There is no area of obvious cracks or spallations observed on the alloy surface. To confirm the physical and chemical characteristics across the depth of the oxide scales, a cross-section of an AISI 441 alloy sample exposed to a 3% humidity air for 500 h at 850°C was examined by FIB/STEM/EDS. Fig. 4.28 shows: (a) the outer layer of chromium-manganese mixed oxide ($MnCr_2O_4$) (~1 um thick) with overgrowth of ($Mn_{1.5}Cr_{1.5}O_4$) and occasional TiO_2, and (b) the inner layer of Cr_2O_3 (~3 um thick) underneath the external layer of Cr rich chromium-manganese mixed oxide ($MnCr_2O_4$), (c) internal oxidation of TiO_2 and SiO_2 segregate at the scale/alloy interface. The surface x-ray analysis (Fig. 4.29) confirms the majority of the scale is $MnCr_2O_4$ spinel and Cr_2O_3 with some TiO_2 and SiO_2.

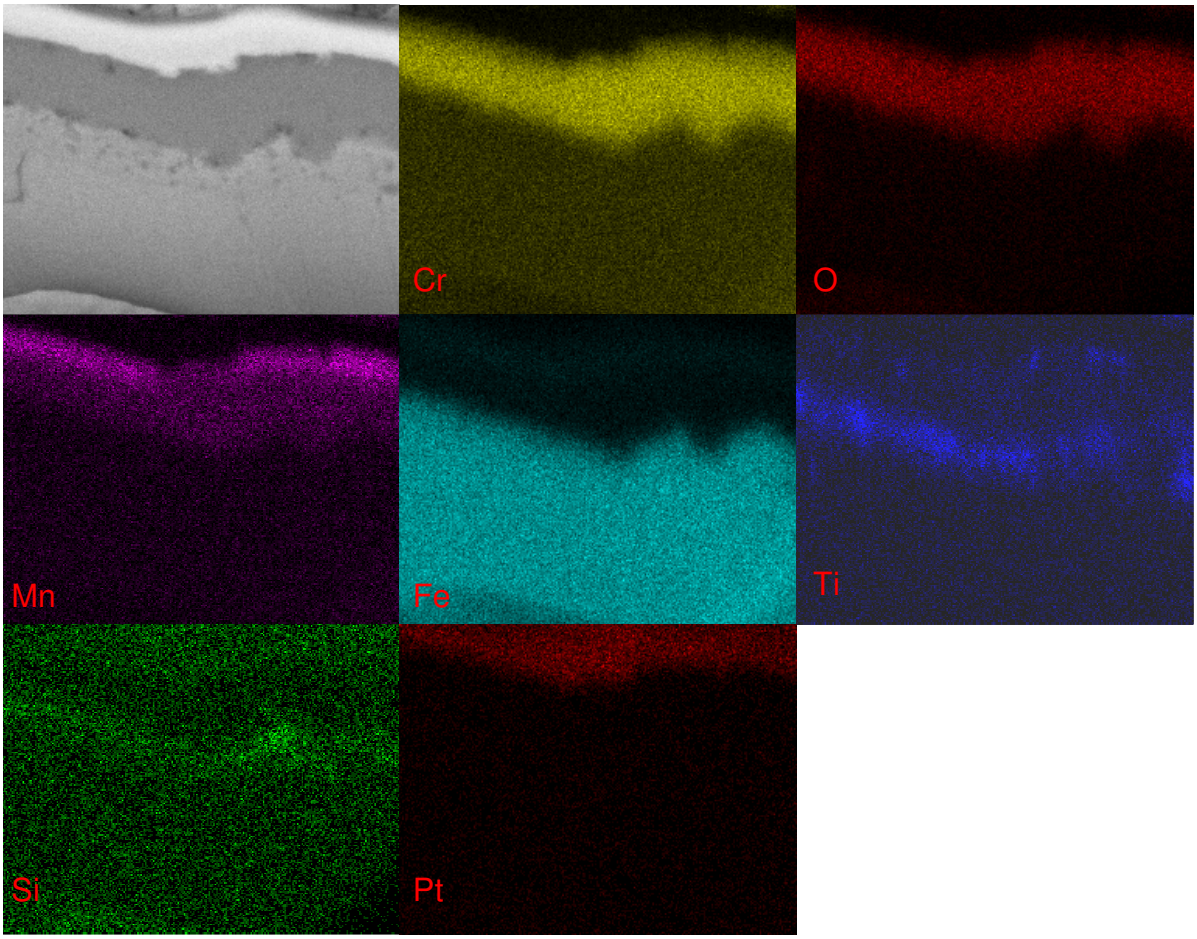

Fig. 4.28 FIB sectioning and SEM images of cross-section of AISI 441 exposed to 3% humid air for 500 h at 850°C

The high chromium evaporation rate of AISI 441 is attributed to the formation of a chromium-rich oxide scale. Generally, the diffusion rate of alloy elements in chromium oxide follows: Mn>Fe>Co>Ni>>Cr [108]. Thus, for ferritic alloys containing Cr and Mn, the oxide scale tends to form a surface $(Mn,Cr)_3O_4$ spinel phase and an inner Cr_2O_3 layer. The presence of the 1% manganese in AISI 441 is accountable for the formation of the outer layer of $(Mn,Cr)_3O_4$ spinel. SiO_2 was observed at the scale metal interface which may reduce the conductivity of the SOFC [23, 26].

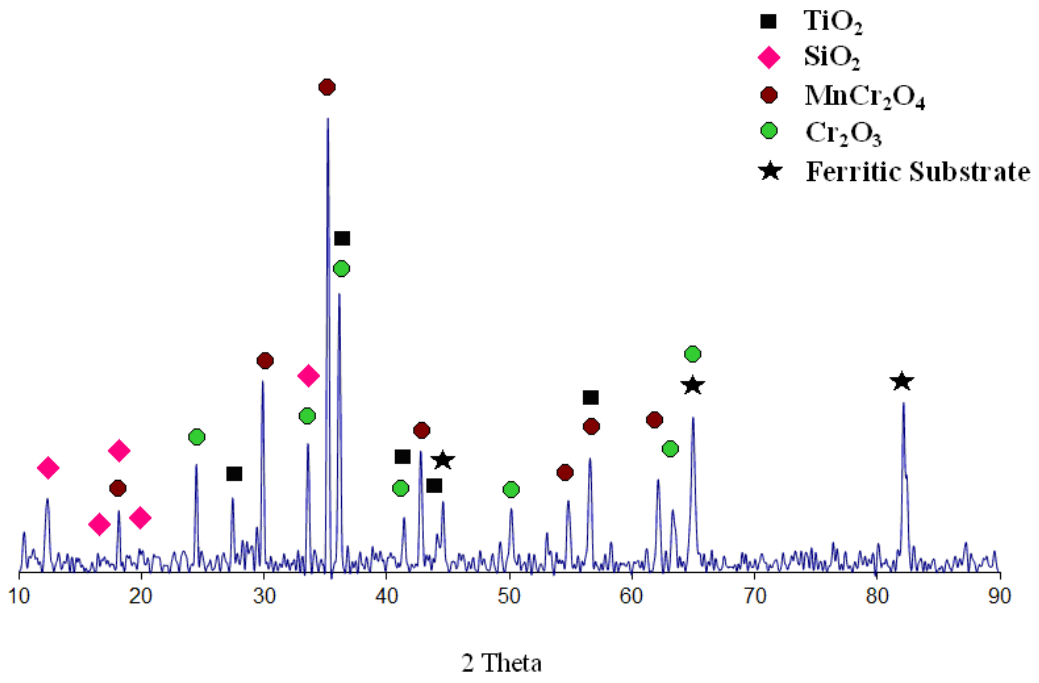

Fig. 4.29 XRD patterns of the AISI 441 exposed to 3% humid air for 500 h at 850°C

The presence of the protective $(Mn,Cr)_3O_4$ spinel can reduce the oxidation rate and mitigate the chromium evaporation rate by an order of magnitude when compared to pure chromia [12]. However, in the case of the AISI 441, the initial formation Cr_2O_3 may lead to a higher chromium evaporation rate with decrease of the rate as the $(Mn,Cr)_3O_4$ spinel gradually forms and covers the Cr_2O_3. This explains the higher chromium evaporation rate observed for AISI 441 compared to $(Mn,Cr)_3O_4$. In this study, no spallation and cracking or delamination of the scale was observed for samples after 500 h test, while Yang et al. found that longer exposure times may lead to localized scale spallation with spallation edges coinciding with alloy grain boundaries and occasional delamination was also observed at the scale/alloy interface which will be detrimental to the performance of it as an interconnect [109].

4.3 Chromium Mitigation via Functional Coating

4.3.1 Evaluation of Manganese Cobalt Oxide Spinel Coated AISI 441

The surface and cross-section images of MCO coated sample after each step during the coating process are shown in Fig. 4.30&4.31. The coating layer (as coated by ASD, Fig. 4.31a) is porous and the thickness is ~ 17 um, the surface (Fig. 4.30a) is covered by MCO spinels. The surface XRD analysis (Fig. 4.32) shows that the as ASD coated coating layer is $Mn_{1.5}Cr_{1.5}O_4$ which at room temperature consists of two phases: cubic Co-rich $Mn_{1+\alpha}Co_{2-\alpha}O_4$ (Space group:) tetragonal Mn-rich $Mn_{2+\delta}Co_{1+\delta}O_4$ (Space group:) α and δ represent a small deviation and are reported [110] by Naka et al. to be less than 0.3 and 0.1 for the cubic and tetragonal spinels, respectively. For simplicity purpose, $MnCo_2O_4$ and Mn_2CoO_4 are used as the standard cubic and tetragonal spinels. Fig. 4.33 shows the elemental mapping of as ASD coated sample by EDS analysis. It is clear that there is no Cr diffusion into the MCO coating layer. After the reducing firing (Fig. 4.31) a chromium rich scale was grown on the metal surface with a cobalt rich metallic layer (with ~4 wt. % Cr, ~10% wt. % Mn) was also formed above and the thickness of the coating layer was reduced to ~9 um. The surface spinel (Fig.4.30 b&c) was reduced to cubic Co metal and MnO (shown as XRD patterns in Fig. 4.32). It is found there is 1~3 wt% Cr and 10~18% Mn associated with Co. The Cr and Mn should be predominantly from the solid state diffusion as Cr and Mn has extensive solid solubility in FCC Co at the reducing firing temperature. The detailed elemental mapping of the coating and substrate interface after the reducing firing (Fig.4.34) shows formation of $(Mn,Cr)_3O_4$ spinel and MnOx at the substrate and coating interface.

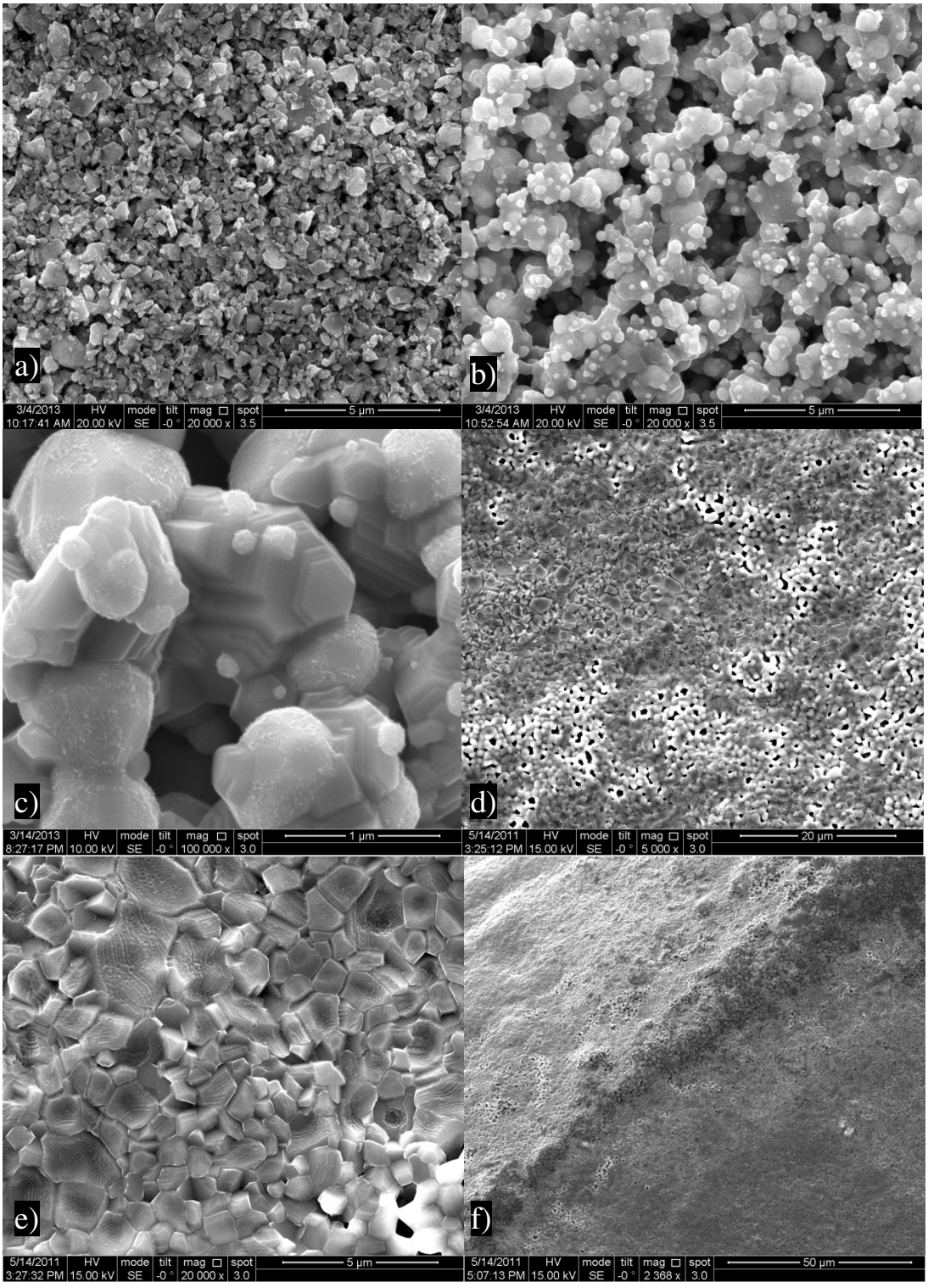

Fig. 4.30 Images of MCO coated AISI 441 surface after each step of the coating process (a) as ASD coated (b) (c) after reducing firing (d)-(f) after re-oxidation firing

The possible gas phase transport of Cr species is negligible as the partial pressure of oxygen in the reduced very low (less than 10^{-16}), the Cr vapor will be negligible too. During the subsequent re-oxidation in air, Yang et al. proposed Co and MnO can react with oxygen to reform the spinel via reactions [111]:

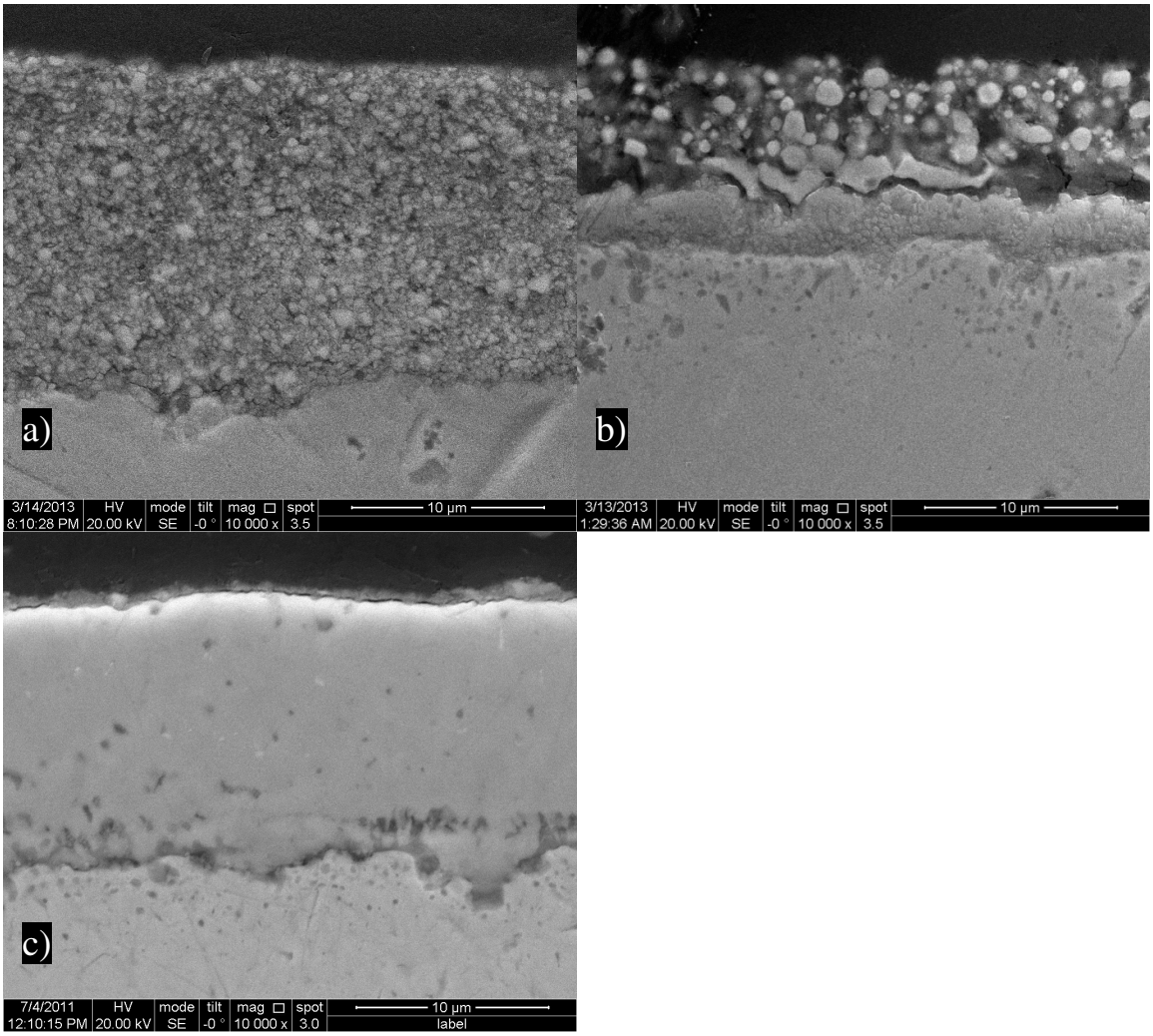

Fig. 4.31 Cross section of MCO coated AISI 441 after each step of the coating process (a) as ASD coated (b) after reducing firing (c) after re-oxidation firing

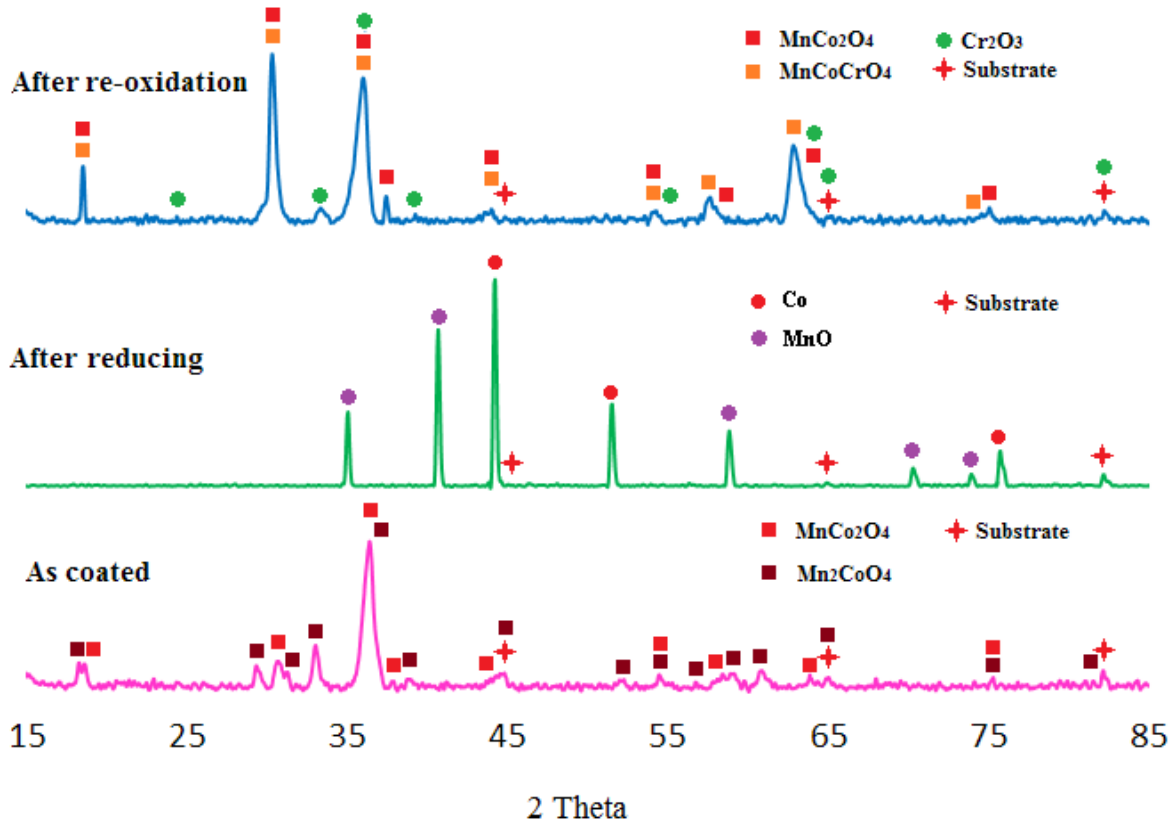

Fig. 4.32 XRD patterns of MCO coated AISI 441 after each step of the coating process

$$4Co+2MnO+3O_2\ (g) = 2MnCo_2O_4 \quad (4.2)$$

$$2Co+4MnO+2O_2\ (g) = 2Mn_2CoO_4 \quad (4.3)$$

Or

$$6Co+6MnO+5O_2\ (g) = 4Mn_{1.5}Co_{1.5}O_4 \quad (4.4)$$

However, based on our observation, a slightly different mechanism is proposed, during the re-oxidation firing process, the metal Co (with 10~18 wt. % Mn) will oxidize to $Co_{3-x}Mn_xO_4$ spinel, MnO can react with oxygen to form Mn_3O_4. With the continuing inward diffusion of Mn from Mn_3O_4 and outward diffusion of Co from $Co_{3-x}Mn_xO_4$ spinel, mixed $MnCo_2O_4$ and Mn_2CoO_4 spinels would form. After re-

oxidation in air, the coating layer (Fig. 4.31c) was densified via this reaction-sintering and the thickness was increased to ~12um.

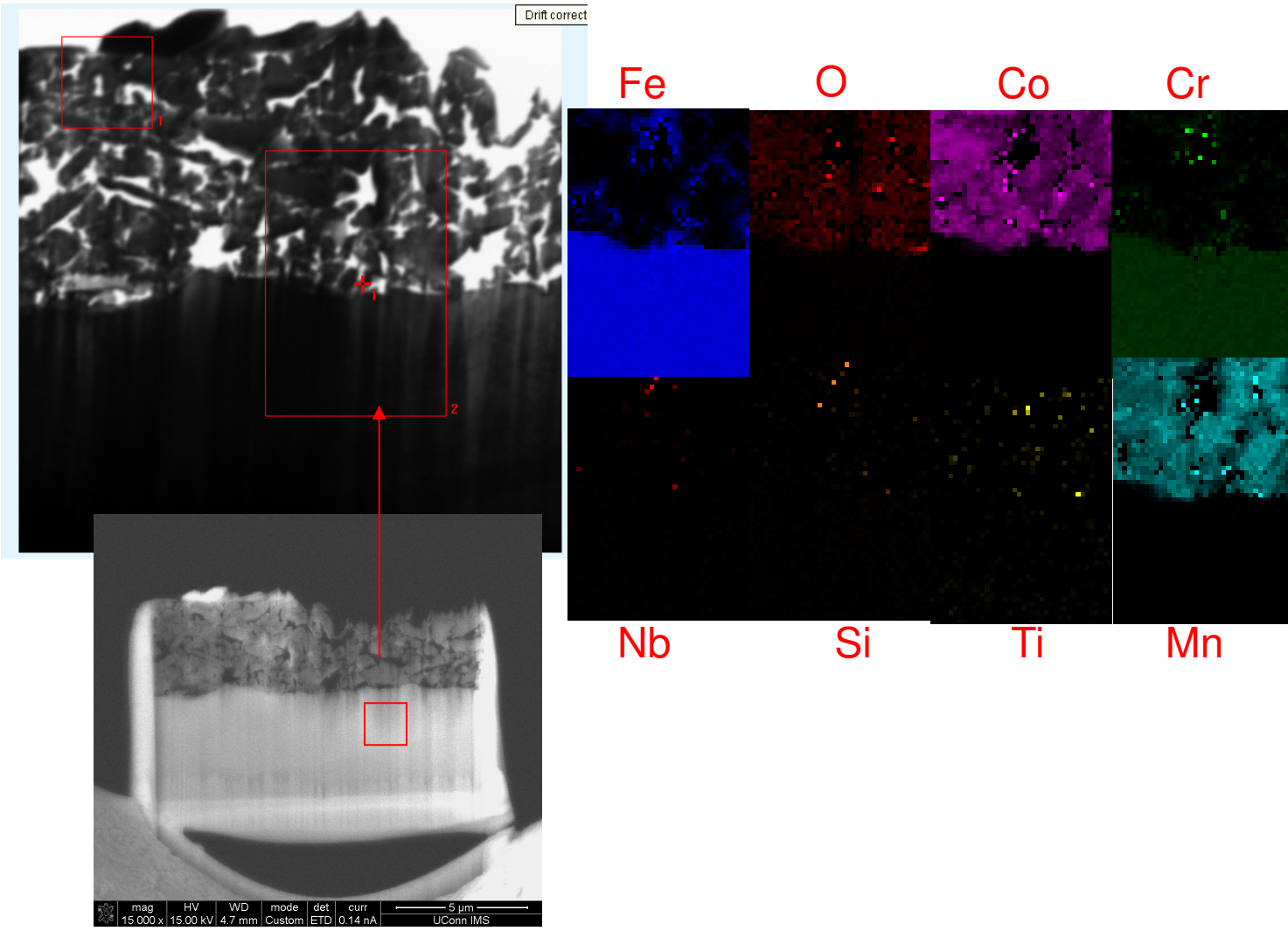

Fig. 4.33 The elemental mapping of as ASD coated sample by EDS analysis

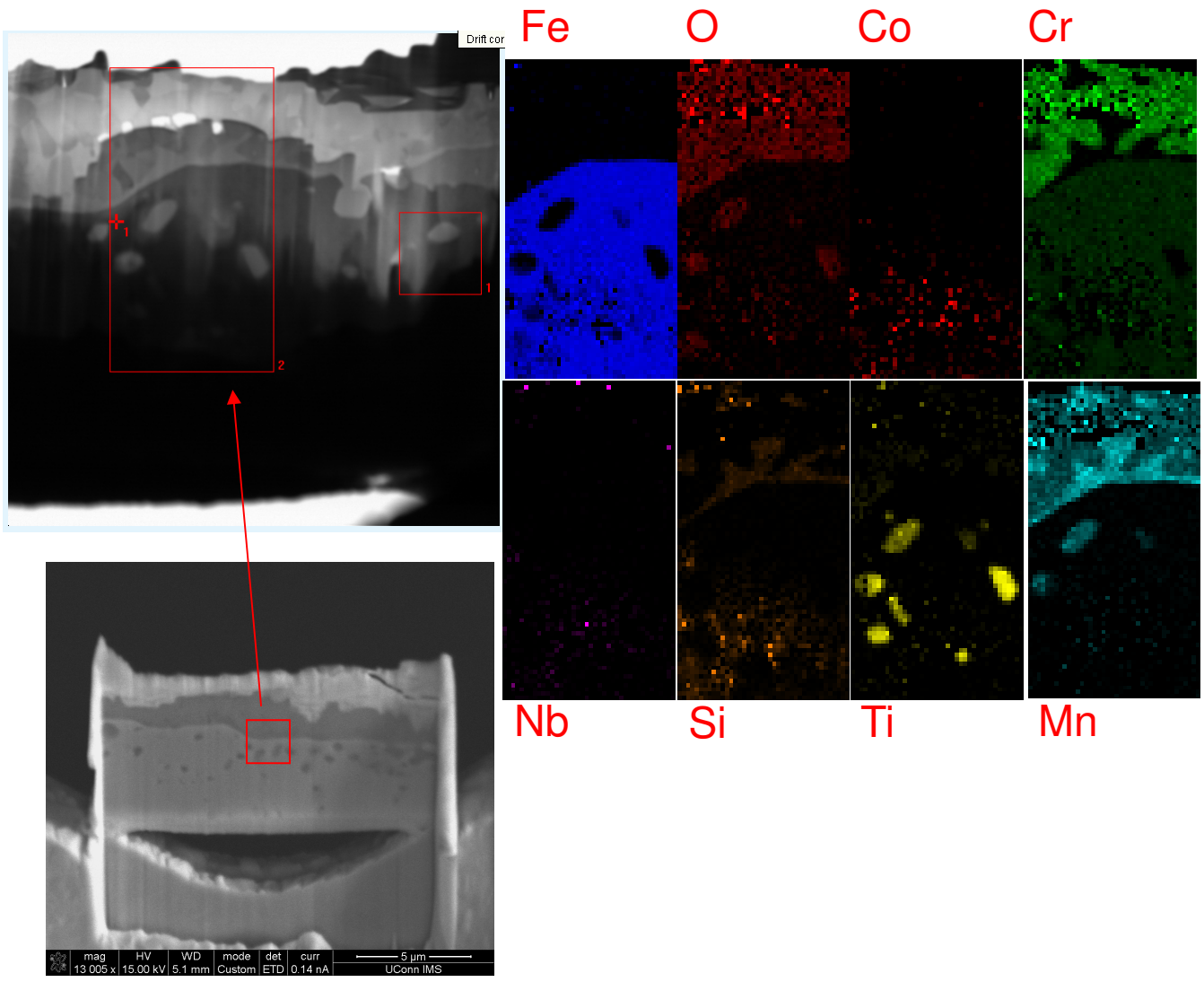

Fig. 4.34 The elemental mapping of as ASD coated sample by EDS analysis after reducing firing

The surface of the coated sample after re-oxidation in air (Fig. 4.30d&e) was covered by rather densely grown crystals with a few closed pores. Fig. 4.30e shows the edges of the sample was also covered by uniform coating. Surface EDS analysis of coating surface shows the chemical composition is close to $MnCo_2O_4$, which is confirmed by XRD (Fig. 4.32) to be cubic $MnCo_2O_4$ spinel structure.

Fig. 4.35 shows the chemical composition profile of the coated sample by EDS point analysis. The outer zone of the coating is primarily $MnCo_2O_4$, the concentration of Mn increases and that of Co decreases as

the coating is extended to its interior zone (the concentration of Mn and Co are approximately equal), and concentration of Cr and Fe in the coating also increases from coating outer zone to inner zone.

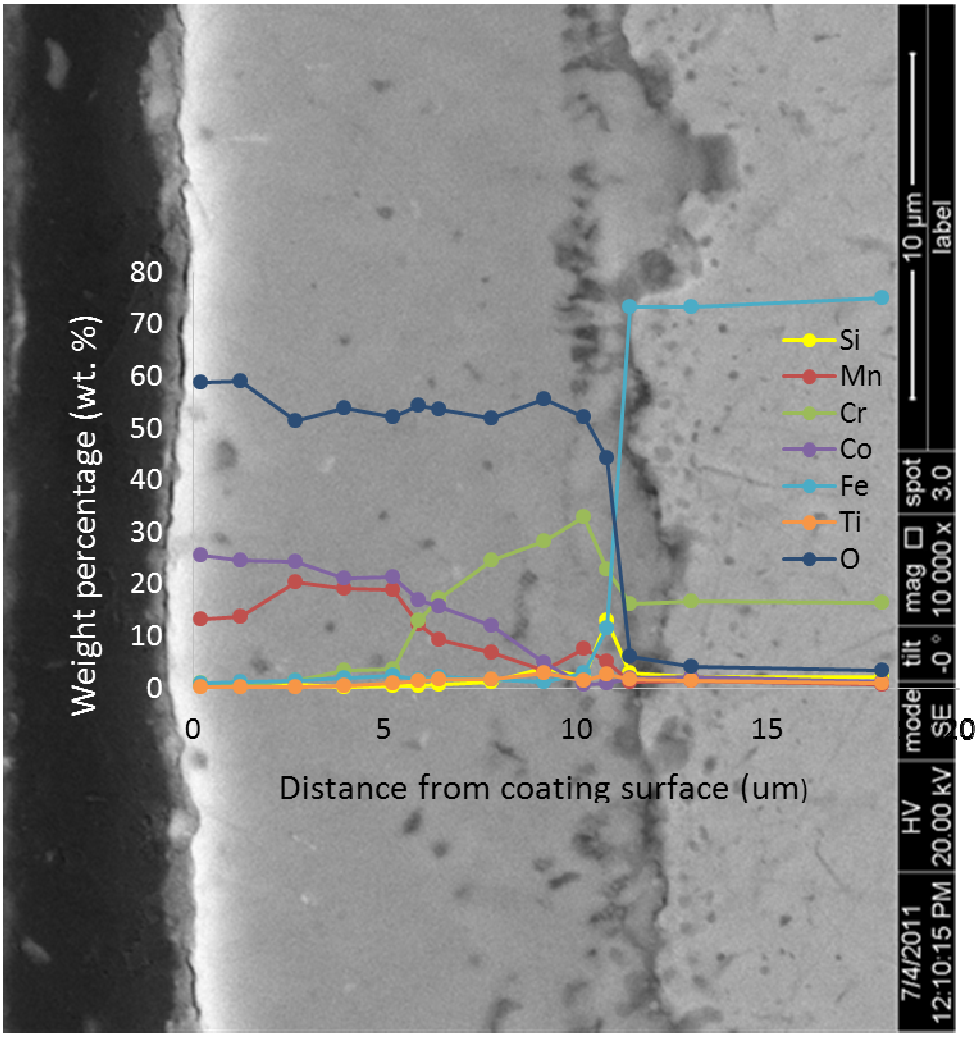

Fig. 4.35 Compositional profile of MCO as coated AISI 441

The Cr concentration is roughly 1.wt. % near the coating surface and stays low (2 wt. %~4 wt %) up to 5um from the coating surface to the coating interior. To further study the reaction between the coating and the underlying substrate, FIB was used to make a thin cross-sectional slab of the coated sample after re-oxidation. Fig. 4.36a&b show BF TEM and STEM images acquired from a FIB-cut thin cross-section through the coated sample. Fig. 4.36c is a compositional profile determined from EDS measurements obtained along the red horizontal line indicated in Fig. 4.36b. The Cr_2O_3 sub-scale was approximately 2.1

um from the line analysis. Beneath the chromia sub-scale, the Cr and Fe contents are close to the bulk alloy with Si segregation at the chromia sub-scale/alloy interface and occasional TiO_2 internal oxidation. The elemental distributions of the reaction layer were revealed more clearly in X-ray mapping experiments and a selection of these data are shown in Fig. 4.36d. X-ray maps obtained from the area indicated by the red box in Fig. 4.36b. There is a band around 3 um thick that comprises a mixture of O, Cr, Mn and Co in varying proportions, which is defined as reaction layer (RL).

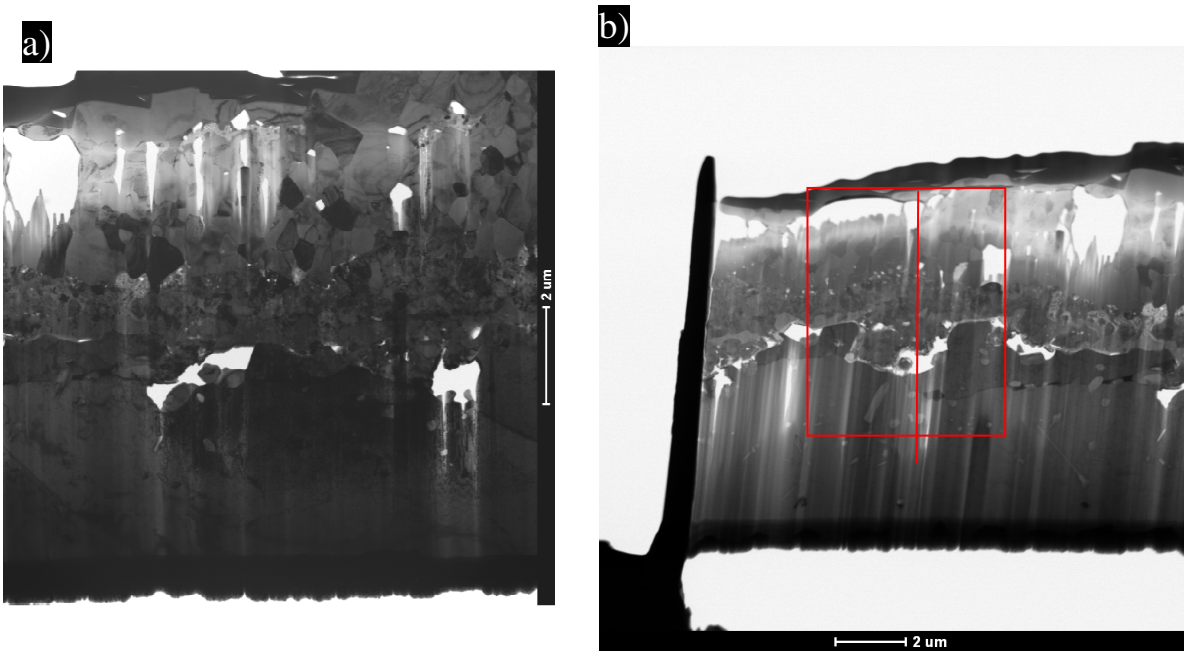

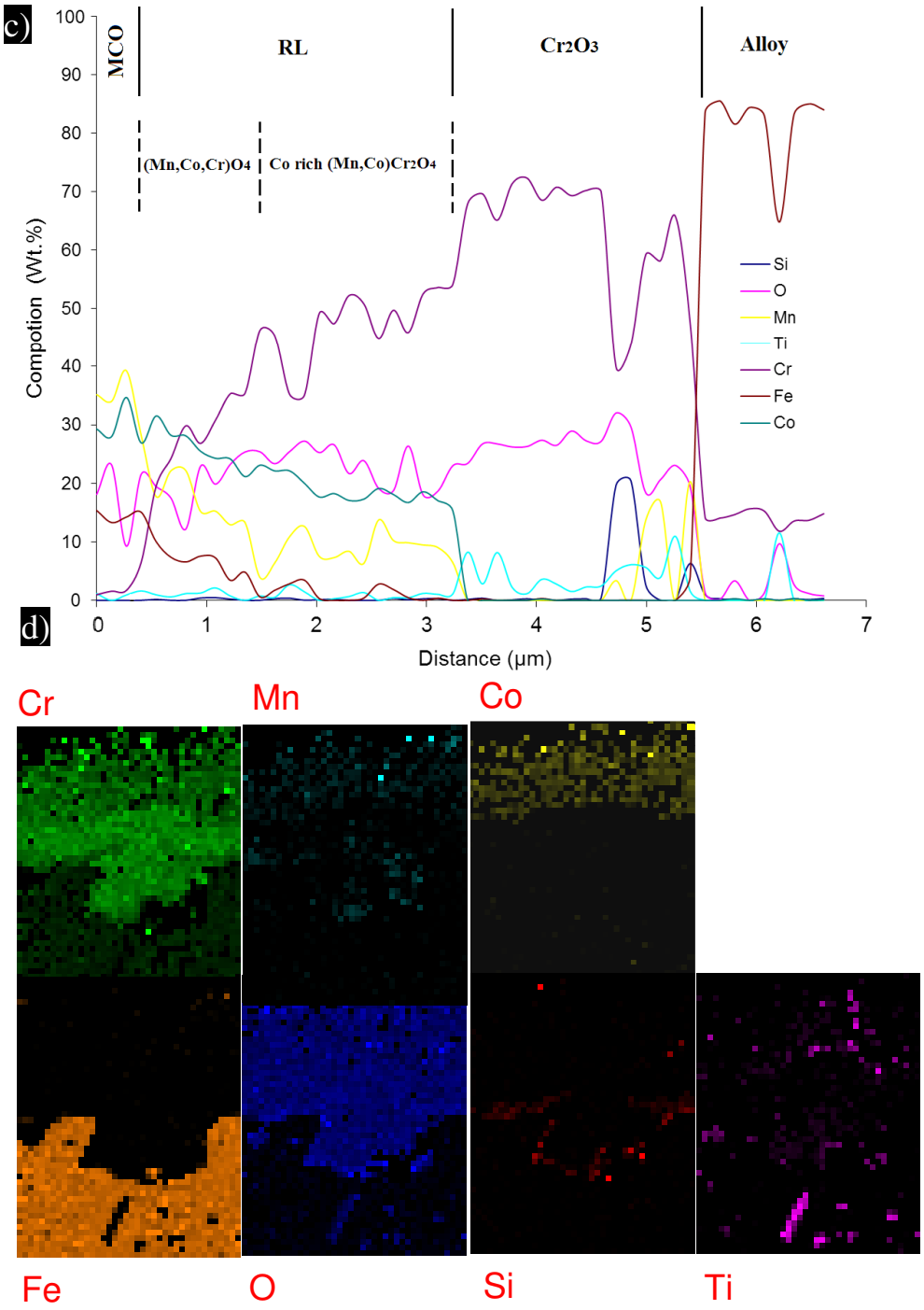

Fig. 4.36 (a) TEM image acquired from a FIB-cut thin cross-section through the sample. (b) STEM image acquired from a FIB-cut thin cross-section through the sample (c) Compositional profile obtained from spectra acquired at points along the vertical line in (b) (d) X-ray maps obtained from the area indicated by the box in (b)

There is also a small amount of Fe, Si and Ti present in the reaction layer and MCO layers, which is the result of elements diffusion from the substrate alloy. Above the reaction layer, there is a region of near constant Mn and Co content, which is MCO coating with average composition $Mn_{1.5}Cr_{1.5}O_4$, which should give roughly equal proportions of Mn_2CoO_4 and $MnCo_2O_4$ phases. The reaction layer can be further classified into two layers: a Cr-Co rich spinel layers ($(Mn,Co)Cr_2O_4$ with with Co concentration much higher than Mn) layer (close to chromia sub-scale) which grows by inward diffusion of Co toward the chromium rich layer and outward diffusion of Mn; a $(Mn,Co,Cr)_3O_4$ layer which grows by diffusion of Cr toward the cobalt rich spinel layer. Although the thicknesses of the chromia scale and the reaction layer varies with location along the interface, the structures of the four distinct layers remain the same. The Cr-Co rich spinel layer may be related to the strong tetrahedral site preference of Co^{2+} [109] or high diffusion rate of Co, relative to Mn in chromia spinels and initial high Co concentration near the chromia scale. The $(Mn,Co,Cr)_3O_4$ layer is around 2 um thick, which grows much faster than the Cr rich $(Mn,Co)Cr_2O_4$ (~1um) layer during the heat treatment. The chromium outward migration during the re-oxidation process is possible the effect of both vapor phase Cr transport, deposition and solid state diffusion. The vapor phase Cr transport is possibly the dominant Cr migration route before Co+MnO layer was re-oxidized and densified, as Cr vapor could easily transport through the open pores and re-deposit on them. Once a dense MCO was grown, the dominant Cr migration route will shift to Cr outward diffusion through MCO layer. As Cr has strong octahedral site preference [112], Cr is assumed to always occupy the octahedral site in $(Mn,Co,Cr)_3O_4$ spinel (grown by Cr outward diffusion).

4.3.2 Chromium Evaporation from coated and uncoated AISI 441

The chromium evaporation rates for MCO coated and uncoated AISI 441 at 850°C in air with humidity levels of 3% (500 h) are presented in Fig. 4.37 as total mass of vaporized chromium per unit area and time. The evaporation rate was reduced by more than two orders of magnitude for the MCO coated samples.

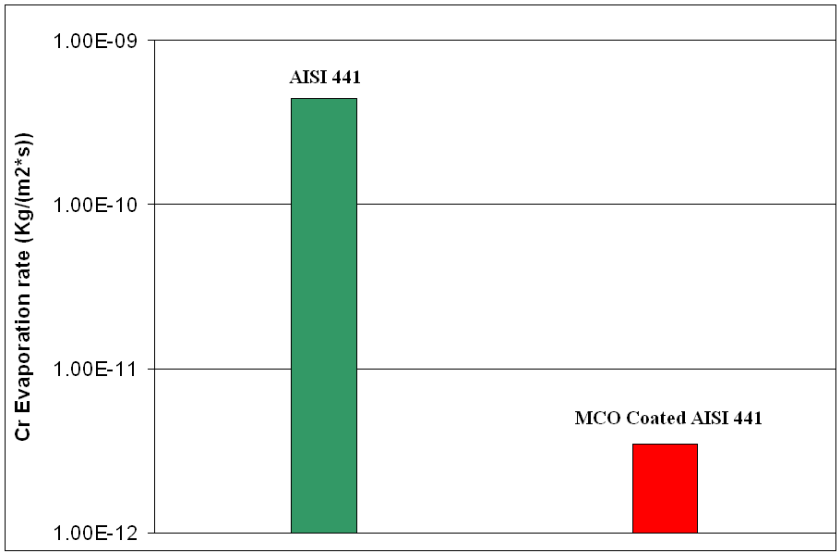

Fig. 4.37 Comparison of the measured chromium evaporation rates of coated and uncoated AISI 441

4.3.3 Evaluation of Manganese Cobalt Oxide Spinel Coated AISI 441 after 500 h Test

Similar characterizations were conducted on the MCO coated AISI 441 after 500 h exposure at 850^{o}C and 3% humidity, and the SEM images of the sample surface are shown in Fig. 4.38. The faceted surface crystals of the 500 h exposed coated sample appeared to be denser and larger than as coated samples with no pores. The edges of the sample were still covered by MCO coatings with no evidence of cracking or spallation after 500 h exposure.

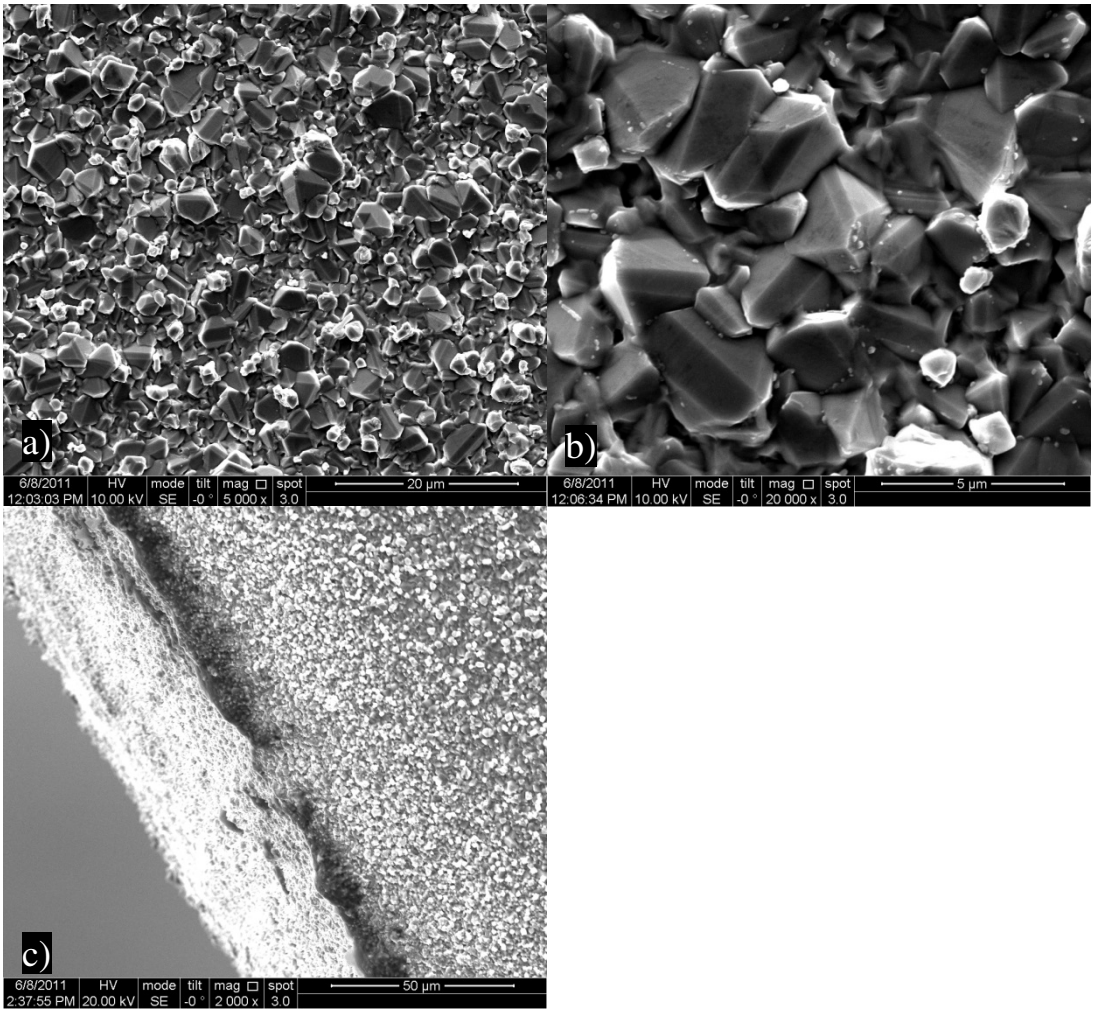

Fig. 4.38 Surface morphologies of MCO coated AISI 441 exposed to 3% humid air for 500 h at 850°C

The surface crystals present in the coating were identified to be $Mn_{1.5}Co_{1.5}O_4$, by XRD (Fig. 4.39). The cross-section images (Fig. 4.40) of the samples show the coating layer remained dense with thickness of approximately 13 um cross the surface. Fig. 4.41 shows the chemical composition profile of a 500 h exposed coated sample by EDS point analysis. The chemical composition is predominant $Mn_{1.5}Co_{1.5}O_4$ along the coating with very low concentration of Fe, Ti, and Si.

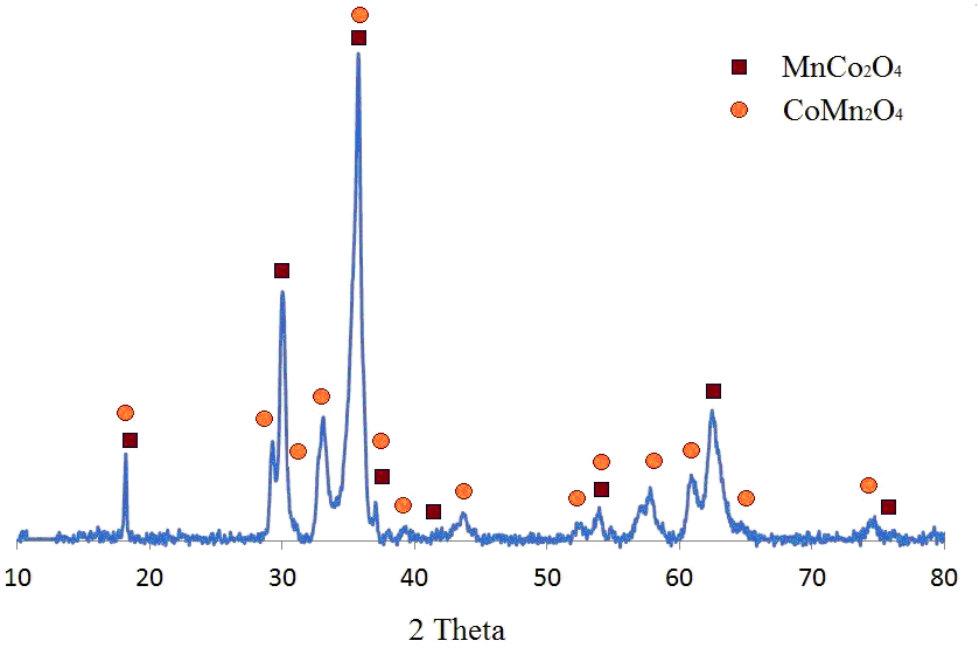

Fig. 4.39 XRD patterns of the coating on AISI 441 exposed to 3% humid air for 500 h at 850°C

The surface concentration of Cr remains roughly 1.wt. % (a slight variation could be observed) in the coating layer up to 7 um from coating surface to the coating interior, and keeps low (2.wt. %~5. wt %) up to 8um.

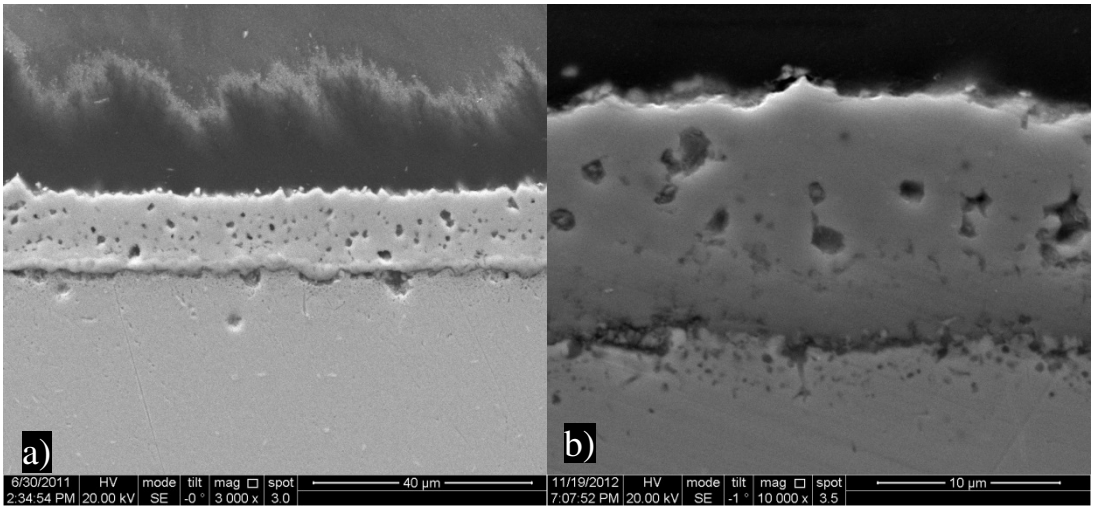

Fig.4. 40 Cross section of MCO coated AISI 441 exposed to 3% humid air for 500 h at 850°C

To study the reaction between the coating and the underlying substrate after 500 h exposure at 850°C and 3% humidity, again FIB was used to make a thin cross-sectional slab of the sample.

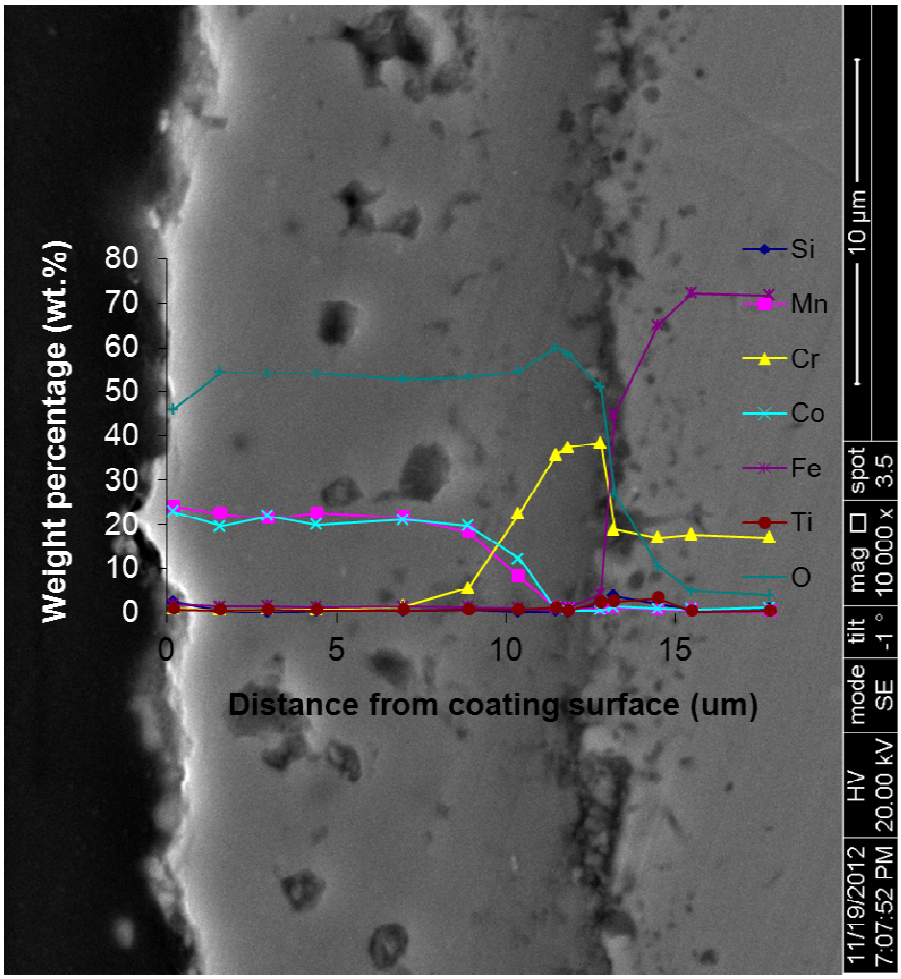

Fig. 4.41 Compositional profile of MCO coated AISI 441 exposed to 3% humid air for 500 h at 850°C

Fig. 4.42 shows BF TEM and STEM images acquired from a FIB-cut thin cross-section through the coated sample. Fig. 4.42 c is a compositional profile determined from EDXS measurements obtained along the red horizontal line indicated in Fig. 4.42 b. The Cr_2O_3 sub-scale has grown to approximately 2.5 um in average from the line analysis. The reaction layer, in this case, shrunk to ~ 2 um with both a Cr rich Cr-Co rich spinel layer (~ 0.5um) and a $(Mn,Co,Cr)_3O_4$ layer (~ 1.5um). Compared to the as coated sample after re-oxidation, the $(Mn,Co,Cr)_3O_4$ layer grew at the cost of Cr-Co spinel layer, and there is only 400nm growth of the chromia sub scale during the 500 h exposure, which means MCO spinel coating and the RL is an effective barrier for inward diffusion of oxygen the growth of the Cr rich $(Mn,Co)Cr_2O_4$ should be beneficial for reducing chromium volatilization.

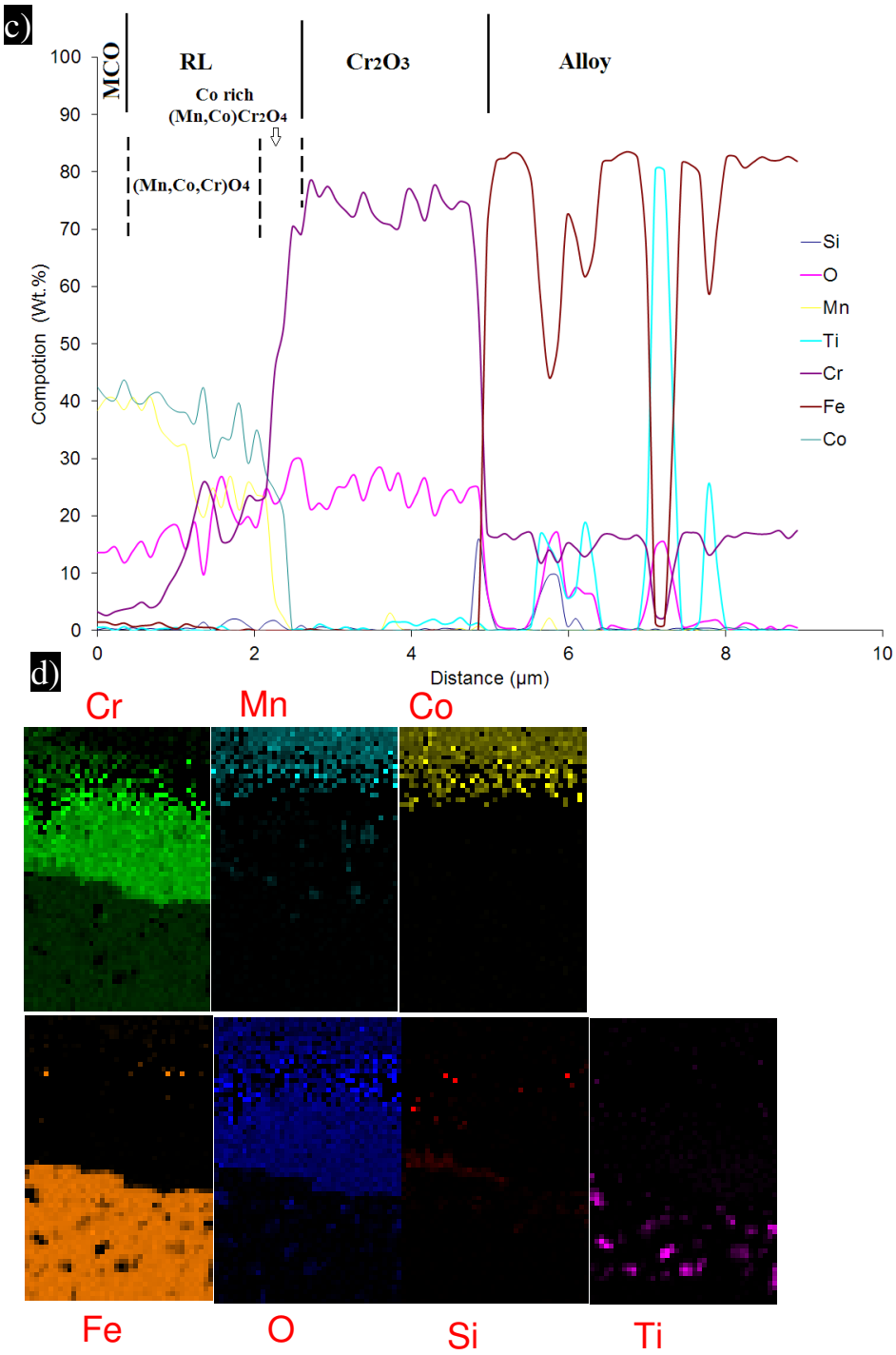

Fig. 4.42 (a) TEM image acquired from a FIB-cut thin cross-section through the sample. (b) STEM image acquired from a FIB-cut thin cross-section through the sample (c) Compositional profile obtained from spectra acquired at points along the vertical line in (b) (d) X-ray maps obtained from the area indicated by the box in (b)

The elemental distributions of the reaction layer were revealed more clearly in X-ray mapping experiments and a selection of these data are shown in Fig. 4.42 d. X-ray maps were obtained from the area indicated by the red box in Fig. 4.42 b. At the chromia sub-scale/alloy interface more Si segregation was observed. Besides TiO_2 internal oxidation, more Ti diffused into the reaction layer, likewise, more Fe was observed as well in the reaction layer. It is argued by Fergus et al. [64] that with Fe and Ti doping in the CMO coating, both Cr diffusion into the MCO coating layer and Co and Mn diffusion into the chromia sub scale were slowed, however no Ti and/or Fe was found in the Cr rich $(Mn,Co)Cr_2O_4$ layer. In the case of the MCO coated AISI 441, as no Ti and/or Fe was initial doped into the MCO, the Ti and Fe diffused from the alloy substrate. It is found that no Ti and/or Fe were present in the chromia sub-scale, most of the Ti and Fe was in the Cr rich $(Mn,Co)Cr_2O_4$ layer, and with the addition of iron or titanium, there is only less than 1 um growth of the Cr rich $(Mn,Co)Cr_2O_4$ and hardly any growth of the $(Mn,Co,Cr)_3O_4$ layer, which would reduce the risk of scale spallation and improve the long-term stability of the interconnect. The low Cr evaporation rate would be ascribed to the successful mitigation of the Cr diffusion through the reaction layer to the coating layer, hence less degradation of the cell.

4.4 Chromium Mitigation via aluminized Coating

4.4.1 Chromium Evaporation from coated and uncoated AISI 441

The chromium evaporation rates for aluminized Nicrofer6025 HT (602CA) at 850^{o}C in air with humidity levels of 3% (500 h) are presented in Fig. 4.43 as total mass of vaporized chromium per unit area and time. The evaporation rate was reduced by near two orders of magnitude for both samples coated by pack cementation and chemical vapor deposition (CVD).

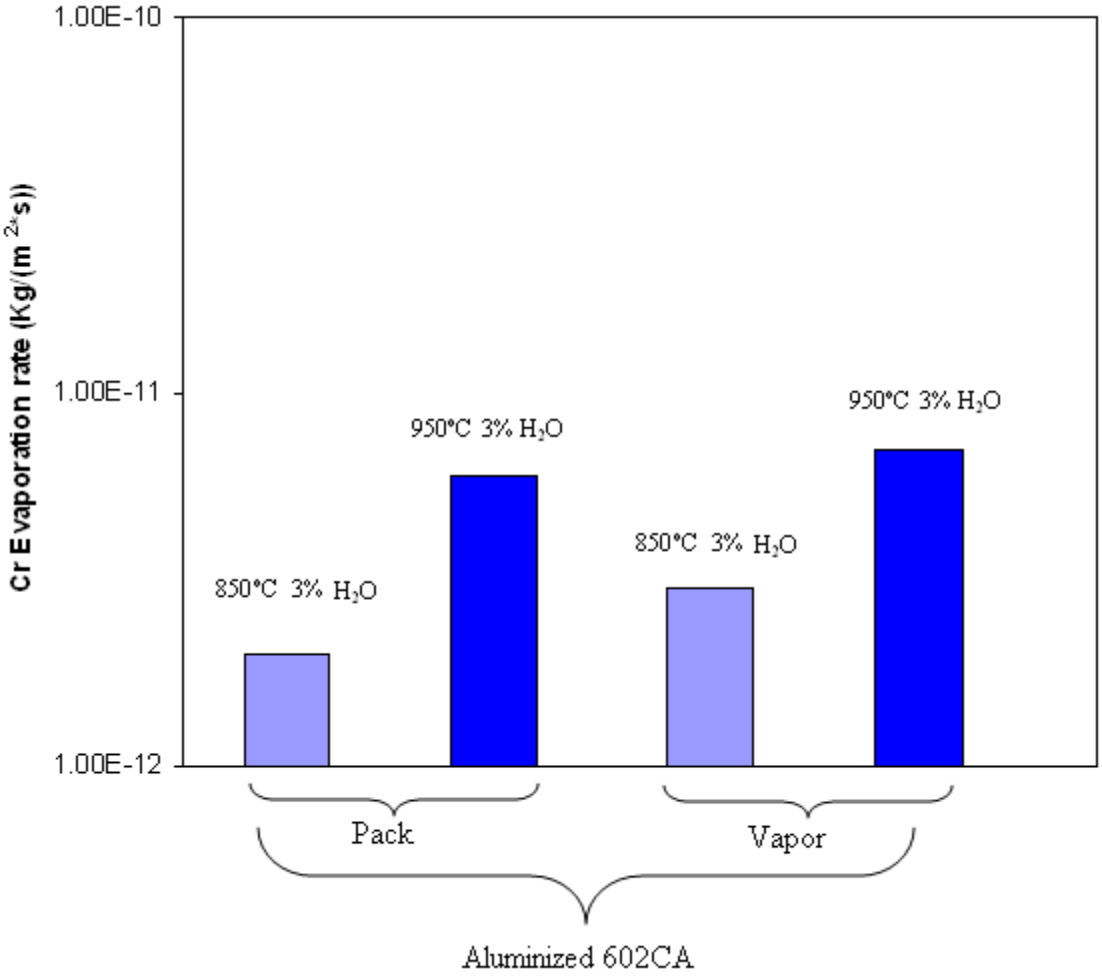

Fig. 4.43 Comparison of the measured chromium evaporation rates of aluminized Nicrofer6025 HT

4.4.2 Evaluation of Aluminized Nicrofer6025 HT

Fig. 4.44 shows SEM images of aluminized Nicrofer6025 HT sample surface (both pack and vapor coated). The aluminized coatings are rather uniform for both samples; a few localized porosities could be observed on the CVD sample surface. Surface EDS analysis of both sample showed predominant Ni and Al with only 2~3 wt % Cr.

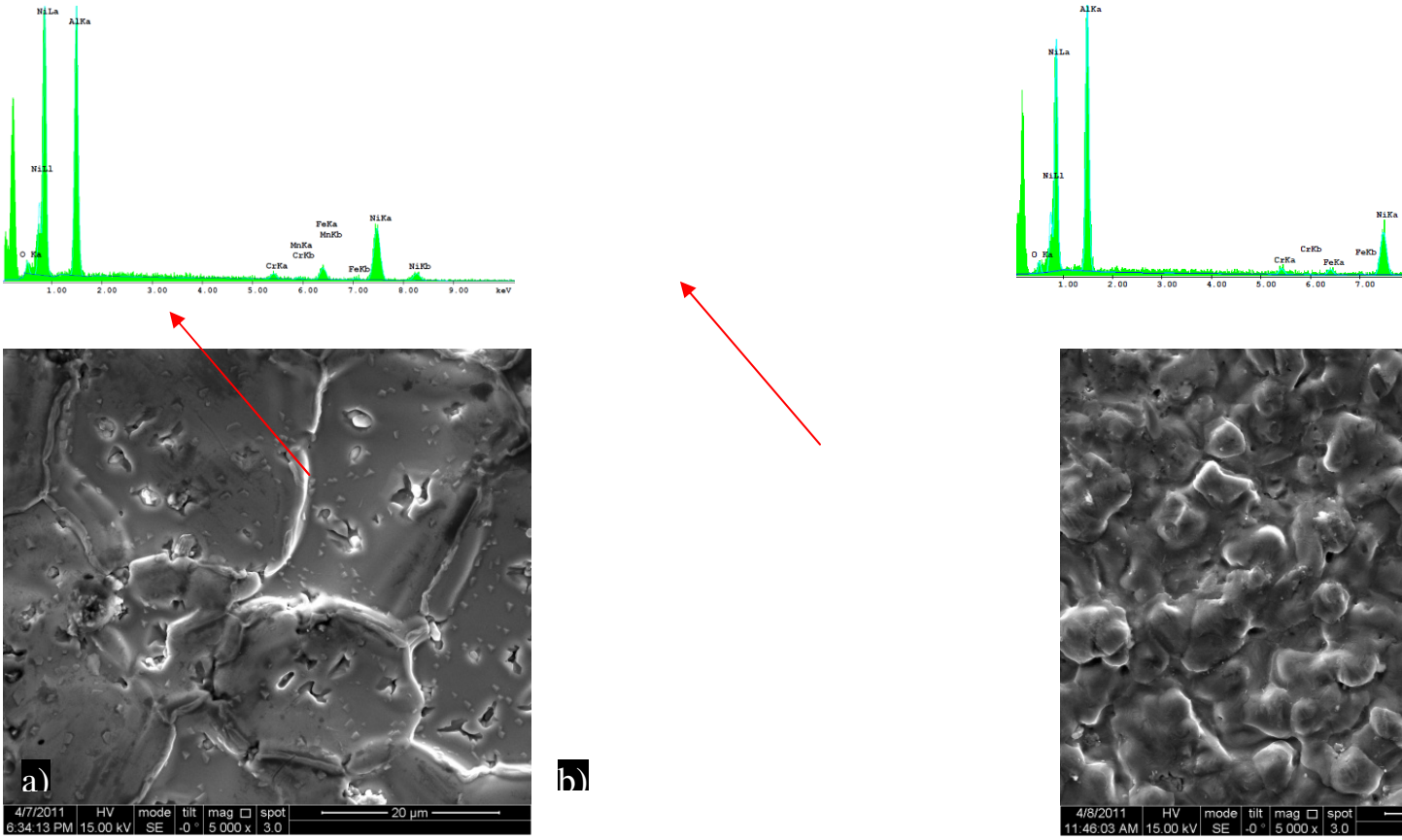

Fig. 4.44 Surface morphologies of aluminized Nicrofer6025 HT (a) CVD (b) Pack cementation

The polished cross-sections are shown in Fig. 4.45. The cross-section can be divided into three different zones: outer zone, interfacial zone, and substrate. The Cr content in the outer zone is very low (less than 3 wt%) for both samples.

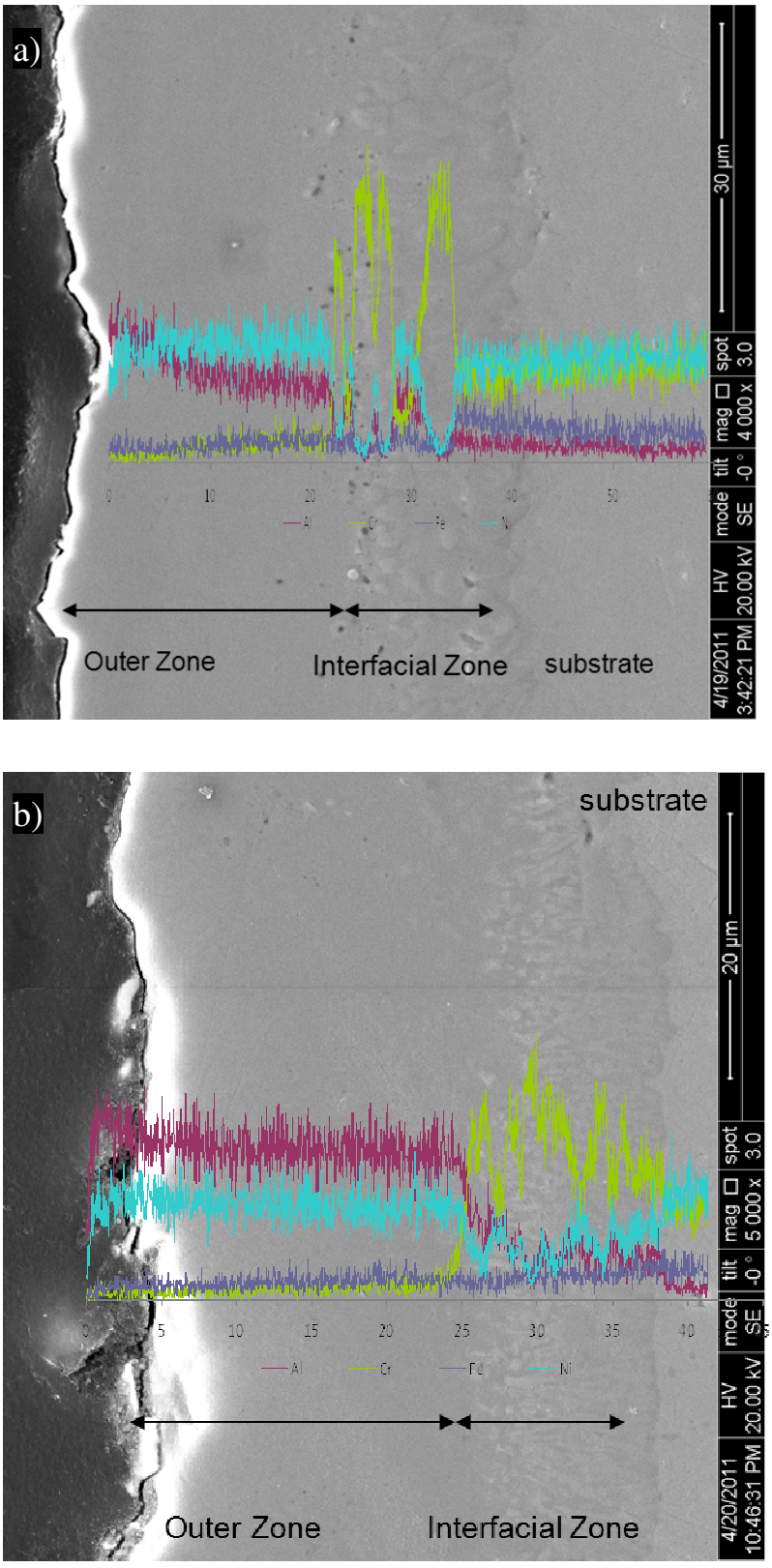

Fig. 4.45 Cross-section of aluminized Nicrofer6025 HT (a) CVD (b) Pack cementation

4.4.2 Evaluation of Aluminized Nicrofer6025 HT after 500 h Test

Fig. 4.46 & 4.47 show SEM images of vapor and pack aluminized Nicrofer6025 HT sample surface after exposure to 3% humid air for 500 h at 850^{o}C. The surface is fully covered by platelet shaped alumina which indicates the formation of transition alumina. And the cross-section images show that both samples established an external alumina scale. Similar features were observed for both samples after exposure to 3% humid air for 500 h at 950^{o}C (Fig. 4.48 & 4.49). More ridge-shaped alumina was seen at 950^{o}C compared to 850^{o}C indicating formation of stable alpha alumina formation. In addition, surface scale spallation and scale thickness variation was observed, though, a slightly thicker alumina scale (in average) was grown at 950^{o}C. The EDS analysis of the surface after the tests indicates that there is about 1~2 wt. % of Cr, which is possibly doped in the alumina scale and is lower than the initial Cr percentage before oxidation. Such low alumina concentration on the surface suggests that the Cr activity on the surface is low as well, which explains the low Cr evaporation rates observed for both samples at 850 & 950 ^{o}C. It is also postulated based on the observation that the initial oxidation of the aluminized sample might lead to higher Cr evaporation rates before the extensive alumina scale establishes. Therefore, pre-oxidation is recommended for further lowering the Cr evaporation rate, however, the pre-oxidation conditions should be examined carefully, as the proper pre-oxidation temperature and humidity level as well as the duration will affect the alumina scale developed on the surface and long term operation.

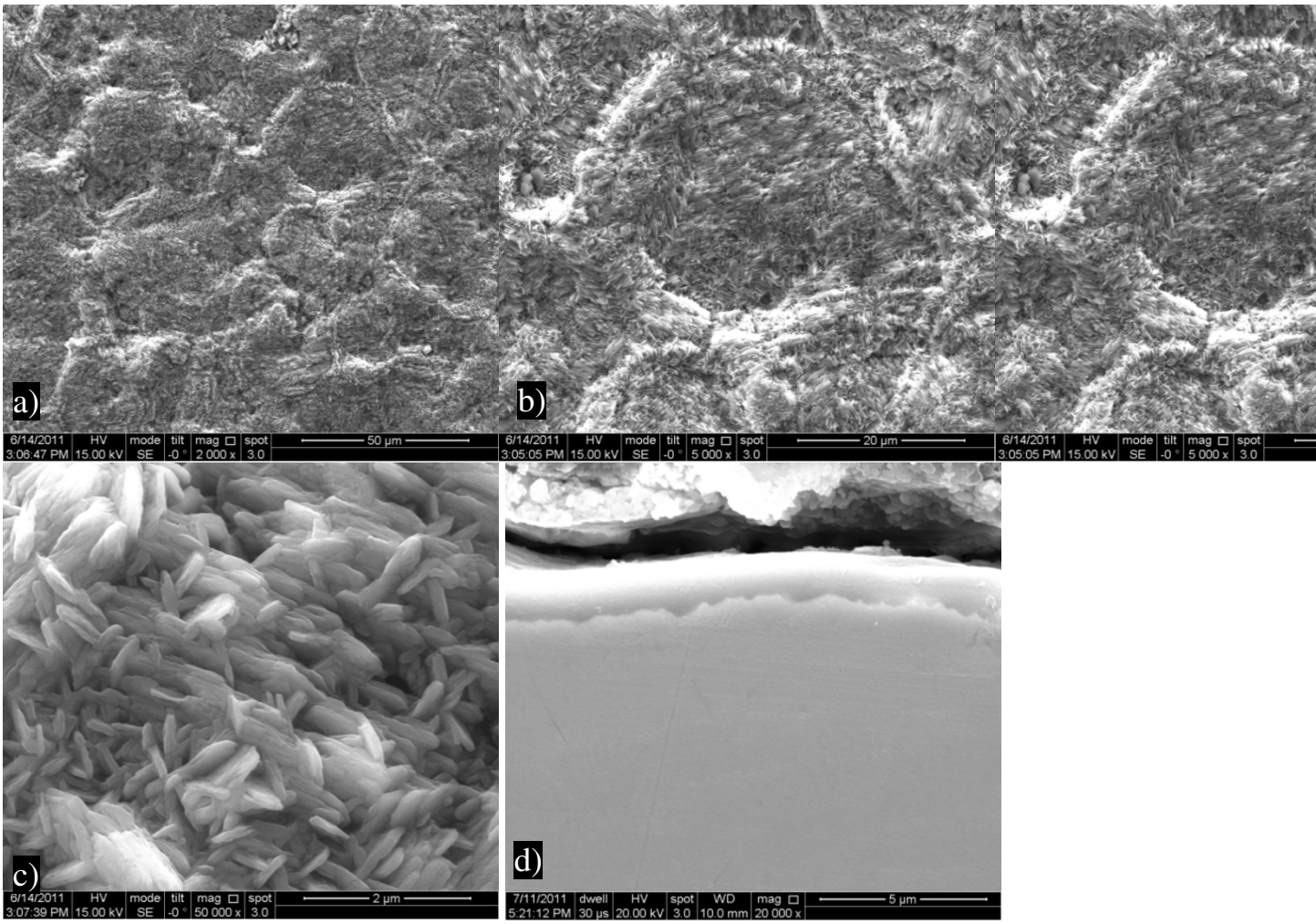

Fig. 4.46 Surface morphologies of CVD aluminized Nicrofer6025 HT a), b), c), and cross-section d) exposed to 3% humid air for 500 h at 850°C

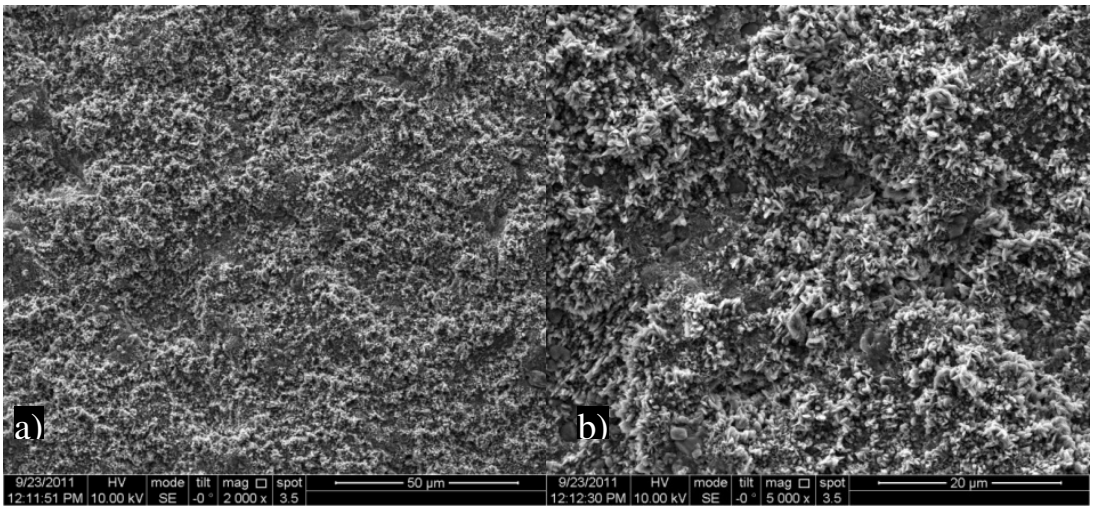

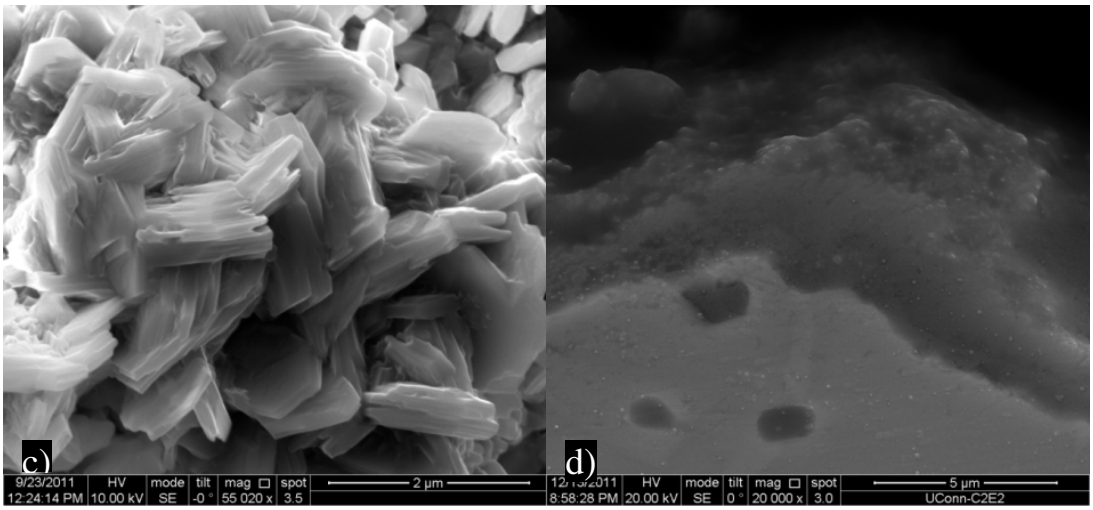

Fig. 4.47 Surface morphologies of CVD aluminized Nicrofer6025 HT a), b), c), and cross-section d) exposed to 3% humid air for 500 h at 950°C

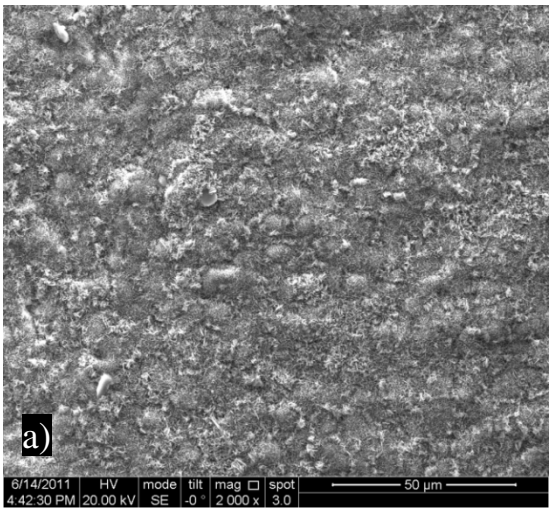

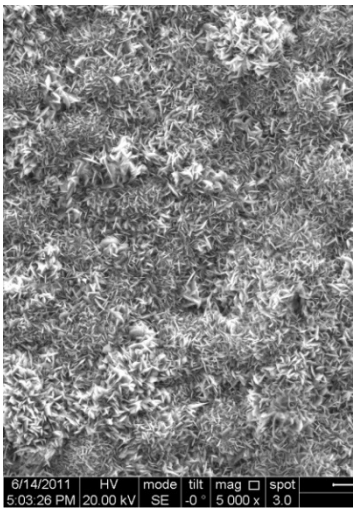

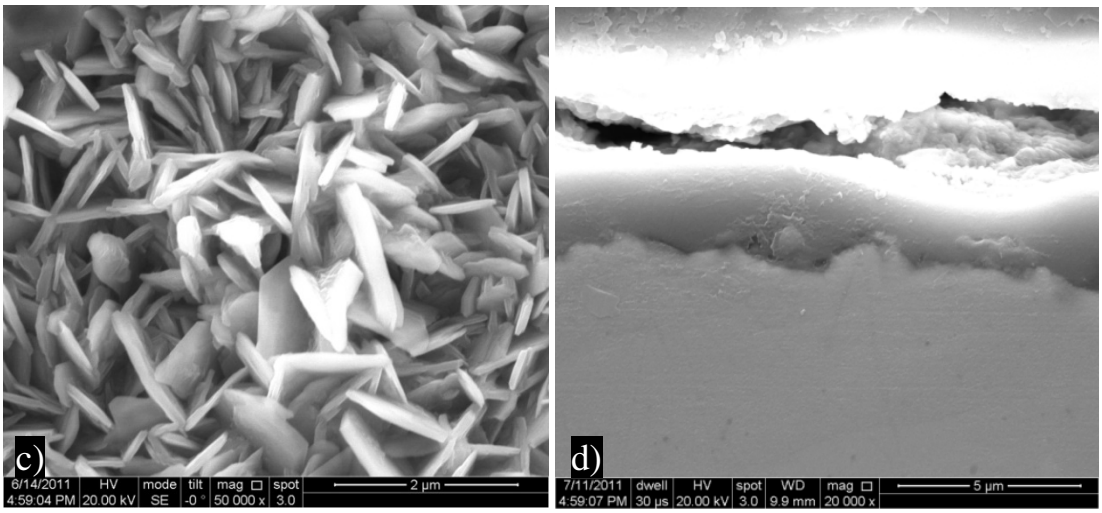

Fig. 4.48 Surface morphologies of pack aluminized Nicrofer6025 HT a), b), c), and cross-section d) exposed to 3% humid air for 500 h at 850^{o}C

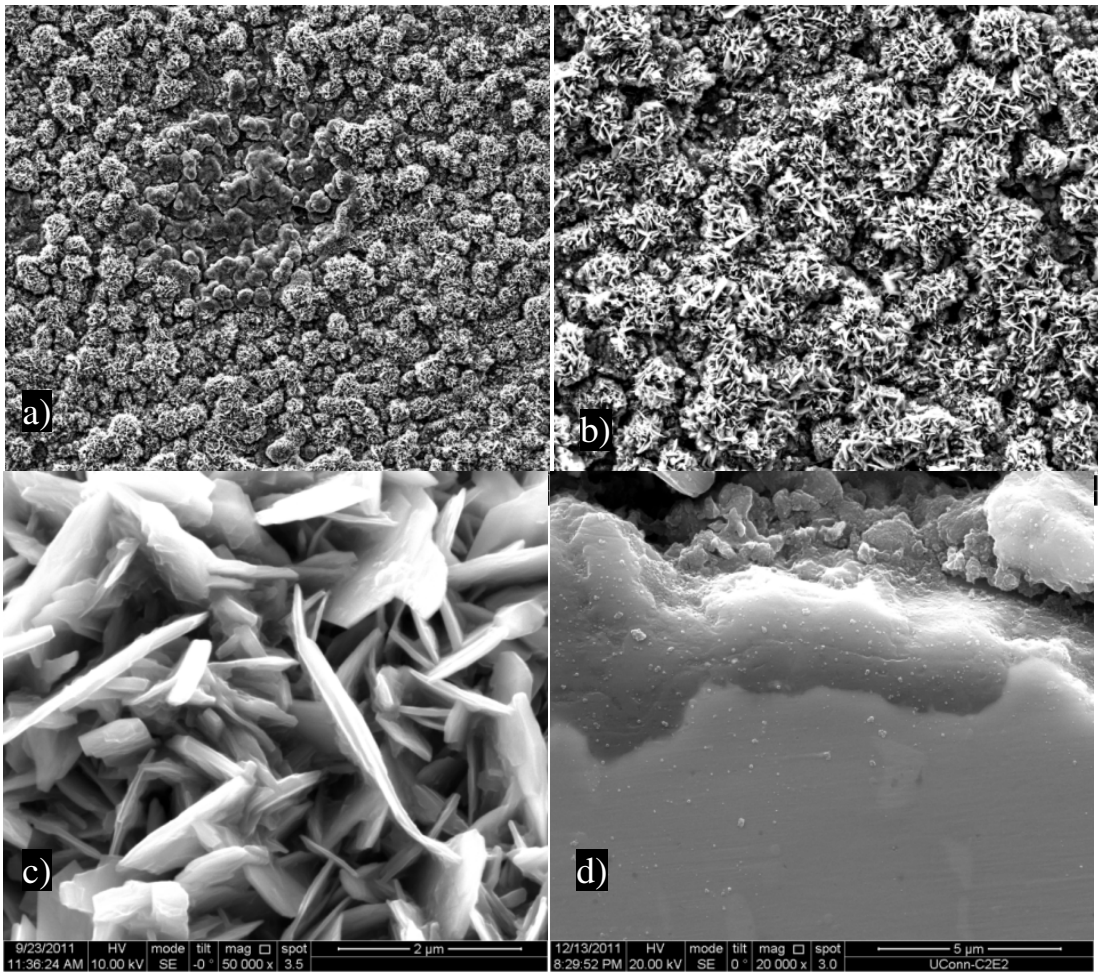

Fig. 4.49 Surface morphologies of CVD pack aluminized Nicrofer6025 HT a), b), c), and cross-section d) exposed to 3% humid air for 500 h at 950°C

Fig. 4.50 & 4.51 show XRD pattern of the CVD and pack aluminized Nicrofer6025 HT sample after exposure to 3% humid air for 500 h at 850°C. The alumina scale formed on the surface is confirmed to be gamma alumina.

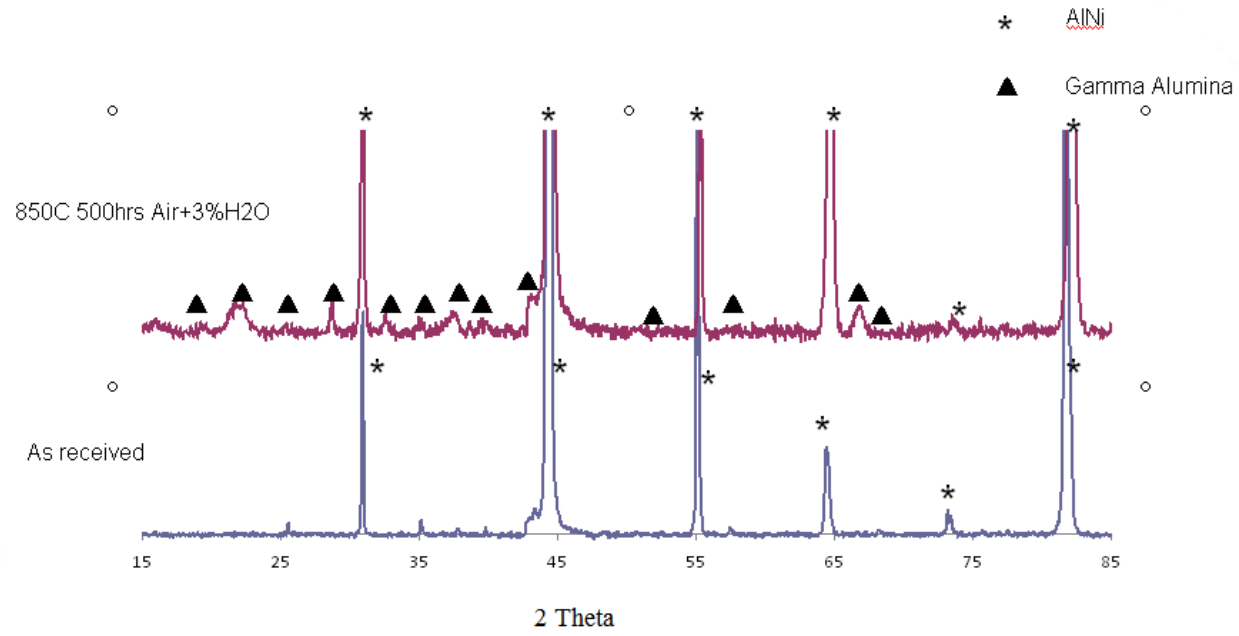

Fig. 4.50 Comparison of XRD patterns of the CVD aluminized Nicrofer6025 HT as received and exposed to 3% humid air for 500 h at 850°C

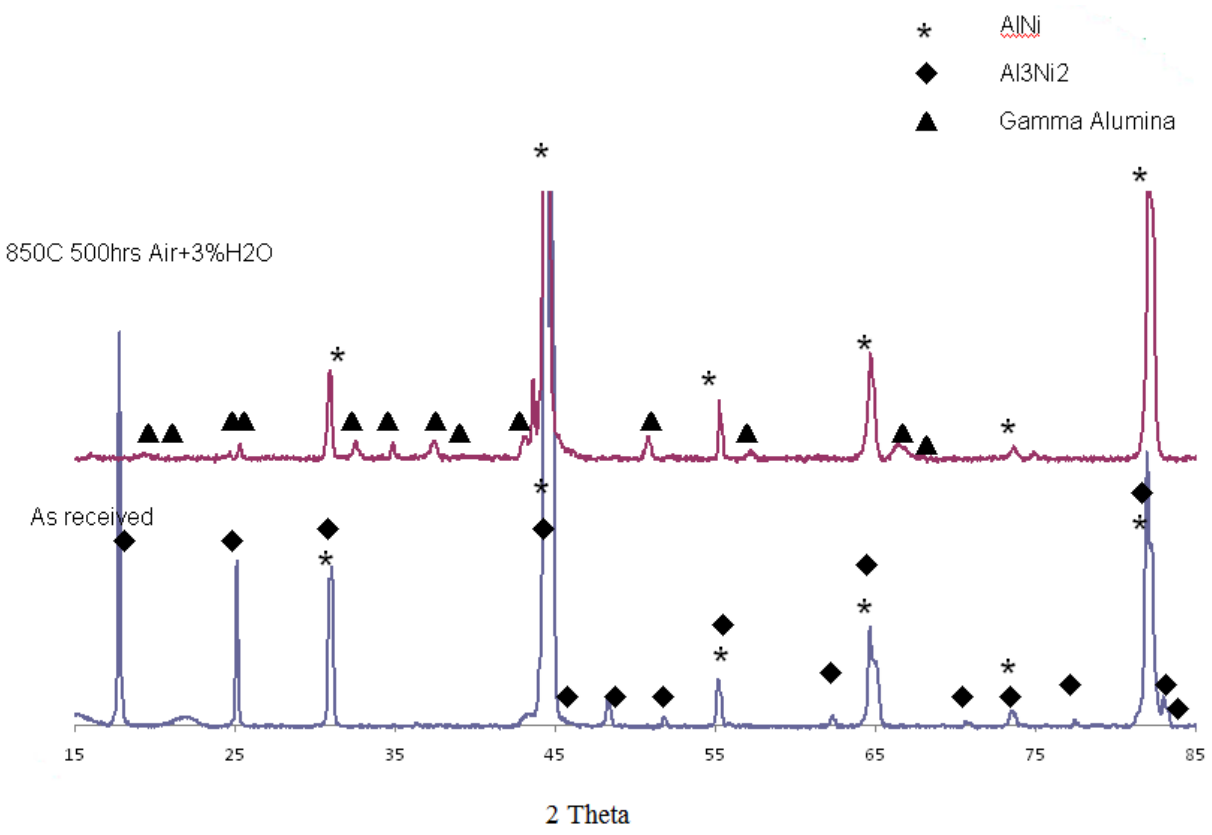

Fig. 4.51 Comparison of XRD patterns of the pack aluminized Nicrofer6025 HT as received and exposed to 3% humid air for 500 h at 850°C

The low Cr evaporation rate would be ascribed to the successful mitigation of the Cr diffusion through the reaction layer to the coating layer, hence less degradation of the cell.

CHAPTER 5
CONCLUSIONS

The chromium evaporation rates were measured for chromia and alumina forming nickel- and iron- base alloys in 3 and 12% humid air using the transpiration method. The chromium evaporation rates have been correlated with the composition and morphology of surface scale that develop at different temperatures and humidity levels. The chromium release is governed by the morphology and chemical composition of scale. The lowest chromium evaporation rates were detected for Aluchrom alloy that develops a continuous and dense aluminum oxide scale, whereas the chromium evaporation rates were an order of magnitude higher for Nicrofer6025 HT that does not quickly develop an inner layer of aluminum oxide, thereby allowing considerable chromium evaporation (before the aluminum oxide layer develops). The chromium evaporation rates were in excess of an order of magnitude lower for AFA alloy which develops a continuous two layered oxide scale with an outer layer of Cr containing mixed oxide and an undercutting pure alumina layer underneath. AISI 310S that develops a surface scale comprised of a non-continuous outer layer of $(Cr,Mn)_3O_4$ followed by an inner chromia scale, showed highest chromium evaporation rates among the three alloys tested. The alloy also showed scale cracking and spallation that contributed to the enhanced chromium evaporation particularly in air with high humidity (12%).

Chromium evaporation rates were measured for MCO coated and uncoated AISI 441 for 500 h exposure at 850^{o}C and 3% humidity using the transpiration method. The chromium evaporation rates have been correlated with the composition and morphology of the scales that develop on the bare alloy surface and also the interaction between manganese cobalt spinel oxides and the substrate alloy. More than 2 orders of magnitude reduction in chromium evaporation rate was detected for MCO coated AISI 441. The reaction layer that grows by diffusion of manganese and cobalt toward the chromia should be beneficial for reducing chromium volatilization. Diffusion of Ti and Fe from the alloy to the reaction layer may cause growth of the $(Mn,Co,Cr)_3O_4$ layer, which would also mitigate the outward diffusion of chromium and hence the chromium volatilization.

Chromium evaporation rates were measured for both vapor and pack aluminized Nicrofer6025 HT, more than one order of magnitude reduction of chromium evaporation rate is achieved. The establishment of

extensive external alumina scale caused mitigation of the Cr outward diffusion, hence, lowered the Cr evaporations rates.

REFERENCES

[1] L. Blum, Cfi-Ceramic Forum International 86 (2009) E17-E22.
[2] S. Farhad, F. Hamdullahpur, Journal of Power Sources 193 (2009) 632-638.
[3] T.A. Adams, P.I. Barton, Aiche Journal 56 (2010) 3120-3136.
[4] Y. Hao, D.G. Goodwin, Journal of Power Sources 183 (2008) 157-163.
[5] P. Kazempoor, V. Dorer, F. Ommi, International Journal of Hydrogen Energy 34 (2009) 8630-8644.
[6] K. Lobachyov, H.J. Richter, Journal of Energy Resources Technology-Transactions of the Asme 118 (1996) 285-292.
[7] S.P. Jiang, J.P. Zhang, X.G. Zheng, Journal of the European Ceramic Society 22 (2002) 361-373.
[8] H. Yokokawa, T. Horita, N. Sakai, K. Yamaji, M.E. Brito, Y.P. Xiong, H. Kishimoto, Solid State Ionics 177 (2006) 3193-3198.
[9] K. Hilpert, D. Das, M. Miller, D.H. Peck, R. Weiss, Journal of the Electrochemical Society 143 (1996).
[10] M. Stanislowski, E. Wessel, T. Markus, L. Singheiser, W.J. Quadakkers, Solid State Ionics 179 (2008) 2406-2415.
[11] M. Stanislowski, E. Wessel, K. Hilpert, T. Markus, L. Singheiser, Journal of the Electrochemical Society 154 (2007) A295-A306.
[12] G.R. Holcomb, D.E. Alman, Journal of Materials Engineering and Performance 15 (2006).
[13] K. Gerdes, C. Johnson, Journal of Fuel Cell Science and Technology 6 (2009) 5.
[14] R. Trebbels, T. Markus, L. Singheiser, Journal of Fuel Cell Science and Technology 7 (2010) 6.
[15] X. Sun, W.N. Liu, E. Stephens, M.A. Khaleel, Journal of Power Sources 176 (2008) 167-174.
[16] M. Stanislowski, J. Froitzheim, L. Niewolak, W.J. Quadakkers, K. Hilpert, T. Markus, L. Singheiser, Journal of Power Sources 164 (2007) 578-589.
[17] J.W. Fergus, Materials Science and Engineering a-Structural Materials Properties Microstructure and Processing 397 (2005) 271-283.
[18] W.N. Liu, X. Sun, M.A. Khaleel, Fuel Cells 10 (2010) 703-717.
[19] V. Miguel-Perez, A. Martinez-Amesti, M. Luisa No, A. Larranaga, M. Isabel Arriortua, Corrosion Science 60 (2012) 38-49.
[20] T. Brylewski, M. Nanko, T. Maruyama, K. Przybylski, Solid State Ionics 143 (2001) 131-150.
[21] T. Horita, Y. Xiong, K. Yamaji, N. Sakai, H. Yokokawa, Journal of the Electrochemical Society 150 (2003) A243-A248.
[22] S. Linderoth, P.V. Hendriksen, M. Mogensen, N. Langvad, Journal of Materials Science 31 (1996) 5077-5082.
[23] P.D. Jablonski, C.J. Cowen, J.S. Sears, Journal of Power Sources 195 (2010).
[24] N. Shaigan, W. Qu, D.G. Ivey, W. Chen, Journal of Power Sources 195 (2010).
[25] Z.G. Yang, K.S. Weil, D.M. Paxton, J.W. Stevenson, Journal of the Electrochemical Society 150 (2003).
[26] W.Z. Zhu, S.C. Deevi, Materials Science and Engineering a-Structural Materials Properties Microstructure and Processing 348 (2003).
[27] Fuel Cell Handbook, 2004.
[28] S. Fontana, R. Amendola, S. Chevalier, P. Piccardo, G. Caboche, M. Viviani, R. Molins, M. Sennour, Journal of Power Sources 171 (2007) 652-662.
[29] S. Fontana, S. Chevalier, G. Caboche, Materials and Corrosion-Werkstoffe Und Korrosion 62 (2011) 650-658.
[30] P. Piccardo, P. Gannon, S. Chevalier, M. Viviani, A. Barbucci, G. Caboche, R. Amendola, S. Fontana, Surface & Coatings Technology 202 (2007) 1221-1225.
[31] S.-S. Pyo, S.-B. Lee, T.-H. Lim, R.-H. Song, D.-R. Shin, S.-H. Hyun, Y.-S. Yoo, International Journal of Hydrogen Energy 36 (2011) 1868-1881.
[32] W. Zhang, J. Pu, B. Chi, L. Jian, Journal of Power Sources 196 (2011) 5591-5594.

[33] X. Chen, P.Y. Hou, C.P. Jacobson, S.J. Visco, L.C. De Jonghe, Solid State Ionics 176 (2005).
[34] C. Collins, J. Lucas, T.L. Buchanan, M. Kopczyk, A. Kayani, P.E. Gannon, M.C. Deibert, R.J. Smith, D.S. Choi, V.I. Gorokhovsky, Surface & Coatings Technology 201 (2006).
[35] X. Montero, F. Tietz, D. Sebold, H.R. Buchkremer, A. Ringuede, M. Cassir, A. Laresgoiti, I. Villarreal, Journal of Power Sources 184 (2008).
[36] Z. Yang, G.-G. Xia, X.-H. Li, J.W. Stevenson, International Journal of Hydrogen Energy 32 (2007).
[37] Z.G. Yang, G.G. Xia, J.W. Stevenson, Electrochemical and Solid State Letters 8 (2005).
[38] S. Kakac, A. Pramuanjaroenkij, X.Y. Zhou, International Journal of Hydrogen Energy 32 (2007) 761-786.
[39] P. Aguiar, C.S. Adjiman, N.P. Brandon, Journal of Power Sources 147 (2005) 136-147.
[40] S.P.S. Badwal, F.T. Ciacchi, D. Milosevic, Solid State Ionics 136 (2000) 91-99.
[41] D.J.L. Brett, A. Atkinson, N.P. Brandon, S.J. Skinner, Chemical Society Reviews 37 (2008) 1568-1578.
[42] K. Choy, W. Bai, S. Clarojrochkul, B.C.H. Steele, Journal of Power Sources 71 (1998) 361-369.
[43] E. Fabbri, A. D'Epifanio, E. Di Bartolomeo, S. Licoccia, E. Traversa, Solid State Ionics 179 (2008) 558-564.
[44] T. Ishihara, M. Honda, T. Shibayama, H. Minami, H. Nishiguchi, Y. Takita, Journal of the Electrochemical Society 145 (1998) 3177-3183.
[45] N. Ito, M. Iijima, K. Kimura, S. Iguchi, Journal of Power Sources 152 (2005) 200-203.
[46] S.D. Kim, S.H. Hyun, J. Moon, J.H. Kim, R.H. Song, Journal of Power Sources 139 (2005) 67-72.
[47] J.S. Ahn, D. Pergolesi, M.A. Camaratta, H. Yoon, B.W. Lee, K.T. Lee, D.W. Jung, E. Traversa, E.D. Wachsman, Electrochemistry Communications 11 (2009) 1504-1507.
[48] M. Sahibzada, B.C.H. Steele, K. Zheng, R.A. Rudkin, I.S. Metcalfe, Catalysis Today 38 (1997) 459-466.
[49] A.F. Sammells, R.L. Cook, J.H. White, J.J. Osborne, R.C. Macduff, Solid State Ionics 52 (1992) 111-123.
[50] A. Tarancon, S.J. Skinner, R.J. Chater, F. Hernandez-Ramirez, J.A. Kilner, Journal of Materials Chemistry 17 (2007) 3175-3181.
[51] E.D. Wachsman, K.T. Lee, Science 334 (2011) 935-939.
[52] E. Gourba, A. Ringuede, M. Cassir, A. Billard, J. Paiviasaari, J. Niinisto, M. Putkonen, L. Niinisto, Ionics 9 (2003) 15-20.
[53] J. Will, A. Mitterdorfer, C. Kleinlogel, D. Perednis, L.J. Gauckler, Solid State Ionics 131 (2000) 79-96.
[54] S.C. Singhal, K. Kendall, High Temperature Solid Oxide Fuel Cells, Fundamentals,Design, and Application, Elsevier, Oxford, UK, 2003.
[55] V.V. Kharton, F.M.B. Marques, A. Atkinson, Solid State Ionics 174 (2004) 135-149.
[56] R.M. Ormerod, Chemical Society Reviews 32 (2003) 17-28.
[57] S.B. Adler, Chemical Reviews 104 (2004) 4791-4843.
[58] J.W. Fergus, Solid State Ionics 171 (2004) 1-15.
[59] N.Q. Minh, T. Takahashi, Science and Technology of Ceramic Fuel Cells, Elsevier Science B. V, The Netherlands 1995.
[60] A. McEvoy, Anode, High Temperature Solid Oxide Fuel Cells: Fundamentals, Design, and Applications., Elsevier, Oxford, UK, 2003, pp. 140–171.
[61] L. Cooper, S. Benhaddad, A. Wood, D.G. Ivey, Journal of Power Sources 184 (2008) 220-228.
[62] P. Piccardo, S. Chevalier, R. Molins, M. Viviani, G. Caboche, A. Barbucci, M. Sennour, R. Amendola, Surface & Coatings Technology 201 (2006) 4471-4475.
[63] H. Ebrahimifar, M. Zandrahimi, Surface & Coatings Technology 206 (2011) 75-81.

[64] K.L. Wang, Y.J. Liu, J.W. Fergus, Journal of the American Ceramic Society 94 (2011) 4490-4495.
[65] N. Birks, G.H. Meier, F.S. Pettit, Introduction to High Temperature Oxidation of Alloys, Cambridge, New York, 2007.
[66] D. Young, High Temperature Oxidation and Corrosion of Metals, Elsevier, Oxford, UK, 2008.
[67] J. Beddoes, J.G. Parr, Introduction to Stainless Steels, ASM International, 1999.
[68] J.R. Davis, Alloy Digest Sourcebook: Stainless Steels, ASM International, 2000.
[69] C.T. Sims, N.S. Stoloff, W.C. Hagel, Superalloys II, Wiley, 1987.
[70] C. Wagner, Zeitschrift für Physikalische Chemie B 21 (1933 42).
[71] P. Kofstad, High temperature corrosion, Elsevier Applied Science London and New York, 1988.
[72] N. Jacobson, D. Myers, E. Opila, E. Copland, Journal of Physics and Chemistry of Solids 66 (2005) 471-478.
[73] S. Deflora, M. Bagnasco, D. Serra, P. Zanacchi, Mutation Research 238 (1990) 99-172.
[74] D. Carter, J. Mawdsley, J. Kropf, V. Maroni, V. Sharma, B. Yildiz, Workshop on the Stack Degradation, Fuel Cell Seminar, Phoenix, AZ, 2008.
[75] H. Asteman, J.E. Svensson, L.G. Johansson, M. Norell, Oxidation of Metals 52 (1999) 95-111.
[76] A. Yamauchi, K. Kurokawa, H. Takahashi, Oxidation of Metals 59 (2003) 517-527.
[77] J.R. O'Leary, R.G. Kunz, T.R. von Alten, Environmental Progress 23 (2004) 194-205.
[78] J. Bailey, Journal of the Electrochemical Society 144 (1997) 3568-3571.
[79] E.J. Opila, D.L. Myers, N.S. Jacobson, I.M.B. Nielsen, D.F. Johnson, J.K. Olminsky, M.D. Allendorf, Journal of Physical Chemistry A 111 (2007).
[80] B.B. Ebbinghaus, Combustion and Flame 93 (1993).
[81] C. Gindorf, L. Singheiser, K. Hilpert, Steel Research 72 (2001) 528-533.
[82] Y.W. Kim, G.R. Belton, Metallurgical Transactions 5 (1974) 1811-1816.
[83] C. Gindorf, L. Singheiser, K. Hilpert, Journal of Physics and Chemistry of Solids 66 (2005) 384-387.
[84] A. D., in: N.B. Le, V. B. (Eds.), Experimental Thermodynamics, vol II, Butterworths, London, 1975, p. 607.
[85] V. S, Measurement of the thermodynamic properties of multiple phases, Elsevier, 2005.
[86] M. U., B.W. E., The Transpiration Method, in: M.J. L. (Ed.) In The Characterization of High Temperature Vapors, John Wiley & Sons, Inc., New York, 1967, p. 91.
[87] W. Huang, S. Gopalan, U.B. Pal, S.N. Basu, Journal of the Electrochemical Society 155 (2008).
[88] N.J. Magdefrau, L. Chen, E.Y. Sun, J. Yamanis, M. Aindow, Journal of Power Sources 227 (2013) 318-326.
[89] J.A. Schuler, A.J. Schuler, D. Penner, A. Hessler-Wyser, C. Ludwig, J. Van Herle, Electrochemical and Solid State Letters 14 (2011) B132-B134.
[90] O. Thomann, M. Pihlatie, J.A. Schuler, O. Himanen, J. Kiviaho, Electrochemical and Solid State Letters 15 (2012) B35-B37.
[91] N. Sakai, H. Yokokawa, T. Horita, K. Yamaji, International Journal of Applied Ceramic Technology 1 (2004) 23-30.
[92] Z. Yang, G.-G. Xia, G.D. Maupin, J.W. Stevenson, Surface & Coatings Technology 201 (2006).

[93] R.T. Grimley, M.G. Inghram, R.P. Burns, Journal of Chemical Physics 34 (1961).
[94] N. Machkova, A. Zwetanova, V. Kozhukharov, S. Raicheva, Journal of the University of Chemical Technology and Metallurgy, 43 (2008) 53-58.
[95] J.R. Regina, J.N. DuPont, A.R. Marder, Oxidation of Metals 61 (2004) 69-90.
[96] G. Berthome, E. N'Dah, Y. Wouters, A. Galerie, Materials and Corrosion-Werkstoffe Und Korrosion 56 (2005) 389-392.
[97] J.A. Nychka, D.R. Clarke, Oxidation of Metals 63 (2005) 325-352.
[98] M.P. Brady, Y. Yamamoto, M.L. Santella, P.J. Maziasz, B.A. Pint, C.T. Liu, Z.P. Lu, H. Bei, Jom 60 (2008) 12-18.
[99] Y. Yamamoto, M.P. Brady, Z.P. Lu, P.J. Maziasz, C.T. Liu, B.A. Pint, K.L. More, H.M. Meyer, E.A. Payzant, Science 316 (2007) 433-436.
[100] Y. Yamamoto, M.P. Brady, Z.P. Lu, C.T. Liu, M. Takeyama, P.J. Maziasz, B.A. Pint, Metallurgical and Materials Transactions a-Physical Metallurgy and Materials Science 38A (2007) 2737-2746.
[101] M.P. Brady, Y. Yamamoto, M.L. Santella, B.A. Pint, Scripta Materialia 57 (2007) 1117-1120.
[102] Y. Yamamoto, A. Takeyama, Z.P. Lu, C.T. Liu, N.D. Evans, P.J. Maziasz, M.P. Brady, Intermetallics 16 (2008) 453-462.
[103] Y. Yamamoto, M.L. Santella, M.P. Brady, H. Bei, P.J. Maziasz, Metallurgical and Materials Transactions a-Physical Metallurgy and Materials Science 40A (2009) 1868-1880.
[104] Y. Yamamoto, M.L. Santella, C.T. Liu, N.D. Evans, P.J. Maziasz, M.P. Brady, Materials Science and Engineering a-Structural Materials Properties Microstructure and Processing 524 (2009) 176-185.
[105] M.P. Brady, Y. Yamamoto, M.L. Santella, L.R. Walker, Oxidation of Metals 72 (2009) 311-333.
[106] H. Bei, Y. Yamamoto, M.P. Brady, M.L. Santella, Materials Science and Engineering a-Structural Materials Properties Microstructure and Processing 527 (2010) 2079-2086.
[107] J.A. Robertson, R.A. Rapp, TAIME 239 (1967).
[108] J. Robertson, Corrosion Science 32 (1991).
[109] I.G. Wright, R.B. Dooley, International Materials Reviews 55 (2010).
[110] S. Naka, M. Inagaki, T. Tanaka, Jom 7 (1972) 441.
[111] Z.G. Yang, G.G. Xia, S.P. Simner, J.W. Stevenson, Journal of the Electrochemical Society 152 (2005) A1896-A1901.
[112] Y. Liu, J.W. Fergus, C. Dela Cruz, Journal of the American Ceramic Society 96 (2013) 1841-1846.

LIST OF PUBLICATIONS

L. Ge, F. S. Pettit, K. Patil, E. Sun, R.K. Singh, M.P. Brady, and P. Singh "*High temperature oxidation and chromium evaporation of an alumina forming austenitic stainless steel*" submitted to Corrosion Science

L. Ge, L. Moretti, F. S. Pettit, and P. Singh "*Corrosion of chromia and alumina forming iron alloys in molten Na-K nitrate salt*" submitted to Oxidation of Metals

L. Ge, F.S. Pettit, N. Kidner, M. Seabaugh, and P. Singh, "*Chromium evaporation from manganese cobalt oxide spinel coated & uncoated AISI 441*" Manuscript in preparation for submission to Journal of Power Source

K. Patil, **L. Ge**, F. S. Pettit, and P. Singh "*Electrochemical corrosion behavior of alumina and chromia forming austenitic stainless Steels in molten Li_2CO_3–Na_2CO_3 environment*" to be submitted

L. Ge, A. Verma, R. Goettler, D. Lovettet, R. K. Singh, and P. Singh "*Oxide scale morphology and chromium evaporation characteristics of alloys for balance of plant applications in solid oxide fuel cells*" Metrans A, 44A, (2013)

S. Bhowmick, **L. Ge**, A. Verma, P. Singh "*Assessment of chromium evaporation from chromia and alumina forming alloys*", Advances in Solid Oxide Fuel Cells VII: Ceramic Engineering and Science Proceedings, Volume 32

L. Ge, A. Czerwinski, B V Mahesh, M. K Mahapatra, P Singh, RK Singh Raman "*Degradation of High Temperature Materials in Traditional and Modern Energy Systems*", ICAER Conf. Proceedings, IITB, 2013